

MICROCOPY RESOLUTION TEST CHART  
NATIONAL BUREAU OF STANDARDS-1963-A

2

FTD-ID(RS)T-0639-85

AD-A162 993

# FOREIGN TECHNOLOGY DIVISION



ACTA AERODYNAMICA SINICA  
(SELECTED ARTICLES)

DTIC FILE COPY



**DTIC**  
**ELECTE**  
JAN 09 1986  
**S** **D**  
**E**

Approved for public release;  
distribution unlimited.



86 1 08 062

## EDITED TRANSLATION

FTD-ID(RS)T-0639-85

5 Dec 85

MICROFICHE NR: FTD-85-C-001201

ACTA AERODYNAMICA SINICA (SELECTED ARTICLES)

English pages: 178

Source: Konggi Donglixue Xuebao, Nr. 4, 1984,  
pp. 1-14; 21-33; 41-97

Country of origin: China

Translated by: SCITRAN

F33657-84-D-0165

Requester: FTD/TQTA

Approved for public release; distribution unlimited.

THIS TRANSLATION IS A RENDITION OF THE ORIGINAL FOREIGN TEXT WITHOUT ANY ANALYTICAL OR EDITORIAL COMMENT. STATEMENTS OR THEORIES ADVOCATED OR IMPLIED ARE THOSE OF THE SOURCE AND DO NOT NECESSARILY REFLECT THE POSITION OR OPINION OF THE FOREIGN TECHNOLOGY DIVISION.

PREPARED BY:

TRANSLATION DIVISION  
FOREIGN TECHNOLOGY DIVISION  
WP.AFB, OHIO.

Accession For	
NTIS NEA&I	<input checked="" type="checkbox"/>
DTIC TAB	<input type="checkbox"/>
Unannounced	<input type="checkbox"/>
Justification	
By _____	
Distribution/ _____	
Availability Codes	
Dist	Avail and/or Special
A-1	

Table of Contents

Graphics Disclaimer ..... iii

Advances in the Study of Separated Flows, by Zhuang Fenggan,  
Zhang Hanxin ..... 1

Some Problems in Discrete Vortex Numerical Modelling of  
Vortex Motion Behind A Circular Cylinder, by Ling Guocan ..... 23

Calculation of Slender Delta Wing with Leading-edge Separation  
by Quasi-Vortex-Lattice Method, by Xiung Shauwen ..... 35

Calculation of Flow Around Thick Wing with Separation Vortices;  
by Zhu Peiye ..... 47

The Split Coefficient Matrix Difference Method for Supersonic  
Three-Dimensional Flow, by Zhang Lumin, Shan Xiaonan ..... 63

Investigation on Some Characteristics of the FLIC Method and Its  
Application to Calculation of Pitot Pressure of Dusty-Gas Shock Tube Flow;  
by Du Xixin ..... 72

An Experimental Investigation of Flap Turbulent Heat Transfer and  
Pressure Characteristics In Hypersonic Flow, by Gao Ruifeng ..... 90

*Laser Doppler Anemometer*  
LDA Measurements for Leading Edge Vortex Core Velocity of a Strake-wing,  
Lu Zhiyong, Cheng Yuangzhong ..... 101

An Experimental Research of Boundary Layer Control Technique for  
Low Speed Multi-component Airfoils, by Wang Jie ..... 114

A Simpler Implicit Method to Solve N-S Equation, by Zhang Hanxin,  
Yu Zechu, Lu Linsheng ..... 124

Numerical Calculation of Separation Flow Over Severely Indented  
Blunt Body, by Gao Shuchun, Gu Gangmin ..... 132

An Implicit Technique for Calculating Separated Base Flow, by  
Dong Changquan ..... 141

Computation of Compressible Turbulent Separated Boundary Layer,  
by Liu Songling ..... 149

3771 +  
↓

An Inverse Boundary Layer Method for Separated Flow, by Qin Ning ..... 158

Wall Lift Interference Corrections in the Ground Effect Testing,  
by Li Jingbai, Qi Mengbo ..... 168

→ (translation, writing, Chinese language) \*

GRAPHICS DISCLAIMER

All figures, graphics, tables, equations, etc. merged into this translation were extracted from the best quality copy available.

## Advances in the Study of Separated Flows

/1

Zhuang Fenggan (Beijing Institute of Aerodynamics) and Zhang Hanxin (Chinese Aerodynamic Research and Development Center).

## Abstract

This paper is divided into two parts. The first part deals with the discussion of numerical simulation of separated flow in which problems requiring further investigation using the NS equation are identified. The second part involves the use of differential topology for the quantitative analysis of a flow field. Furthermore, some preliminary investigation on three-dimensional separation and vortex formation is discussed.

## I. Introduction

For a long time, people believed that flow separation should be avoided in order to obtain good aerodynamic properties. In reality, separation always occurs. For instance, separation always occurs on the lee side when an aircraft flies at a large attack angle. In addition, we also discovered that the leading edge separation vortex could improve the lift of the airfoil. Hence, the important task is to understand and control the mechanism of separation and vortex motion in order to create the condition for implementing active control. This paper will not discuss any experimental techniques. It only discusses the most important progress in digital simulation and qualitative analysis from the theoretical angle.

## II. Numerical Simulation of Separated Flow

First, we must have a mathematical model. One model is used to simulate a steady flow and the other is to simulate a real time flow. The steady and non-steady NS equation can be used as an accurate mathematical model, respectively. This also includes turbulent flow. Of course, equations can be simplified in many cases. Various turbulent flow models have to be used in calculating a turbulent flow. Different simplifications procedures may be used in different regions. In the solution finding process, iterations can be performed in order to match it between regions. This method is very often suitable for a steady flow. Even for a steady flow, iterations between regions may also be lengthy. Therefore, we employed simplified NS equation which satisfy all regions within a specific accuracy range. The current simplified NS equations include: the simplified NS equation introduced by Davis<sup>[1]</sup> based on Zheng Xiangi's viscous thin shock wave layer theory, which is accurate to the  $Re^{-1}$  order of magnitude and is called the viscous shock wave layer equation, the parabolic NS equation, i.e., the PNS equation, introduced by Lubard and Helliwell<sup>[2]</sup> by omitting all diffusion terms related to the flow direction in the steady NS equation, and a thin layer approximation equation which omits all diffusion terms in the flow direction and transverse direction. In two-dimensional cases, PNS equation is identical to the thin layer equation. In steady conditions, the viscous shock wave layer equation is parabolic in both the flow and transverse directions. However, due to the presence of a subsonic region, the equation is also

weakly elliptical. PNS equation is parabolic in the flow direction. However, it is elliptical in the transverse direction. It can be used to simulate a transverse separation problem where the flow separation region is not too large. Similarly, because of the presence of a subsonic region, the pressure gradient along the flow direction should be specially treated in performing iterations.

This paper was received on June 26, 1984

When a separation region is present, a single scan most often cannot yield accurate results. Therefore, it is necessary to perform repeated scans or overall iteration. A simplified equation is only suited for a separation region which is not very large. Normally, the complete NS equation will have to be relied on to directly deal with the problem. /2

Currently, the use of NS equation (including simplified NS equations) to simulate a viscous separated flow is in the developing stage. A great deal of work has been done on laminar and turbulent flows. Simulation is partially successful in dealing with some typical flows such as shock wave boundary layer interference, two-dimensional compression turning, flow around the airfoil and flow around a hemispherical cylinder. Especially in laminar flow conditions, the data are basically in agreement with the experimental results. In the case of turbulent flow, there is usually a larger difference because there is a lack of reliable turbulent flow models in the separation region and the neighboring regions. In addition, the Reynold's number used in

the simulation, which is to some extent related to the turbulent model, is not high enough. Therefore, current numerical simulation of NS equation cannot yet be used extensively to solve separated flow problems in engineering due to the limitation of computer and turbulent model. In spite of these limitations, numerical simulation of NS equation is very useful to the further understanding of the flow mechanism. Furthermore, it creates conditions for engineering application on the long run. In steady conditions, NS equation is hypobolically elliptical. Because of the elliptical nature, its numerical simulation is very complicated. After taking the development of new computers into consideration, we leaned toward a time correlation method, which can reflect real time simulation, to solve NS equation. In order to make practical numerical simulation feasible, we must properly solve the following problems.

1. The coordinate system and mesh chosen must have a sufficiently high resolution to describe the physical characteristics of the flow field. Currently, a body coordinate is most frequently used to turn the physical space to solve the equation into a simple regular region (such as a rectangular parallelepiped or a sphere). The boundary of the physical space is the boundary for the simple region. The early TTM method<sup>[3]</sup> using elliptical equation to solve the problem is usually considered as the most popular method. The elliptical nature ensures the smoothness of the solution. Furthermore, we can adjust the distribution of the nodal points of the mesh by

choosing an appropriate control function. The disadvantage of this method is that it takes more computer time and memory space. A simpler approach is to use a mesh formation method for algebraic equations<sup>[4]</sup>. A typical algebraic method is to introduce several layers of control surfaces between the inner and outer boundary based on the characteristics of the physical problem so that the boundary corresponds to plane in the simple region. Then, the corresponding relation of internal nodal points is found by intrapolation of algebraic expressions. As for recent advances, in addition to using various methods to generate meshes, the study of optimization of meshes and self-adapting meshes is more important which allows the automatic capture of shock wave and vortex surface. It can accurately reflect the spatial flow in the large gradient region. The key is to correctly present a guideline for optimization and self-adaption. This is a problem worth further investigation.

2. The selection of a difference scheme can directly affect the stability and rate of convergence of the solution. Explicit time dependent methods were used in earlier simulation. However, due to limitation of stability conditions, the allowed time step in the calculation is too small. Therefore, many implicit methods have been developed. Here, only implicit difference schemes are analyzed.

First, the center of our discussion is implicit difference methods, which include the non-iterative implicit factorization method<sup>[6][7]</sup>, ADI method and time sharing implicit center difference method<sup>[8]</sup>. It was proven that these three methods are

interchangeable within the range of second order precision. Moreover, all three use center difference. These are feasible methods. The Courant number, which is related to the time step length, can reach an order of magnitude of several hundreds or thousands. However, in the calculation, especially in dealing with problems with hidden shock wave, it is necessary to add an artificial dissipation term. This is a key technical measure to control oscillation and it is highly empirical. In addition, it is necessary to form viscous and inviscous Jacobian matrices and to solve three diagonal matrices by chasing in the calculation. Hence, the computation and programming workload is large.

Another important implicit scheme was introduced by MacCormack in 1981<sup>[9]</sup>. As compared to the method described above, it has the following advantages. First, the difference /3 scheme employed is a two-point single side difference. Therefore, it is only necessary to chase two diagonal matrices. Second, it is only necessary to calculate the inviscous Jacobian matrix in the computation. However, the effect of viscosity is taken into account in the stability condition when we calculate the absolute matrix. Third, when the time step satisfies the explicit expression stability condition, it is able to automatically change into the early stage MacCormack explicit scheme. These special features reduce the workload. However, we must still calculate the characteristic value of the Jacobian matrix. Moreover, it is necessary to create an absolute matrix. This cancels some of the advantages. Unfortunately, an empirical artificial dissipation term must still be added to eliminate

oscillation in the calculation of a separated flow field with shock waves.

In order to solve this problem, Coakley<sup>[10]</sup> introduced an implicit windward difference method. As a matter of fact this method originates from the separation coefficient matrix method used to solve hypobolic equations. The basic idea is to use the characteristic value of the inviscous portion of the Jacobian matrix in the NS equation to control the spatial derivative of the inviscous part. When the characteristic value is greater than zero, a second order difference directed toward the rear is used. When the characteristic value is less than zero, a second order difference directed forward is used. The spatial derivative of the viscous portion employs center difference. This scheme, in theory, is dissipating. There is no need to add another dissipation term. Examples of shock wave and boundary layer interference calculation show that this method is highly accurate and stable. The time step for calculation is large. The convergence rate is fast. Furthermore, it does not need an added artificial dissipation term. A detailed analysis indicates that the region where the characteristic value changes sign indicates that the region where the characteristic value changes sign may require special treatment. Coakley was inspired by Harten's work<sup>[11]</sup> to create dissipation functions. These are problems to be studied further. Other difference schemes are not discussed individually.

3. In implicit calculation, it is very important to provide the computation condition on the boundary. If it is not properly

given, the computation is not going to be stable. Or, this difference equation set and boundary condition make the problem unsuited to define. As an example, we are quoting the paper by Abarbanel and Murman<sup>[12]</sup>. They gave some inspiring conclusions. In the following equation

$$\frac{\partial U}{\partial t} = \frac{\partial F(U)}{\partial x} - \frac{\partial G(U)}{\partial y}$$

if the region for calculation is  $0 \leq x \leq \infty, -\infty < y < \infty, t > 0$ , they proved that if the backward Euler implicit scheme or Crank-Nicolson implicit scheme is used to solve the above equation, then

(1) the computation is stable if the boundary condition is

$$U_{i;0} = 2U_{i;1} - U_{i;2}$$

(2) the computation is stable if the boundary condition is

$$U_{i;0} = 2U_{i;1} - U_{i;2}$$

Here, the first subscript represents the nodal point in the x-direction where "0" represents  $x = 0$ . The second subscript is the nodal point number in the y direction. It is easy to see that the first boundary condition is implicit and the second boundary condition is triply explicit.

4. Accelerated convergence in the computation is also an important problem. There are many measures introduced in the literature. We believe that we should pay more attention to multi-mesh and the self-adapting mesh technique mentioned above.

The multi-mesh technique was first introduced by in 1962<sup>[13]</sup>. Later, Brandt<sup>[14]</sup> made further advances. Its basic

advantage is that the coarse mesh can eliminate errors caused by low wave number and the fine mesh can eliminate errors caused by high wave number. This technique has already successfully been used in the calculation of the transonic small perturbation equation, complete velocity potential equation and Euler equation. In addition it is beginning to be applied to the computation of NS equation. Stubbs<sup>[15]</sup> combined this technique with MacCormack's /4 implicit scheme and obtained very good results. In the following, we will use a one-dimensional problem as an example to split the NS equation into inviscous and viscous portions and to employ the method suggested by Stubbs to explain the procedure of multi-mesh calculation for the inviscous portion. Let us assume that the inviscous part of the equation is

$$\frac{\partial U}{\partial t} + \frac{\partial F}{\partial x} = G$$

The procedure is:

(1) to use MacCormack's implicit method to calculate  $\delta U_j^h = (U_j^{n+1} - U_j^n)^h$  on the fine mesh nodal points (assuming the mesh spacing is h).

(2) to use the Ni scheme to calculate  $\delta U_j^{2h}$  on the nodal points of the coarse mesh (assuming the mesh spacing is 2h and nodal points are j, j+2, j+4, ...)

$$\delta U_j^{2h} = \frac{1}{2} \left[ \delta U_{j-1}^h + \delta U_{j+1}^h + \frac{\Delta t}{\Delta x} (A_{j-1} \delta U_{j-1}^h - A_{j+1} \delta U_{j+1}^h) + \frac{1}{2} \Delta t (B_{j-1} \delta U_{j-1}^h + B_{j+1} \delta U_{j+1}^h) \right]$$

where  $A = \partial F / \partial U$ ,  $B = \partial G / \partial U$ . According to this result, the values on other nodal points of the original fine mesh may be obtained by linear intrapolation.

(3) If the mesh is still not coarse enough, we can use the Ni scheme to calculate the values on nodal points of a coarser

mesh (j, j±4, j±8, ...):

$$\delta U_j^k = \frac{1}{2} \left[ \delta U_{j-2}^k + \delta U_{j+2}^k + \frac{\Delta t}{\Delta x} (A_{j-2} \delta U_{j-2}^k - A_{j+2} \delta U_{j+2}^k) + \frac{1}{2} \Delta t (B_{j-2} \delta U_{j-2}^k + B_{j+2} \delta U_{j+2}^k) \right]$$

Values on nodal points of the fine mesh can be obtained by linear intrapolation.

(4) to use MacCormack's method to perform implicit fine mesh calculation based on the values obtained with the coarse mesh nodal points. Then, steps (2) and (3) are repeated until a stable solution is obtained.

Of course, the problems discussed above are the major ones to be seriously studied if numerical simulation NS equation of separated flow is going to become practical. To some extent, these are fundamental problems. On one hand, we need theoretical studies. On the other hand, we must rely on a great deal of numerical experiments to solve these problems. As a part of the theoretical work, differential topology will be applied to the qualitative analysis of the flow field.

### III. Qualitative Analysis of the Flow Field

Separation starts from the surface of an object. Then, the vortex penetrates deep into the flow region. The study of separation can begin with the study of the flow pattern on the surface of the object. Lighthill<sup>[16]</sup> is the pioneer in this field. He introduced the friction line concept and assumed that friction is a continuous two-dimensional vector field. We usually believe that surface friction line is the limiting stream line. If an x,y coordinate is introduced to the surface and

$\tau$  and  $\sigma$  are the friction components in x and y direction, respectively, then the differential equations defining the friction line are:

/5

$$\frac{dx}{d\lambda} = \tau(x, y, Re, M, \alpha, \dots)$$

$$\frac{dy}{d\lambda} = \sigma(x, y, Re, M, \alpha, \dots)$$

where  $Re$ ,  $M$ ,  $\alpha \dots$  are parameters such as Reynolds number, Mach number and attack angle, and  $\lambda$  is a chosen variable. Relative to different parameters, the distribution of the surface friction line is different, i.e., with various types of topologic structures. From the qualitative theory of differential equation we know that the topological structure is determined by the number of singular points (points where  $\tau=\sigma=0$ ), the property of each singular point and the connection of mutual friction lines between singular points. Furthermore, according to qualitative theory, a structurally stable singular point can only be a first order singular point. One type is the settle point whose Poincare index is -1. The other type includes focal point, nodal point and center point, and the corresponding Poincare index is +1. For an enclosed curve surface, the total singular point index  $S$  is

$$S = 2-2g$$

where  $g$  is the topological seed value of the curve surface. For a curve surface topologically equivalent to a spherical surface,  $g=0$ ,  $g=1$  if it is equivalent to an annular curve surface. Therefore, there are 2 more nodal points (including focal points and centers) than settle points on a spherical surface. Hence,

their topological structure can only be  $N_2, N_3, S_1, N_4, S_2, N_5, S_3$  .....  $N_n S_{n-2}$ , where N represents a nodal point and S represents a settle point. The subscript represents the number of that particular point. Bippes<sup>[17]</sup> obtained a dozen or so different flow patterns up to  $N_5 S_3$  in the hemispherical cylinder oil flow experiment. We are not going to investigate very complicated flows here. Instead, we will use the flow around an ellipsoid with an attack angle studied by Wang Guozhang as a typical example for analysis. In addition, we hope to clarify some controversies. Based on experimental results and theoretical analysis, Wang divided the basic flow into the following three regions:

(1)  $0 < \alpha < \alpha_{sv}$ , closed separation emerges at the tail as shown in Figure (1a);

(2)  $\alpha_{sv} < \alpha < \alpha_{av}$ , open separation begins on the leeward side, together with the formation of a small second order closed separation region in the rear, as shown in Figure (1b);

(3)  $\alpha > \alpha_{av}$ , another closed separation appears on the leeward side as shown in Figure (1c).

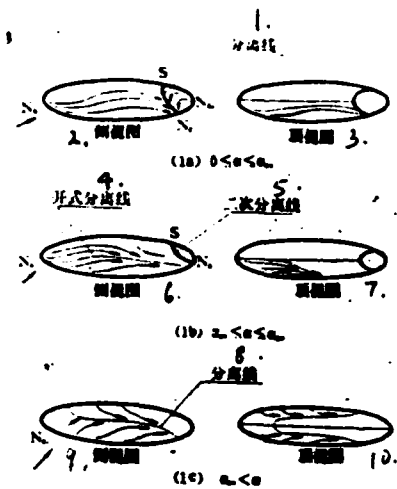


Figure 1. Basic Patterns of Flow Around an Ellipsoid with an Attack Angle

1. separation line
2. side view
3. top view
4. open separation line
5. second order separation line
6. side view
7. top view
8. separation line
9. side view
10. top view

The boundary of each region shown in the figure is related to the aspect ratio of the ellipse when the incoming flow is identical. This flow pattern is quite different from the flow around a slender body at a large attack angle. Here, the shape of the head and the tail, especially the head, has an important effect. Before analyzing these patterns, several points are obvious from the topological viewpoint. The separation line and re-adhesion line must be the limiting stream lines. The limiting stream lines on both sides of the separation line will be drawn closer to the separation line. The limiting stream lines on both

sides of the re-adhesion line, however, are moved away from it. The separation line may be a part of the limiting stream line or may be the entire limiting stream line. A limiting stream line must be from a singular point to a singular point. Or, it must be an enclosed curve. It cannot terminate at a regular point.

With regard to closed separation, there is no controversy. Figure (1a) shows that the separation line is the line of friction from  $S$  to  $N_s$ , which agrees with the  $N_3S_1$  topological structure model. The open separation Wang introduced to Figure (1b) was in fact first observed experimentally by Maskell. Wang pointed out that this open separation is a separation without any singular point. It is not related to Lighthill's singular point separation at all. In addition, Wang also made a transition from closed separation to open separation and attributed it as the so-called tongue splitting<sup>[19]</sup>. These conclusions warrant further investigation because tongue splitting does not agree with laws of topology. In addition, as shown in Figure (1b), the open separation line must be located on the line of friction connecting  $N_{a1}$  to  $N_s$ . If the line terminates at a new  $N_s$ , then it obviously does not satisfy Poincare's law of topology. Open separation is an important three-dimensional separation mode from the formation of vortex. There is practical significance to study it further. We noticed that Tai<sup>[20]</sup> pointed out that drawing limiting stream lines together alone is not enough to create vortex separation. It also requires "collision" with the inviscous stream line on the outer fringe of the boundary, just as the pattern shown by

Maskell earlier. Thus, we analyze that separation and vortex formation must be studied as a whole. Dallmann<sup>[21]</sup> first pointed out that the spatial topological structure corresponding to an identical surface flow pattern is not unique. We still do not have a complete topological theory in a three-dimensional space. However, if we consider any surface in the space and the continuous velocity field on the surface, this surface can intersect with the surface of the object. By defining the singular point on the body surface is a semi-nodal point  $N'$  or semi-settle point  $S'$ , then Hunt<sup>[22]</sup> proved that

$$G = \left( \Sigma_N + \frac{1}{2} \Sigma_{N'} \right) - \left( \Sigma_S + \frac{1}{2} \Sigma_{S'} \right) = 1 - n$$

where  $\Sigma_N$  is the total nodal point number,  $\Sigma_S$  is the total settle point number,  $\Sigma_{N'}$  is the total semi-nodal point number,  $\Sigma_{S'}$  is the total semi-settle point number and  $n$  is the chosen degree of surface connection. For a single connected region  $n=1$ . For a double connected region,  $n=2$ .

This law can be used to preliminarily analyze the basic flow pattern around a slender body at a large attack angle. Nielsen<sup>[23]</sup> and Ericsson<sup>[24]</sup> summarized the experimental results from low velocity to a transonic flow with a transverse Mach number  $M_c$  of less than 0.5. According to the size of the attack angle  $\alpha$ , the state of flow can be divided into five regions:

(1)  $0 < \alpha < \alpha_{sv}$ , the flow is adhered to the body as shown in Figure (2a);

(2)  $\alpha_{sv} < \alpha < \alpha_{av}$ , symmetric stationary vortices appear in the leeward area as shown in Figure (2b);

(3)  $a_{av} < a < a_{bv}$ , asymmetric stationary vortices appear in the leeward area as shown in Figure (2b);

(4)  $a_{bv} < a < a_{av}$ , alternating non-stationary vortices appear in the leeward area as shown in Figure (2d); and

(5)  $a > a_{uv}$ , the leeward area becomes non-stationary vortices and tailing of random vortex motion.

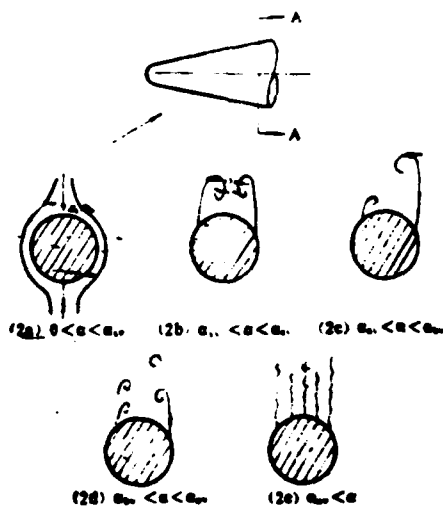


Figure 2. Basic States of Flow Around a Slender Body at Large Attack Angle (in A-A cross-section)

The flow at  $M_c \leq 0.5$  is often called a subcritical flow. Conclusive opinions on supercritical flow at  $M_c \geq 0.5$  are still to be further studied. The classification into five regions is also a rough one. The actual flow is far more complex than those drawn here. A topological structure analysis of the flow pattern shows that the transition from one region to another is an important subject. First, let us look at Figure (2a). There are only two semi-stagnation points on the plane,  $G=-1$ , which agrees with the topological law. Figure (2b) only shows 4 semi-stagnation points and 2 nodal points. Obviously, there is another stagnation point in

the upper flow field. The topological format is  $N_2S_1S_4'$ . Figure (2c) shows the generation of an asymmetric lateral force on the slender body in region (3). Before it is developed into an asymmetric vortex, a second order separation and interaction between the primary separation vortex and the secondary vortex exist on the body surface. In the early stage, some people /7 believed that asymmetric vortices are created by asymmetric separation on the leeward side. However, G. Chapman et al found experimentally in 1975 that asymmetric vortices are not primarily created by asymmetric separation. Instead, they are due to fluid dynamic instability. Peake and Tabak<sup>[25]</sup> believed that the asymmetry of a fluid is related to the instability of the velocity cross-section at the upper settle point on the cross-section of the object. Furthermore, this mechanism was qualitatively interpreted based on its topological structure. The study on the control and breakup of asymmetric vortex is still in its infancy.

Now let us give a preliminary qualitative analysis on the spatial flow field. The Cartesian coordinate  $x_j$ ,  $j = 1, 2, 3$  is used.  $u_j$  is the velocity component in the  $x_j$  direction. Let a singular point be the origin. Its neighborhood is

$$u_j = a_{j,i} x_i, \quad a_{j,i} = \left( \frac{\partial u_j}{\partial x_i} \right)$$

The stream line equation can be written as

$$\frac{dX}{dt} = AX$$

where

$$A = a_{j,i}, \quad X = (x_1, x_2, x_3)^T.$$

Let us assume the eigen value of A is  $\lambda_j$ ,  $j = 1, 2, 3$  and the eigen vector corresponding to  $\lambda_j$  is  $C_{ij}$ . In this case, the eigen value of  $A^T$  is also  $\lambda_j$ . The corresponding eigen vector is  $B_{ij}$ . Furthermore,

$$B_{ij} C_{kj} = \delta_{ik}$$

The solution of the differential equation is

$$x_i = \sum_{j=1}^3 \varphi_j C_{ij} e^{\lambda_j t}$$

$\varphi_j$ ,  $j = 1, 2, 3$  are integration constants.  $\lambda$  satisfies the following third order equation

$$\Delta - \left[ \frac{\partial(u_1, u_2)}{\partial(x_1, x_2)} + \frac{\partial(u_2, u_3)}{\partial(x_2, x_3)} + \frac{\partial(u_3, u_1)}{\partial(x_3, x_1)} \right] \lambda + \frac{\partial u_i}{\partial x_i} \lambda^2 - \lambda^3 = 0$$

where  $\Delta$  is the value of the determinant corresponding to A. For steady flow and incompressible flow, because of the continuity equation.

$$\sum_{j=1}^3 \lambda_j = 0$$

When the three roots are all real, they cannot simultaneously be positive or negative. This means that singular points cannot all be nodal points or settle on three mutually perpendicular planes. Furthermore, we can define three plane

$$B_{ij} x_j = 0$$

These three planes are tangent to regular flow surfaces. Where one root is real and the remaining two are complex conjugate roots, it is only possible to define one plane tangent to the regular flow surface. In this case, there is a singular stream line. Other stream lines are cylindrical spirals around this

singular stream line. Using the Candan equation and assuming

$$J_1 = \frac{\partial(u_1, u_2)}{\partial(x_1, x_2)} + \frac{\partial(u_2, u_1)}{\partial(x_1, x_2)} + \frac{\partial(u_1, u_1)}{\partial(x_1, x_1)}$$

then the necessary and sufficient condition for a pair of conjugate solutions is

$$\frac{\Delta^2}{4} + \frac{J_1^2}{27} > 0$$

The ordinary vortex we are referring to (including the vortex /8  
created by an open separation) is this type of spiral flow. If  
our only objective is to determine whether there is a vortex  
structure around a specific point, we may choose a coordinate  
system which is moving with the velocity of that point and the  
above analysis is still valid. By using the results discussed  
above, it is very easy to prove that the condition to have a  
vortex leaving a symmetric flow plane is that the initial  
singular point should be a focal point and the core stream line  
of the vortex (singular stream line) is perpendicular to the  
symmetry plane. A similar method can be used to study the  
spatial flow near the surface which demonstrates that the  
formation of a horn vortex originates from a focal point singular  
point on the surface. Incidentally, we noticed that the A matrix  
is a real symmetric matrix for an imitational motion. All its  
eigen values are real. There is, of course, no such vortex  
structure.

#### IV. Conclusions

This paper does not involve any practical engineering problems with complicated separation and vortex motion. The difficulties in theoretical calculation are apparent. To date, Graham and Hankey's<sup>[26]</sup> calculation of asymmetric vortex is most successful. However, from Lamont's experiment<sup>[27]</sup>, the magnitude of the lateral force is also related to the tumbling angle and Reynolds number. Moreover, in turning point situation, the lateral force is almost decreased to zero. The contribution of laminar flow separation to the magnitude of lateral force is comparable to that of turbulent flow separation. However, the distribution is not consistent. In addition to carrying out detailed experimental studies on the rolling of spatial vortex, the mutual interaction among vortices from one topological structure to another, and the appearance of a random tail flow, theoretical qualitative analysis will provide us with great assistance. This discussion covered in this paper only classifies the status and basis for further studies.

In the preparation of this paper, Comrade Li Suxun was also very helpful. The authors wish to express their gratitude.

#### References

- [1] David, R.T., AIAA J. Vol. 8, 843-851, 1970.
- [2] Lubard, S.C. and Helliwell, W.S., AIAA J. Vol. 12, 965-974, 1974.
- [3] Thompson, J. F et al, J. of Comp Physics Vol. 15, No. 3, 1974.

- [4] Eriksson, L.E., AIAA J. Vol. 20, 10, 1982.
- [5] Smith, R.E., AIAA Paper 83-1904.
- [6] Beam, R. and Warming, R.F., AIAA J. Vol. 16, 393-401, 1978.
- [7] Tannehill, J.C. et al. AIAA Paper 81-0049.
- [8] Zhang Hanxin et al, Applied Mathematics and Mechanics, Vol. 4, No. 1, 1983.
- [9] MacCormack, R.W., AIAA Paper 81-0110.
- [10] Coakley, T.J., AIAA Paper 83-1958.
- [11] Harten, A, NYU Report, New York Univ, New York, N.Y., Mar. 1982.
- [12] Abarbanel, S.L. and Murman, E.M., J. Comp Phys, Vol. 48, 2, 1982.
- [13] Федоренко Р. П., ЖВММФ 1, 1092-1096, 1982.
- [14] Brandt, A., Lecture Notes in Physics 18. pp 82-89 Springer-Verlag, 1973.
- [15] Stubbs, R.M., AIAA Paper 83-1945.
- [16] Lighthill, M.J., in Laminar Boundary Layers pp 48-88, Oxford Univ. Press, 1983.
- [17] Bippes, H and Turk, M., DFVLR IB 222-83 A 07.
- [18] Wang, K.C., AIAA J. Vol, 10, pp 1044-1050, Aug. 1972.
- [19] Wang, K.C., AIAA Paper 83-0296.
- [20] Tai, T.C., AIAA Paper 83-0297.
- [21] Dallman, U., AIAA Paper 83-1735.
- [22] Hunt, J.C.R., et al, JFM Vol. 86, part 1 pp 179-200. 1978.
- [23] Nielsen, J.N., AIAA Paper 78-20.

/9

- [24] Ericsson, L.E., ZFW, No. 3-5, 1981.
- [25] Tobak, M. and Peake, D.J., AIAA Paper 79-1480.
- [26] Gnahan, J.E., and Hankey, W.L., AIAA J. Vol. 21, 11, 1983.
- [27] Lamont, P.J., AIAA Paper 80-1556.

## ADVANCES IN THE STUDY OF SEPARATED FLOWS

Zhuang Fenggan  
(BIA)

Zhang Hanzin  
(CARDIC)

### Abstract

This paper consists of two parts. The first deals with the numerical simulation of separated flows and problems need further study are indicated with NS equations model. The second involves an application of differential topology to qualitative analysis of flow fields and the connection between 3D-separation and vortex production is discussed.

Some Problems in Discrete Vortex Numerical Modelling of  
Vortex Motion Behind a Circular Cylinder

/10

Ling Guocan (Institute of Mechanics, Academia Sinica)

Abstract

This is a brief review of the four problems encountered in the discrete numerical modelling of unsteady flow and vortex motion behind a circular cylinder, i.e., the discrete method and the stability of the vortex sheet, boundary layer separation and the positions of nascent vortices, the secondary vortex problem and the reduction of circulation of vortices in the wake. The paper also presents some topics which require further study.

Introduction

For an abruptly started unsteady constant velocity cylindrical motion (corresponding to an unsteady uniform flow around a cylinder), the numerical modelling under subcritical conditions at high Reynolds numbers needs another theoretical approximation model because the results of the numerical solution of the existing N-S equation are not dependable. The important characteristics of the viscous separation flow of a non-stream line convex object are the formation, concentration, offset, and consumption of a vortex. In a two-dimensional incompressible N-S equation (expressed by  $\xi$  and  $\phi$ ), the distribution of the vortex function  $\xi$  with time and space will determine the entire flow ( $\phi$ ). A simplified theoretical model is based on how to relatively accurately reflect the distribution of  $\xi$ . For a high Reynolds

number flow with a valid boundary layer, this type of small viscosity fluid flow can be expressed by using the inviscous flow theory together with the assistance of boundary layer flow, circulation and concentrated vortex. In the flow field, continuously or concentrated vortices are expressed, in approximation, by many discrete small vortices of some strength. This is the discrete vortex method. In recent years, there are significant advances in the discrete vortex method in conjunction with the boundary layer theory. Some numerical experiments on the circular cylinder flow were successful in calculating the disengagement frequency. This method is also very simple. The dimensionless time in the computation may be as long as over 200, which is equivalent to travelling a distance more than 200 times the radius of the circular cylinder after the motion begins. However, because this flow is relatively complex, the changes of flow with time include unsteady separation of the boundary layer, formation and variation of the shear sheet, creation and development of vortices, alternating disengagement of vortices and the variation of vortices. To date, the understanding of the mechanisms and patterns of some problems such as the characteristics of the rear shear sheet layer, the disengagement process of vortices and the dissipation of vortices in the wake is still inadequate. There are also some problems in the numerical modelling using the discrete vortex method, which require further discussion and resolution. The following is a brief review of these four problems.

## I. Discrete Method and Stability of Vortex Sheet Motion

The motion of the vortex sheet is mathematically an initial value problem. However, the question of the existence of the solution and its uniqueness remains unproven.

This paper was received on June 14, 1984.  
This paper was a part of the National Separation Vortex Flow Academic Report held on April 10-20, 1984.

In the actual computation of the discrete vortex method, the point vortex group tends to move randomly when the computation gets too long. In Reference [1], the cause of this random motion was analyzed in the domain of inviscous flow theory. The induced conjugate complex velocity  $\bar{q}(z_i)$  at any point  $z_i$  in space by a continuous vortex sheet with an intensity  $\gamma(S)$  should be /11

$$\bar{q}(z_i) = \frac{1}{2\pi i} \rho \int \frac{\gamma(S_1) dS_1}{z_i - z_1}$$

When  $z_i$  is located on the vortex sheet, singularity is shown in the integration. The principal Cauchy value should be used. If the vortex sheet is divided into many small segments and the nodal point in each segment is expressed by  $k_{\pm}(1/2)$ , then the complex velocity can be approximately written as

$$\bar{q}(z_i) = \frac{1}{2\pi i} \sum_{i=1}^N \frac{\Gamma_i}{z_i - z_i} - \frac{1}{2\pi i} \frac{\Gamma_i e^{-i\theta_i}}{|S_{i+\frac{1}{2}} - S_{i-\frac{1}{2}}|} \ln |(z_i - z_{i+\frac{1}{2}})(z_i - z_{i-\frac{1}{2}})|^{-1}$$

The induced velocity by N discrete point vortices at point  $z_j$  is

$$\bar{q}(z_j) = \frac{1}{2\pi i} \sum_{i=1}^N \frac{\Gamma_i}{z_i - z_j}$$

By comparing the above we know that the velocity of a point vortex calculated by the discrete vortex method is different from

the velocity induced by the actual continuous vortex sheet. The difference is a logarithmic term. Both are in agreement when point  $z_j$  is located at the center of the vortex segment. The logarithmic term gets larger when the distances between  $z_j$  and the two ends are unequal. The discrete method was used in references [1] and [2] to rearrange the positions of discrete conservation principle to make the new position of each vortex to be at the center of the vortex segment. Then, the motion of these vortices was calculated. Thus, the randomness of the motion of vortices over a long period of time is significantly decreased. The above discussion is based on the inviscous flow theory. On the other hand, when two vortices are approaching each other and the spacing is  $\delta \ll 1$ , the order of magnitude of the induced velocity given by the inviscous flow theory is  $(1/\delta) \rightarrow \infty$ . In order to eliminate the possibility of introducing a vortex nucleus to the singularity, the induced velocity in the vortex nucleus range can be calculated based on the viscous flow theory<sup>[3]</sup>. In order to facilitate engineering calculations, induced velocity in the vortex nucleus can be calculated based on the Rankine vortex model. The velocity can even be made to be zero<sup>[5]</sup>. The use of all above methods can reduce the random motion of point vortices.

Stability analysis of the motion of a non-homogeneous vortex sheet in contact with the boundary layer is more complex. As a vortex spiral develops towards downstream, the intensity decreases with the expansion of the vortex sheet. Therefore, it is somewhat stable with respect to Helmholtz stability. With

respect to the Tollmien-Schlichting instability of the portion of the shear sheet where the vortex is in contact with the boundary layer, the analysis is still inadequate. This type of instability must be predicted in the vortex developing process<sup>[2]</sup>.

## II. Boundary Layer Separation and Position of Nascent Discrete Vortices

The flow around a circular cylinder has a very short initial unsteady period. Because there are two different separation guidelines, i.e., Prandtl and M.R.S. guidelines, the position of the boundary layer is different. The initial circumferential separation differs by  $40^\circ$  and the initial dimensionless separation time ( $\bar{t} = Vt/R$ ) differs by 0.3. Correspondingly, the position and time of the initial separation vortex are different. Reference [4] pointed out that it is a reasonable consideration to place the position of a newly created vortex at the location where the boundary layer begins to thicken significantly and separation bubble begins to emerge based on the M.R.S. guideline. This paper also compared the effect of both situations on the initial wake. After a very short period of time, when  $\bar{t} \rightarrow 1$ , the variation of the cylindrical boundary layer tends to vary in a quasi-steady state. Afterwards, there is no obvious difference between the boundary layer separation positions predicted by /12 these two guidelines. Thus, the early stage of variation at  $\bar{t} < 1$  can often be omitted for the characteristics of a motion

over a relatively long period of time. The computation can begin with the boundary layer varying in a quasi-state.

When a discrete vortex is newly created, because the vortex and its image vortex "distort" the local flow field, the boundary layer will be separated prematurely. The calculated long term mean separation angle is only  $\pm 67^\circ$ <sup>[5]</sup> or  $\pm 77^\circ$ <sup>[2]</sup>, which is smaller than the widely believed  $\pm 82^\circ$ . One consideration to minimize this effect is to begin counting the induction effect of a recent vortex after one or a half step in time<sup>[3],[6]</sup>. This is equivalent to placing the initial position of the recent vortex at a distance of  $\bar{v}_j \Delta \bar{t}$  or  $(1/2)\bar{v}_c \Delta \bar{t}$  away from the separation point.  $\bar{v}_j$  and  $(1/2)\bar{v}_c$  are the background flow field velocity or the transfer velocity of the vortex point. In conjunction with viscous vortex nucleus correction, this method can improve the calculated results of the separation point. In some engineering problems focusing on long term flow characteristics, in order to avoid the above difficulty in calculating the separation point, it is assumed that separation occurs at the place where the maximum surface velocity chopped by 5%<sup>[6]</sup>. This assumption is very close to actual result. There are different methods to determine the initial radial position of a recently created vortex by satisfying the no-slip condition at the vortex at the instance when a point vortex is disengaged<sup>[5],[2]</sup>, by choosing an appropriate initial value from numerical experiments based on the stability of the vortex motion, and by using the initial radius as a half of the thickness of the boundary layer to determine the

initial radial position of the vortex when the viscous vortex nucleus is corrected<sup>[3]</sup>. In general, in flow problems involving the time-dependent separation points, the initial position of a discrete vortex does not necessarily have to be determined by the no-step condition.

### III. Secondary Vortex, Effect of Secondary Vortex and Mechanism of Vortex Detachment

The numerical modelling of the discrete vortex method under the assumption of high Reynolds number subcritical conditions shows<sup>[4-6]</sup> that the maximum return surface flow in the return flow region can reach the order of magnitude of the incoming flow in the initial unsteady stage of the flow around the cylinder. A part of the rear shear layer is continuously under the effect of a reverse pressure gradient after a specific instance. Theoretical computations<sup>[4-6]</sup> assumed that this rear shear layer would separate and create a secondary vortex in opposite direction to the primary vortex. The secondary vortex has an important effect on the motion and evolution of the primary vortex, the cancellation of vortex in the wake, the distribution of pressure on the surface of the object, and the drag and transverse force executed on the cylinder<sup>[3],[6],[7]</sup>. Figures 1 and 2 show some examples of the effect of the secondary vortex.

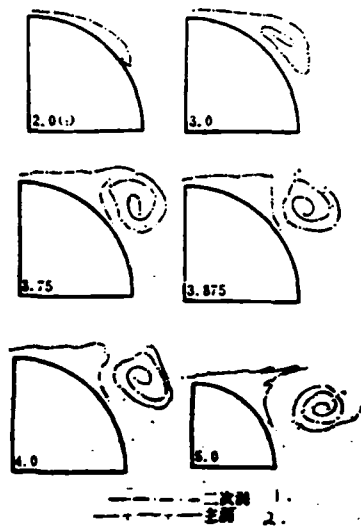


Figure 1. Effect of Secondary Vortex on the Evolution of the Primary Vortex

1. secondary vortex
2. primary vortex

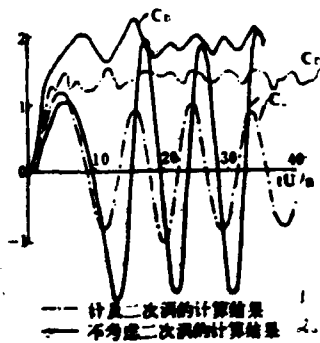


Figure 2. Effect of Secondary Vortex on Drag Coefficient  $C_D$  and Transverse Force Coefficient  $C_L$ .

1. results of computation after taking secondary vortex into account
2. results of computation by not considering secondary vortex

The vortex motion described by theoretical calculation<sup>[3,7]</sup> agrees with many experimental observations at high Reynolds numbers<sup>[8]</sup>. Therefore, the effect of rear shear layer separation and secondary vortex cannot be neglected. On the other hand, in one experiment conducted at Reynolds number 9500 it was observed /13 that there was a pre-wake formation and evolution process (including the appearance and disappearance of a pair of secondary vortices) prior to the formation of the primary wake. Afterwards, due to the instability of the flow, return flow separation, such as the one considered in the theoretical calculation, did not take place. As the calculation of the rear shear layer separation point, the time-dependent variation of the separation point was obtained by using the boundary layer approximation method (Stratford method) under the assumption of laminar flow separation in the early stage of the flow in reference [7]. In long term flow situations, there are only approximation methods<sup>[5][6]</sup>. Therefore, there is a need to conduct detailed non-contact experiments on the rear shear layer in order to understand its special characters so that we can perform a more delicate theoretical analysis.

There are different theories explaining the mechanism vortex detachment from the cylinder. There are two different viewpoints on the breakdown of the primary vortex sheet in its developing process due to the factor whether the effect of secondary vortices should be considered<sup>[7],[2],[5]</sup>. Correspondingly, different methods were used to introduce an asymmetric

perturbation to the numeric calculation in order to realize primary vortex detachment. However, the presence and development of secondary vortices to fracture the symmetric vortex sheet may be one of the conditions leading the vortex to begin an asymmetric motion.

#### IV. Reduction of Circulation of Vortices in the Wake

With regard to the cancellation and viscous dissipation of vortices in the wake, the total circulation in the concentrated wake vortex should be much less than the sum of the vortices detached from the boundary layer. Experimentally, it is only approximately 60% of the original value. However, the calculated result based on the discrete vortex mode 1 is around 80% of the original value. This problem has not been resolved in the theoretical model. It will have an effect, to various extents, on the separation point, transverse force, wake length,  $St$  number, size of the vortex and stability region of vortices. Cancellation of vortices is caused by approaching vortices in opposite directions and by point vortices less than a specific distance from the surface of the object. There are three possible reasons for opposite direction vortices to approach one another in the flow behind a cylinder: 1) point vortices generated by secondary vortices and boundary layer separation approach one another behind the cylinder; 2) distorted or cutoff primary vortex layer is carried into the wake by the inviscous flow; and 3) the vortices are swept apart downstream and thus distributed in the entire wake. Several numerical experiments

were conducted to study the extent of vortex reduction by different mechanisms<sup>[2],[5],[6]</sup>. In some work, a correction factor, less than 1, was multiplied to the intensity of recently created or secondary vortices in order to match the calculated drag (or other parameter) with the experimental results<sup>[3]</sup>. The distribution of vortex was studied from various angles. In reference [2], the assumption of point vortex conservation was abandoned. It was assumed that the loss of each point vortex in the wake is proportional to its intensity and its location in the recently separated vortex sheet. Certain principles for turbulent flow loss were obtained through numerical experiments. The total circulation was decreased by approximately 20% in the calculated result. However, it is necessary to further determine major causes of vortex reduction in real flows and the patterns of variation.

#### References

- [1] Fink, P.T. & Soh, W.K., Tenth Symposium of Naval Hydrodynamics.
- [2] Sarpkaya, T. & Issacson, M., Mechanics of Wave Force on Offshore Structure, Van Nostrand Reinhold Company, 1981.
- [3] Ling Guocan, Journal of Mechanics, 3 (1983).
- [4] Ling Guocan and Yi Xieyuan, Journal of Mechanics, 2 (1981).
- [5] Deffenbaugh, F.D. & Marshall, F.J., AIAA J. Vol. 14, No. 7.
- [6] Stansby, P.K. & Dixon, A.G., The Aeronautical Quarterly, 9 (1981).

- [7] Ling Guocan and Yi Xieyuan, *Journal of Mechanics*, 1 (1982).  
[8] Coutancean, M. & Bouard, R., *JFM*, 101 (1980), 3.

**SOME PROBLEMS IN DISCRETE VORTEX NUMERICAL  
MODELLING ON VORTEX MOTION BEHIND A  
CIRCULAR CYLINDER**

Ling Guocan

*(Institute of Mechanics, Academia Sinica, Beijing)*

**Abstract**

This is a shortened review which is concentrated on four aspects in discrete vortex numerical modelling on unsteady flow and vortex motion behind a circular cylinder, i. e. (1) the discrete method and the stability of the motion of vortex sheet (2) boundary layer separation and the nascent discrete vortices' positions (3) the secondary vortices problem and (4) the reduction of circulation of vortices in the wake. Some further works are also suggested in this note.

Calculation of Slender Delta Wing with Leading-edge Separation /21  
by Quasi-Vortex-Lattice Method

Xiung Shauwen (Beijing Institute of Aeronautics and Astronautics)

I. Introduction

The leading-edge separation vortex produced by a slender wing with a large backward sweep at a large attach angle has an important effect on its aerodynamic characteristics. There are several theoretical methods to calculate the aerodynamic properties of the leading-edge vortex. Earlier, there was the Smith method<sup>[1]</sup>, which was based on a slender body assumption. Therefore, the trailing-edge conditions cannot be satisfied. The leading-edge suction analogy (and its extensions) is a relatively simple and accurate method to calculate the forces and moments on the entire wing. However, it does not provide a detailed load distribution<sup>[2]</sup>. In reference [3], the vortex lattice method was extended to wings with leading-edge separation. Several discrete vortex lines were used to represent the actual leading-edge vortex with a nucleus. The force and moment thus calculated are more accurate. But, the load distribution is not satisfactory. Currently, the most realistic leading-edge separation model is the free vortex sheet method which employs a continuous dipole distribution to represent the wing and the free vortex sheet, resulting in a satisfactory pressure distribution<sup>[4]</sup>. However, this method is more complicated and requires a larger computer and more computer time.

Mehrota and Lan<sup>[5]</sup> used the quasi-vortex-lattice method, which is applicable to flows without separation, on wings with leading-edge separation<sup>[6]</sup>. This method divides the wing along its span into several narrow strips. Each narrow wing strip is replaced by a continuous vortex sheet. The leading-edge separation vortex is represented by the discrete vortex line added onto the vortex sheet as well as from the leading-edge and trailing-edge. The special feature of this method is that boundary conditions can be met at the leading-edge through a theoretical treatment of singular points on the leading-edge. In addition, it is capable of taking leading-edge separation into account. The latter may be an appropriate method to calculate a wing strip where separation of the inner wing is different from that of the outer wing. Besides, this method maintains the relative simplicity of the vortex lattice method. In the meantime, it also gives more satisfactory results.

In this paper, the theory in reference [5] is used to calculate a flat delta wing with complete leading-edge separation on a FELIX C-256 computer. Furthermore, the results are compared with experimental data.

## II. Calculation Method

### 1. Calculation Model

For a large backward sweep thin delta wing, an attached vortex sheet represents the wing surface. The discrete free vortex line is used to represent the separated leading-edge

vortex sheet and the tail vortex sheet in order to simultaneously satisfy the airfoil condition, the leading-edge and trailing-edge boundary conditions, and the conditions that no force is exerted on the leading-edge and tail vortices. Figure 1 shows the distribution of attached vortex elements and tail vortex elements. The positions of attached vortex elements in the chord and span direction follow the cosine law, i.e.

$$x_i = x_1 + \frac{c}{2}(1 - \cos \theta_i) \quad (1)$$

This paper was received on June 9, 1984.

$$\theta_k = \frac{2k-1}{2} \frac{\pi}{N}, \quad k=1, 2, \dots, N \quad /22$$

$$y_j = \frac{b}{4}(1 - \cos \varphi_j) \quad (2)$$

$$\varphi_j = \frac{2j-1}{2} \frac{\pi}{M}, \quad j=1, 2, \dots, M$$

where  $x_1$  is the x coordinate of the leading-edge of the wing,  $c$  is the local chord length,  $N$  is the number of vortex elements along the chord direction,  $b$  is the span length and  $M$  is the number of longitudinal vortex elements parallel to the plane of symmetry. The longitudinal vortex elements divide the half wing into  $(M-1)$  strips parallel to the plane of symmetry along the span direction. The vortex density  $\gamma$  is continuous along the chord direction in every narrow strip. In the same narrow strip, the value of  $\gamma$  along the span direction remains unchanged.

The position of the control point  $(x_{cp}, y_{cp})$  is also determined according to the law of cosine:

$$x_{cp,i} = x_1 + \frac{c_i}{2} \left(1 - \cos \frac{i\pi}{N}\right), \quad i=0, 1, \dots, N \quad (3)$$

$$y_{cpj} = \frac{b}{4} \left( 1 - \cos \frac{j\pi}{M} \right), \quad j=1, 2, \dots, (M-1) \quad (4)$$

where  $x_{1j}$  and  $c_j$  are the x-coordinate of the leading-edge and chord length at  $y_{cpj}$ . When  $i = 0$ , the control point is the leading-edge. When  $i = N$ , the control point is in the trailing-edge.

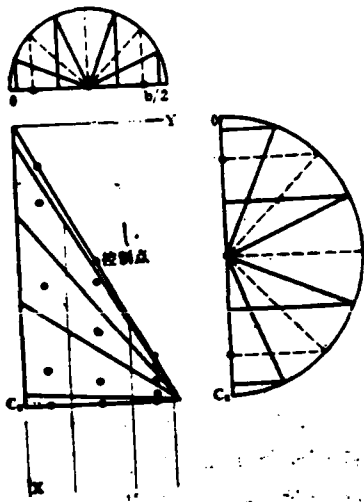


Figure 1. Distribution of Attached Vortex Elements and Tail Vortex Elements on the Wing

1. control point

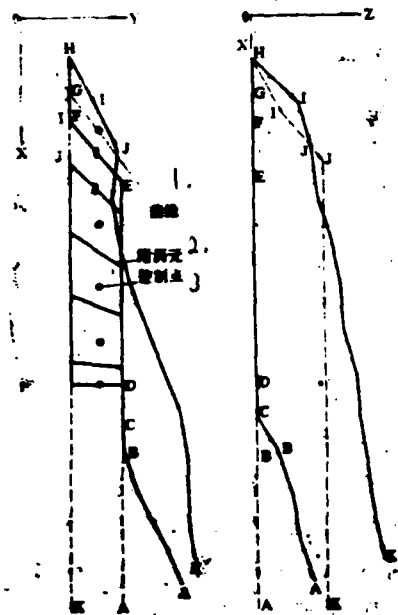


Figure 2. A Typical Leading-edge Free Vortex Element

1. leading-edge
2. attached vortex element
3. control point

The initial leading-edge vortex is added to the attached vortex lattice. Figure 2 shows a typical leading-edge vortex element AK on a narrow strip of the wing. The free vortex element consists of many broken vortex segments. The dotted line represents the initial position and the solid line indicates the final position. A and K are a chord length  $C_R$  away from the trailing-edge. The vortex line directions from infinity to A and that from K to infinity coincide with the direction of the incoming flow. The initial position of each segment of vortex line can be determined as follows:

(1) Initially, AE is in the same direction as that of attached longitudinal vortex element. Segment DE is fixed on

/23

the wing plane. BC and CD are  $0.1C_R$ . In order to meet the trailing-edge contact condition, CD is fixed on the wing plane and BC is only allowed to vary in the x-z plane.

(2) EF is on the wing plane. It is located between the leading-edge and the first attached vortex element. It is located in the position equivalent to the first vortex element position which divides the attached vortex into  $(N+1)$  elements in the chord direction i.e.

$$x_E = x_{IE} + \frac{C_E}{2} \left[ 1 - \cos \frac{\pi}{2(N+1)} \right]$$

$$x_F = x_{IF} + \frac{C_F}{2} \left[ 1 - \cos \frac{\pi}{2(N+1)} \right]$$

(3) FH is on the wing plane, in the same direction as another longitudinal attached vortex element. G is the leading-edge. In order to satisfy the leading-edge boundary condition, GH is also fixed in the wing plane.

(4) HK is rolled up into the leading-edge vortex on top of the wing by the end of the computation. Its initial position is in the plane parallel to the plane of symmetry. The initial position of I is:

$$x_1 = -x_H, \quad y_1 = y_H$$

$$z_1 = 0.1C_R \tan(22.5 - 0.5a) \quad \text{when } a \leq 15^\circ$$

or 
$$z_1 = 0.1C_R \tan a \quad \text{when } a \geq 15^\circ$$

IJ is in the flow direction. The height of J above the wing is approximately  $0.1C_R$ . JK is parallel to the wing.

## 2. Boundary Conditions and Solution

As described above, the wing surface is divided into  $(M-1)$  strips. Each one has  $N$  unknown attached vortex elements and

one unknown leading-edge vortex element. There are a total of  $(N+1)(M-1)$  unknowns. There are  $(N+1)$  control points on each strip. The total number of control points is also  $(N+1)(M-1)$ . Boundary conditions are met at each control point. When the control point is not on the leading-edge, the boundary condition should be

$$[A_{ij}]\{\gamma_j\} + [B_{ij}]\{\Gamma_j\} = \{-\sin \alpha\} \quad (5a)$$

If it is on the leading-edge, then based on reference [5], the equation is

$$[A_{ij}]\{\gamma_j\} + [B_{ij}]\{\Gamma_j\} = \{a_{1i} - \sin \alpha\} \quad (5b)$$

where  $A_{ij}$  and  $B_{ij}$  are the aerodynamic effect coefficients, attached vortex element and leading-edge vortex element, respectively.  $\gamma$  is the density of attached vortex elements and  $\Gamma$  is the condition of the leading-edge vortex element.  $a_{1k}$  is a parameter related to the leading-edge suction coefficient. From reference [5]

$$a_{1i} = N \sqrt{\tan^2 \Lambda + \beta^2} \left( \frac{2c_{t,i} \cos \Lambda}{\pi \sqrt{1 - M_\infty^2 \cos^2 \Lambda}} \right)^{\frac{1}{2}} \quad (6)$$

where  $M_\infty$  is the Mach number of the flow,  $\beta^2 = \sqrt{1 - M_\infty^2}$ ,  $\Lambda$  is the leading-edge swept back angle of the wing, and  $C_t$  is the cross-sectional leading-edge suction coefficient which can be predicted in advance. If the leading-edge is completely separated,  $C_t$  is zero everywhere, then  $a_{1k} = 0$ .

Because the density of the attached vortex elements as well as the intensity and position of the leading-edge vortex are not known, it is required to solve the equation by iteration. The position of the free vortex is adjusted in the solution finding process to make the direction of each vortex segment the same as

that of the flow velocity at the center. There are two standards for judging the convergence of the solution. One is the free vortex is subject to the least amount of force in continuous iterations and the other is that the circulation of the free vortex does not vary by more than 2% in two consecutive calculations. If these two points are satisfied, then it is the solution we are looking for.

### 3. Load Computation

/24

The load on the attached vortex segment in the span direction and the load on both ends caused by longitudinal vortices are first calculated. Then, the latter is added to the calculation of points in the span vortex segments. The load on a point along the chord can be obtained by Fourier series expansion.

### III. Comparison of Computation with Experiments

In this work we calculated a delta wing with a  $74^\circ$  sweep back, with leading edge totally separated and with  
 $M_\infty = 0$ . We choose  $N=6$  and  $M=10$ . The length of the free vortex segment is  $0.15C_R$ . We calculated three attack angles. In Figures 3 to 6, comparisons of calculated values to experimental data are given. The experimental data was taken from reference [7]. When the attack angle is  $10^\circ$  and  $20^\circ$ , calculated lift agrees with the experimental value. When the attack angle is  $30^\circ$ , the calculated value is on the low side. On the curve of moment, results at all these attack angles agree very well with the experimental data.

As for the cross-section load distribution in the span direction, calculated results are generally in agreement with the experimental results near the trailing-edge. Near the leading-edge, the calculated peak  $\Delta C_p$  is lower than the experimental value. Furthermore, the position is closer to the root. This is due to the replacement of the actual concentrated vortex by discrete vortices. The aspect ratio of the wing calculated in this work is relatively small (aspect ratio = 1.147). If the lattices in the span direction can be increased, the calculation may be improved.

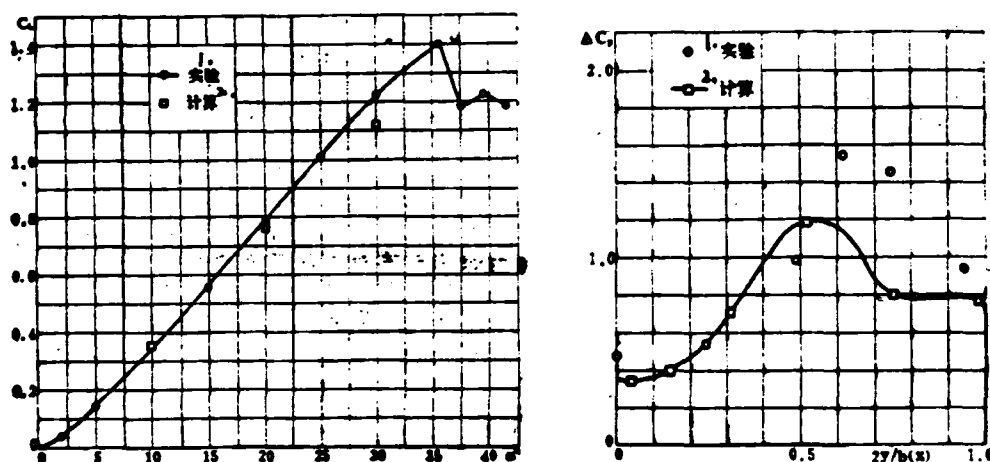


Figure 3. Comparison of Calculated and Experimental Lift Curve

1. experimental
2. calculated

图3 升力曲线的计算值与实验结果的比较

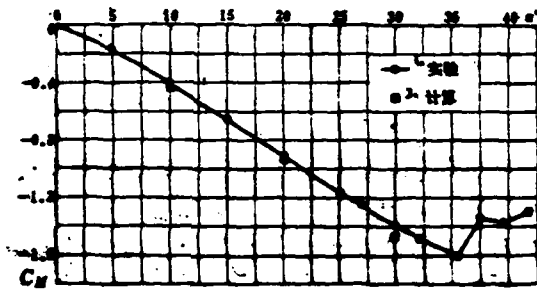


Figure 4. Comparison of Calculated and Experimental Moment Curve

- 1. experimental
- 2. calculated

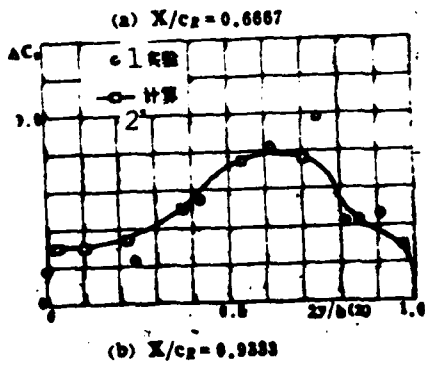


Figure 5. Distribution of  $\Delta C_p$  in the Span Cross-section,  $\alpha=20^\circ$

- 1. experimental
- 2. calculated

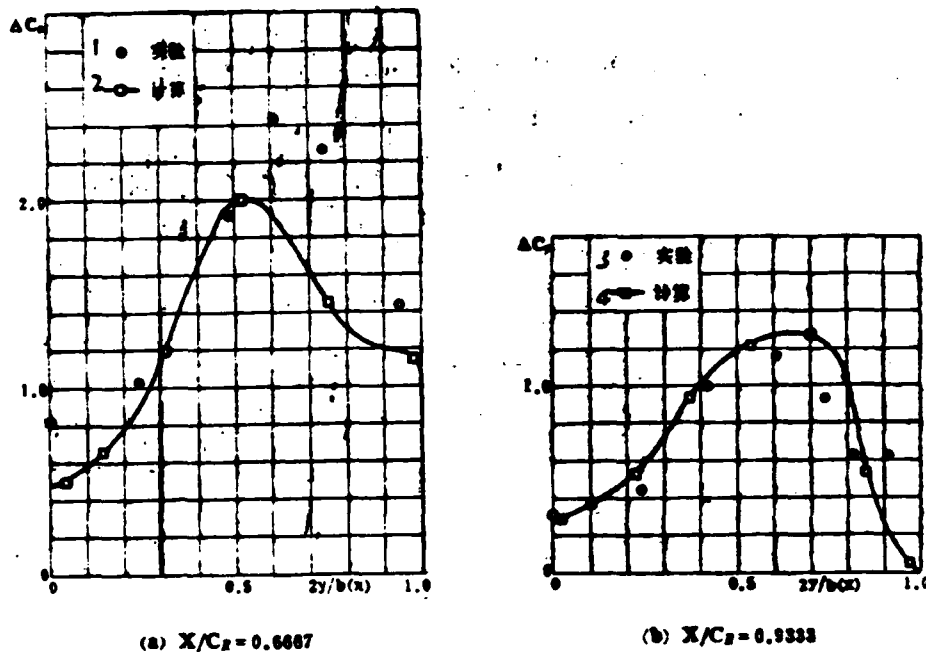


Figure 6. Distribution of  $\Delta C_p$  in the Span Cross-section,  $\alpha=30^\circ$

1. experimental
2. calculated
3. experimental
4. calculated

#### References

- [1] Smith, J.H.B., Proc. Roy. Soc., A 306 (1968), 67-90.
- [2] Polhamus, E.C., NASA TN D-3767 (1966).
- [3] Kandil, O.A., Mook, D.T. and Nayfeh, A.H., AIAA Paper No. 74-503 (1974).
- [4] Brune, G.W., Weber, J.A., Johnson, F.T., Lu, P. and Rubbert, P.E., NASA CR-132709 (1975).
- [5] Lan, C.E., J. Aircraft, 11, 9(1974), 518-527.

- [6] Mehrotra, S.C. and Lan, C.E., NASA CR-145304 (1978).  
[7] Wentz, W.H., Jr., NASA CR-2002 (1972).

**A CALCULATION OF SLENDER DELTA WING  
WITH LEADING-EDGE SEPARATION BY  
QUASI-VORTEX-LATTICE METHOD**

Xiong Shanwen

*(Beijing Institute of Aeronautics and Astronautics)*

**Abstract**

The Quasi-Vortex-Lattice method (QVLM) which was used calculating the thin wing without separation has been extended to calculate the slender delta wing with leading-edge separation. The advantage of this method is that the leading-edge boundary condition can be exactly satisfied. It can be used to predict aerodynamic characteristics of wings having partial leading-edge separation. A calculation has been made here for a slender delta wing with complete leading-edge separation and the results are compared with the experimental data. The comparison shows that QVLM can give satisfactory or reasonable results.

Zhu Peiye (Institute of Computer Technology, China Aviation  
Institute)

### Abstract

A panel method was developed in this work to calculate the aerodynamic force on a three-dimensional wing with separation vortices. The model used is simple and visual. Furthermore, it is suited for any arbitrary planform wings with different profiles. This method employs a planar quadrilateral lattice as well as another lattice formed by a parallelogram and four non-coplanar triangles. A second order doublet sheet distribution is arranged on each lattice in order to ensure a high accuracy. Examples used include a rectangular wing and a sweptback wing. Calculated results were compared with available experimental data and other theoretical results. They were found in satisfactory agreement.

### I. Introduction

A separation vortex type of aerodynamic distribution is often used for fighters and it will be used in the near future<sup>[1]</sup>. In this layout, the flow is separated at the leading edge of the wing tip. A separation vortex is created. It flows downstream from the upper side of the wing. This separation vortex has a great effect on the pressure distribution on the wing, resulting

in the non-linear rise of the lift coefficient with increasing angle of attack. The aerodynamic properties of the aircraft can be significantly improved if this phenomenon can be effectively controlled and utilized. The maneuverability will be improved dramatically. The typical examples include the slender delta wing, side strip wing and close range coupled duck wing layout.

In recent years, some work was done to calculate the aerodynamic load on a wing with separated vortices and the geometric positions of separation vortices. For instance, Belotserkovskii<sup>[2]</sup>, Rehback<sup>[3]</sup> and Kandil<sup>[4]</sup>, used a so-called vortex lattice method, together with a relaxation technique, to calculate the aerodynamic load on a thin wing at a large attack angle and the positions of separation vortices. In their calculations, the wing was replaced by an arc with vortex circles (equivalent to constant doublet distribution). Discrete vortex lines are used to represent the free vortex sheet, in approximation. The authors also employed similar method to calculate the aerodynamic force on a ultrathin large attack wing with very good results<sup>[5,6]</sup>. This type of method is simple. But, it only considers a thin wing and cannot calculate the pressure distribution on the wing. Johnson et al at Boeing<sup>[7]</sup> introduced a panel method to calculate a thick three-dimensional wing. In their model, the separation vortex consists of the free vortex sheet, vortex core and a cross-section connecting the two across which the free vortex is transported to the vortex core.

A first order source distribution was used for the middle surface of the wing as well as for free vortex sheets. In addition, a second order curved lattice was used to provide their method with a higher accuracy. A very good pressure distribution was obtained. However, we can see that their calculation method is more complex and requires more computer time.

In this work, a method is developed to calculate the aerodynamic load of a three-dimensional thick wing at large attack angles. In this method, the wing surface is divided into lattices. Furthermore, a second order doublet distribution is employed. The free vortex sheet is represented by broken discrete-free vortex line in approximation.

---

This paper was received on March 20, 1984. Revised manuscript was received on May 31.

As compared to Boeing's method, this separation vortex model is <sup>128</sup> simple. It does not require any geometric data on the middle plane of the wing. There is also no need to calculate the concentrated source effect index. It not only is applicable to various wing profiles but also has a satisfactorily high accuracy.

## II. Mathematical Approach of the Problem

The steady, in viscous and incompressible potential flow of a three-dimensional thick wing is considered. It is assumed that the wing tip has a sharp edge. When there is lift, the air flow will be separated at the wing tip to create a separation vortex.

As we all know, this problem satisfies the Laplace equation. The boundary conditions are that the wing surface  $S_W$  and free vortex sheet  $S_V$  are unpenetratable, the pressure on either side of the free vortex sheet is equal, the perturbation velocity at infinity is zero and the Kutar condition on the trailing edge and line of separation. Notice that the shape of the free vortex sheet is not known in advance. Therefore, this is a second boundary value problem with a position of the boundary unknown. This unknown boundary must be solved by using an iteration method as a part of the solution to the problem. From Green's formula we know that the solution to the problem may be expressed by a surface integral of a source concentration density  $\sigma$  and a doublet density  $\mu$ . In this work, only a doublet surface distribution is employed. By taking the unpenetratable boundary condition into consideration, we get the following integral equation

$$-\vec{V}_\infty \cdot \vec{n} = -\frac{1}{4\pi} \iint_S \mu(Q) \frac{\partial}{\partial n} \left[ \frac{\partial}{\partial n_0} \left( \frac{1}{r} \right) \right] dS_0 \quad (1)$$

where  $\iint$  indicates that the Cauchy principal value is chosen for the integral,  $S = S_W + S_V$ ,  $\vec{V}_\infty$  is the free flow velocity, and  $\vec{n}$  is the unit external normal vector. This is obviously much simpler than using  $\sigma$  and  $\mu$  simultaneously. As for other methods involving simultaneously using  $\sigma$  and  $\mu$  and a comparison of their results, one can read reference [8].

### III. Numerical Method

#### 1. Approximation of Wing Surface and Free Vortex Sheet

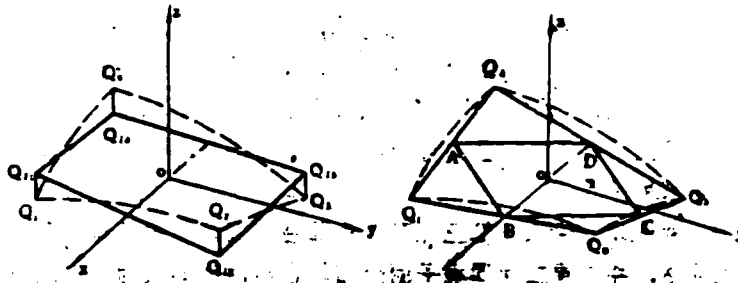


Figure 1. Two Types of Lattices of Approximate Wing Surface Area Element

- (a) parallelogram lattice
- (b) non-coplanar plane combination lattice

The wing surface is divided into many small parallelogram area elements (lattices). Each element is approximated by a parallelogram or by a non-coplanar combination comprised of four triangles. Figure 1a shows the parallelogram  $Q_{11}, Q_{12}, Q_{13}, Q_{14}$ . It is parallel to two diagonals  $Q_1Q_3$  and  $Q_2Q_4$  of the surface element  $Q_1Q_2Q_3Q_4$  on the wing surface. Furthermore, it is at the same distance away from them. Figure 1b shows a parallelogram ABCD. The apices are located in the middle of the lines /29 connecting the quadrilateral  $Q_1Q_2Q_3Q_4$ . This parallelogram and the four triangles,  $\Delta ABQ_1$ ,  $\Delta BCQ_2$ ,  $\Delta CDQ_3$  and  $\Delta DAQ_4$ , are combined to create the approximate area element  $Q_1Q_2Q_3Q_4$ . Obviously, the former is simple and easy to calculate. But, the accuracy is not very high. It is usually used when the curvature of the wing surface is not very large. The latter is more complicated.

However, it can more accurately approximate the wing surface, especially in large curvature areas such as the leading edge, side and trailing edge. Furthermore, it also ensures the continuity of the geometric shape. In this work, this method is used to approximate the wing surface, not only to attain certain accuracy but also to ensure that the calculation is not too complicated.

According to Helmholtz theory, the intensity of a free vortex sheet remain unchanged downstream. Therefore, it is possible to turn a free vortex sheet into a discrete vortex lines of equal intensity. These vortex lines should be stream lines. In numerical computation, they are approximated by broken lines. The last segment is a semi-infinite line parallel to the free flow velocity.

## 2. Second Order Doublet Sheet Distribution

A second order doublet sheet distribution is arranged on each lattice

$$\mu(x,y) = \mu_0 + \mu_x x + \mu_y y + \mu_{xx} x^2 + \mu_{xy} xy + \mu_{yy} y^2 \quad (2)$$

where  $(x,y)$  is the local right angle coordinate on the lattice. The origin is at the center of the lattice. Hence,  $\mu_0$  is the value of the doublet distribution at the center. This value is chosen to be the discrete unknown of the problem. Other coefficients such as  $\mu_x$ ,  $\mu_y$ , ...,  $\mu_{yy}$  are not independent. They are expressed as a linear combination of discrete unknowns on two neighboring lattices.

$$\mu_x = \sum_{i=1}^n b_{x,i} \mu_i, \quad \mu_y = \sum_{i=1}^n b_{y,i} \mu_i, \quad \dots, \quad \mu_{yy} = \sum_{i=1}^n b_{yy,i} \mu_i \quad (3)$$

where  $\mu_i$ ,  $i=0, \dots, 8$  are the discrete unknowns of the lattice and 8 neighboring lattices.  $b_{xi}$ ,  $b_{yi}, \dots, b_{yyi}$  are constants which can be calculated by the weighted least square method.

Strictly speaking, the optimal accuracy can only be obtained by matching second order doublet distribution with a second order curved lattice. But, the curvature in most areas on the wing is usually not very large in most cases. Because a non-coplanar combination lattice is used, in addition to locally tightening the lattice, better accuracy can be obtained. Therefore, satisfactory results can also be obtained by using a second order doublet distribution and a planar lattice.

### 3. Kutar Condition

With regard to the Kutar condition for the trailing edge, there are many equivalent expressions. In this method, the condition used is that the vortex intensity vector on the trailing edge is parallel to the local velocity. In general, the flow velocity at the trailing edge is nearly parallel to the wing chord. The perpendicular component of the vortex intensity vector in the span direction is equal to zero. This method does not require a new equation and does not introduce a new unknown. It is very convenient.

### 4. Formation and Solution of Linear Algebraic Equations

The surface integral on the right hand side of the discrete approximation formula (1) discussed above is used to obtain a series of linear algebraic equations to find the discrete unknown  $\mu_i$  by letting this equation be satisfied at all lattice

centers (i.e., control points).

$$\sum_{i=1}^N a_{ij} \mu_i = b_j, \quad i=1, \dots, N \quad (4)$$

where  $N$  is the number of wing surface lattices and  $a_{ij}$  is the influencing coefficient. Notice that the kernel of the integral (1) has the following property

$$\iint_S \frac{\partial}{\partial n} \left[ \frac{\partial}{\partial n_0} \left( \frac{1}{r} \right) \right] dS_0 = 0 \quad (5) \quad /30$$

where  $S$  is an enclosed curve. If errors in the discretization process and numerical computation can be neglected, then the determinant of the coefficient matrix in equation (4)  $|a_{ij}| = 0$ . These equations have infinite sets of solutions differing by a constant. For this reason, we let  $\mu_N = 0$  and use the least square method to solve  $N-1$  unknowns from  $N$  equations. The linear equations are solved by the method of elimination. The method of elimination is always reliable and effective for equations of reasonable order.

##### 5. Relaxed Iteration of Free Vortex Line

If the geometric position of the free vortex is known, then the method described above can be used to find the doublet intensity distribution on the wing. By using the method of superposition, it is possible to calculate the velocity at any point in the flow field. In our problem, the geometric position of the free vortex is not known. It requires a relaxed iteration technique to simultaneously determine the doublet intensity and the geometric position of the free vortex. This relaxed iteration process can be simply described in the following.

The doublet intensity distribution is calculated by using the above method with a given initial free vortex position, i.e., given free vortex lines from the trailing edge of the wing as well as from the separation line. In the flow field defined by this doublet intensity distribution, the position of the free vortex line is corrected based on the condition that a free vortex line is a stream line in order to make it closer to the stream line. The calculation is repeated by using the corrected free vortex line as the initial value until the maximum correction of two consecutive iterations is less than a specific accuracy requirement.

#### IV. Examples

##### 1. Rectangular Wing

A symmetric rectangular wing with an aspect ratio 2, the Boeing TR17, is under consideration. The distribution of wing thickness along the span direction is

$$d(y) = 0.11 \cos \frac{\pi}{2} y, \quad y \in [0, 1] \quad (6)$$

The half wing span is divided into 4 lattices along the span and 12 lattices in the chord direction according to the law of cosine to allow the leading edge to have a tighter mesh. Thus, the half wing span has 96 lattices. Figure 2 shows the calculated separation vortex.

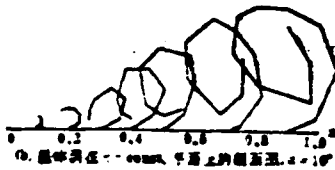
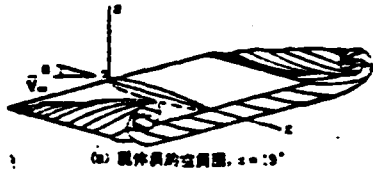


Figure 2. Side Separation Vortex of a Symmetric Rectangular Wing

- (a) separation vortex in space  $\alpha = 19^\circ$
- (b) cross-section of separation vortex across the  $x = \text{const.}$  plane,  $\alpha = 10^\circ$

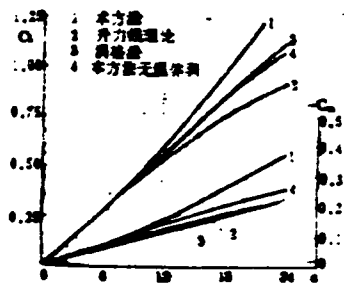


Figure 3. Lift Coefficient and Pitch Moment Coefficient of a Rectangular Wing

- 1. This work
- 2. lift line theory
- 3. vortex lattice method
- 4. this method without separation vortex

Figure 2a shows the separation vortex at an attack angle  $\alpha = 19^\circ$ . /31  
Figure 2b shows the cross-section of the separation vortex across a plane  $x = \text{const.}$  in the span direction when  $\alpha = 10^\circ$ . From these two figures one can see the curling of the separation vortex and the spatial position of the free vortex line.

Figure 3 is a comparison of total lift coefficient and total pitch moment coefficient calculated by using this method to those obtained with other methods. In the figure, curve 1 is obtained using the method, curve 2 is based on the lift line theory, curve 3 is by using vortex lattice method<sup>[9]</sup>, and curve 4 is also based on this method but without considering separation vortices. When the attack angle is small, all methods are comparable. With increasing attack angle, this method results in larger non-linear lift and pitch moment.

In order to demonstrate the adaptability of this method to various wing profiles, it was used to calculate the same wing with an asymmetric profile, the E-603 wing. The results are satisfactory. Figure 4a is the separation vortex diagram calculated at  $\alpha = 22^\circ$ . An interesting result was obtained when we calculated the situation that  $\alpha = 10^\circ$ . In this example, the wing tip is not straight. Instead, it is the middle arc of the E-603 profile. At the leading edge, this middle arc has a local angle of attack  $\beta = 20^\circ$  and since  $\alpha = 10^\circ$ , a local negative angle of attack of approximately  $-10^\circ$  occurs at the leading edge. Therefore, the separation begins curling outward and does not curl inward as under normal conditions. The cross-sectional view of the separation vortex on the  $x = \text{const.}$

plane shown in Figure 4b clearly illustrates this point. Each cross-sectional curve begins with an outward curl and then curls inward (as compared to Figure 2b). This shows that our method can be used to calculate complicated separation vortices.

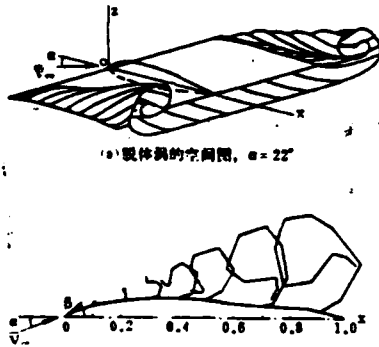


Figure 4. Side-fringe Separation Vortex of a Rectangular Wing With Asymmetric Profile

- (a) spatial diagram of separation vortex,  $\alpha = 22^\circ$
- (b) cross-section of separation vortex at  $x = \text{const.}$ ,  
 $\alpha = 10^\circ$

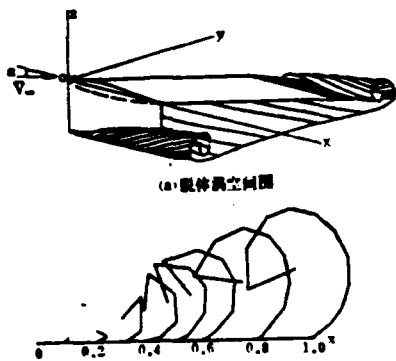


Figure 5. Wing Top Separation for a  $45^\circ$  Sweepback Wing With Aspect Ratio 2 at  $\alpha = 10^\circ$

- (a) spatial diagram of separation vortex
- (b) cross-section of separation vortex on  $x = \text{const.}$  plane

## 2. Sweepback Wing

Let us consider an equal chord length,  $45^\circ$  sweepback wing with an aspect ratio of 2. This wing has the same profile and span thickness distribution as those for the above rectangular wing. Figure 5a shows the spatial shape of the calculated separation vortex at  $\alpha = 10^\circ$ . Figure 5b shows the cross-section of this vortex on the  $x = \text{const.}$  plane. We can see that this method is also capable of calculating the geometric shape of the wing top separation vortex of a sweepback wing.

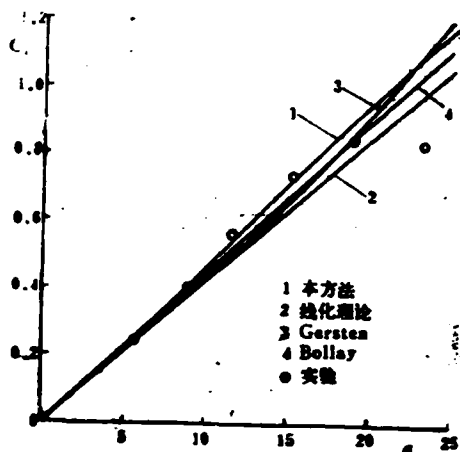


Figure 6. Total Lift Coefficient of the Sweepback Wing

- 1. this method
- 2. linearization theory
- o experimental

Figure 6 shows the calculated total lift coefficient of the sweepback wing (curve 1) and compared it with results obtained using other methods, as well as with experimental data. Curve 2 is based on a linearization theory, curve 3 is based on Gersten's theory, and curve 4 is based on Bollay's theory. These /32 theoretical results and the experimental data are directly brought over from Reference [10]. At small attack angles, all theoretical results are in agreement with the experimental data. At medium attack angles, the results obtained with this method fit the data better. As the attack angle further increases, such as greater than 20°, all theoretical results deviate

significantly from the experimental data. This may be due to the breakage of the separation vortex over the wing in the experiment which leads to a rapid drop of the lift.

## V. Conclusion

In this work, a panel method was developed to calculate the flow around a three-dimensional thick wing with separation vortices. This method employs a simple model and is applicable to any arbitrary planar wing of various profiles as long as the wing has sharp fringes. Examples shown in this paper indicate that the accuracy of calculated results is satisfactory.

The method not only can be used to calculate the flow around a thick wing with separation vortices, but also can be extended to complicated situations such as leading edge separation vortex and leading and trailing edge interference of a slender wing. For a smooth body with symmetric separation vortices, such as the fuselage and missile head, as long as the position of the separation line is known, this method can also be used to perform the calculation. By using the Planck-Glow theory, this method can easily be extended to calculate a subsonic subcritical flow.

## Appendix

This work was completed by the author at the Institute of Mechanics at Stogadtt University in West Germany. All the computations were carried out in the university computer center. The author wishes to express his gratitude to the director of the institute and his advisor Professor R. Eppler for their assistance.

## References

- [1] Ji Xiumei, "Aerodynamic Layout of Fighters in the 90's", Institute of Technical Information of the Ministry of Aerospace Industry, 1983.
- [2] Belotserkovskii, S.M., NASA TTF 12/291, 1969.
- [3] Rehbach, C., AIAA J. 14, 253-5, 1976.
- [4] Kandil, O.A., Mook, D.T. & Nayfeh, A.H., J. Aircraft, 13, 22-8, 1976.
- [5] Zhu Peiye and Shou Wenxi, Journal of Aeronautics, <sup>12-21</sup>4 (1978).
- [6] Zhu, P.Y., Shou, W.X. & Luo, S.J., Computer Methods in Applied Mechanics and Engineering, Vol. 26, 305-19, 1981.
- [7] Johnson, F.T., Tinoco, E.N., Lu, P. & Epton, M.A., AIAA Paper 79-0282, 1979.
- [8] Johnson, F.T., NASA CR 3079, 1980.
- [9] Maskew, B., N71-20115 (Loughborough TT 7009), 1970.
- [10] Sacher, P., DGLR 78-221, 1978.

Zhu Peiye

(Institute of Computing Technology, CAE)

## Abstract

The present paper has developed a panel method predicting the non-linear aerodynamic loads on thick wings with separation vortices. The model used is simple and visual. The method can be used for arbitrary planform wings with different profiles. Planar quadrilateral panel and panel that consists of a parallelogram and four triangles are used. In order to obtain a high accuracy, the wing is represented by piecewise continuous quadratic doublet sheet distributions. The aerodynamic loads on rectangular wing and sweepback wing are computed. They agree well with experimental tests and other theories.

The Split Coefficient Matrix Difference Method for Supersonic  
Three-dimensional Flow

141

Zhang Lumin and Shan Xiaonan

(China Aerodynamic Research and Development Center)

Abstract

In this paper, a split coefficient matrix (SCM) difference method is introduced to calculate the inviscid steady flow over a non-symmetric three-dimensional body. This method is based on the mathematical theory of characteristics. In the split coefficient difference method, the coefficients are split according to the slope of the characteristic line. These coefficients are multiplied by an appropriate unidirectional difference. The forward difference is related to the negative characteristic value. The backward difference is related to the positive characteristic value.

A blunt spherical cone is used as an example in this paper. Furthermore, we compared this method with reference [2] and found that the SCM can still maintain a high accuracy with few meshes.

I. Basic Equations

In the cylindrical coordinate  $0-zr\varphi$ , let us assume that the body surface and shock wave surface are respectively expressed as:

$$r_b = r_b(z, \varphi) \quad r_s = r_s(z, \varphi)$$

Let us introduce the following transformation

$$z = z, \quad \xi = \frac{r - r_b}{r_s - r_b}, \quad \Phi = \varphi$$

where  $r, z, \varphi$  represent the radial, axial and circumferential coordinate of the cylindrical coordinate, respectively.  $r_b$  and  $r_s$  are the body and shock wave radial coordinates.

By making the variables dimensionless, i.e., dividing  $p$  and  $\rho$  by flow parameters  $p_\infty$  and  $\rho_\infty$ , dividing velocity by  $\sqrt{p_\infty/\rho_\infty}$ , and by dividing lengths such as  $z$  and  $r$  by the radius of the blunt  $R_N$ , the three-dimensional inviscid steady Euler equations are

$$\begin{aligned} Ad_t + Bd_r + Cd_\Phi + D &= 0 \\ u^2 + v^2 + w^2 + \frac{2\gamma}{\gamma-1} \frac{p}{\rho} &= C_1 \\ C_1 &= \gamma M_\infty^2 + \frac{2\gamma}{\gamma-1} \end{aligned} \quad (1)$$

where  $u, v, w$  are the axial, radial and circumferential velocity components,  $\gamma$  is the specific heat,  $p$  is pressure and  $\rho$  is density.

$$d = (u, v, w, p)^T$$

$$A = \begin{bmatrix} \rho u^2 & 0 & 0 & u \\ \rho u v & 0 & 0 & v \\ 0 & \rho u w & 0 & w \\ 0 & 0 & \rho u & 0 \end{bmatrix}$$

This paper was received on January 9, 1984. Revised manuscript was received on May 22.

$$B = \begin{bmatrix} \rho a^2 \xi_r & \rho a^2 \xi_z & \frac{1}{r} \rho a^2 \xi_\phi & \bar{U} \\ \rho \bar{U} & 0 & 0 & \xi_r \\ 0 & \rho \bar{U} & 0 & \xi_z \\ 0 & 0 & \rho \bar{U} & \xi_\phi / r \end{bmatrix}$$

$$C = \begin{bmatrix} 0 & 0 & \frac{1}{r} \rho w^2 & \frac{w}{r} \\ \frac{1}{r} \rho w & 0 & 0 & 0 \\ 0 & \frac{1}{r} \rho w & 0 & 0 \\ 0 & 0 & \frac{1}{r} \rho w & \frac{1}{r} \end{bmatrix}$$

$$D = \begin{bmatrix} \frac{1}{r} \rho a^2 v \\ 0 \\ -\frac{1}{r} \rho w^2 \\ \frac{1}{r} \rho w w \end{bmatrix}$$

$$\bar{U} = u \xi_r + v \xi_z + \frac{w}{r} \xi_\phi$$

$$\xi_r = \xi_z [(\xi - 1) r_{,z} - \xi r_{,z}]$$

$$\xi_\phi = \frac{1}{r_1 - r_2}$$

$$\xi_\phi = \xi_z [(\xi - 1) r_{,\phi} - \xi r_{,\phi}]$$

$r_{bz}$ ,  $r_{b\phi}$ ,  $r_{sz}$  and  $r_{s\phi}$  are first derivatives of  $r_b$  or  $r_s$  with respect to the subscript.  $\xi_r$ ,  $\xi_z$  and  $\xi_\phi$  are first derivatives of with respect to the subscript.

## II. Split Coefficient Equation

The Euler equation (1) is hypobolic. Hence, there exists a similarity transformation which can be written as

$$d_t + A^{-1} T A_{Bz} T^{-1} A d_t + A^{-1} S A_{\phi\phi} S^{-1} A d_\phi + A^{-1} D = 0$$

$$\bar{B} = A^{-1} B = A^{-1} T A_{Bz} T^{-1} A$$

$$\bar{C} = A^{-1} C = A^{-1} S A_{\phi\phi} S^{-1} A$$

Let

$\Lambda_{BA}$  and  $\Lambda_{CA}$  are diagonal matrices formed by the characteristic values  $\lambda^{\bar{B}}$  and  $\lambda^{\bar{C}}$  of matrices  $\bar{B}$  and  $\bar{C}$ , respectively.

$$\Lambda_{BA} = \text{diag}(\lambda_1^{\bar{B}}, \lambda_2^{\bar{B}}, \lambda_3^{\bar{B}}, \lambda_4^{\bar{B}})$$

$$\Lambda_{CA} = \text{diag}(\lambda_1^{\bar{C}}, \lambda_2^{\bar{C}}, \lambda_3^{\bar{C}}, \lambda_4^{\bar{C}})$$

$$\lambda_1^{\bar{B}} - \lambda_2^{\bar{B}} = \bar{U}/u$$

$$\lambda_{3,4}^{\bar{B}} = \frac{1}{u^2 - a^2} \left[ (u\bar{U} - a^2 \xi_0) \pm a \sqrt{\left(u\xi_0 + \frac{w}{r} \xi_0\right)^2 + (u^2 - a^2) \left(\xi_0^2 + \frac{\xi_0^2}{r^2}\right)} \right] \quad /43$$

$$\lambda_1^{\bar{C}} - \lambda_2^{\bar{C}} = w/ru$$

$$\lambda_{3,4}^{\bar{C}} = \frac{1}{r(u^2 - a^2)} (uw \pm a \sqrt{u^2 + w^2 - a^2})$$

$\lambda_3^{\bar{B}}$  and  $\lambda_3^{\bar{C}}$  correspond to the "+" sign and  $\lambda_4^{\bar{B}}$  and  $\lambda_4^{\bar{C}}$  correspond to the "-" sign.

$$T^{-1} = \begin{bmatrix} 1 & 1 & -\frac{(\xi_0 - \lambda_1^{\bar{B}})}{\xi_0} & 0 \\ 0 & 0 & \frac{\xi_0}{r\xi_0} & 1 \\ \frac{\bar{U} - \lambda_3^{\bar{B}} u}{a^2} & -(\xi_0 - \lambda_3^{\bar{B}}) & -\xi_0 & -\frac{\xi_0}{r} \\ \frac{\bar{U} - \lambda_4^{\bar{B}} u}{a^2} & -(\xi_0 - \lambda_4^{\bar{B}}) & -\xi_0 & -\frac{\xi_0}{r} \end{bmatrix}$$

$$S^{-1} = \begin{bmatrix} 0 & 1 & 1 & \frac{w}{u} \\ 0 & 1 & -1 & \frac{w}{u} \\ \frac{w}{r} - \lambda_1^{\bar{C}} u & a^2 \lambda_1^{\bar{C}} & 0 & \frac{-a^2}{r} \\ \frac{w}{r} - \lambda_2^{\bar{C}} u & a^2 \lambda_2^{\bar{C}} & 0 & \frac{-a^2}{r} \end{bmatrix}$$

By using the inverse  $T^{-1}$  and  $S^{-1}$ , we can obtain  $T$  and  $S$ .

Based on the sign of the characteristic value, the diagonal matrix  $\Lambda$  can be divided into two parts;  $\Lambda_+ = \Lambda_+ + \Lambda_-$  where  $\Lambda_+$  is only  $\lambda > 0$  and  $\Lambda_-$  for  $\lambda < 0$ .

Therefore, the split coefficient matrix can be separated as

$$\bar{B} = A^{-1} T \Lambda_{BA} T^{-1} A + A^{-1} T \Lambda_{BA} T^{-1} A = \bar{B}_+ + \bar{B}_-$$

$$\bar{C} = A^{-1} S \Lambda_{CA} S^{-1} A + A^{-1} S \Lambda_{CA} S^{-1} A = \bar{C}_+ + \bar{C}_-$$

The split coefficient equation for the three-dimensional steady Euler equation is:

$$d_t + \bar{B}_b d_{t_b} + \bar{B}_f d_{t_f} + \bar{C}_b d_{\theta_b} + \bar{C}_f d_{\theta_f} + A^{-1} D = 0 \quad (2)$$

The subscript b represents the backward difference and f represents the forward difference. The above equation is an interior point calculation equation.

### III. Boundary Treatment

#### (1) Body Surface Boundary ( $\xi = 0$ )

Based on the steady Euler equation (2), the characteristic compatibility relation is established as follows: /44

$$T^{-1} d_t + T^{-1} \bar{B}_b d_{t_b} + T^{-1} (\bar{C}_b d_{\theta_b} + \bar{C}_f d_{\theta_f}) + T^{-1} A^{-1} D = 0$$

On the body surface, the impermeable condition should be satisfied:

$$\bar{U} = 0 \quad \lambda_{1,1}^{\bar{b}} = 0$$

The negative characteristic value  $\lambda_4^{\bar{b}}$  should be taken according to the physical significance. Using  $\partial p / \partial z$  as an example:

The split coefficient expansion is:

$$p_z = -(\lambda_4^{\bar{b}} p_{t_b} + g_z) - \frac{\rho u_{t_b}^2}{A} \left\{ \left( r_{t_b} u_{t_b} + \frac{r_{t_b \theta}}{r_b} w_{t_b} \right) \lambda_4^{\bar{b}} + \left( r_{t_b} g_z - g_z + \frac{r_{t_b \theta}}{r_b} g_z \right) - \left[ u r_{t_b z} + \frac{w}{r_b} \left( r_{t_b \theta} - \frac{r_{t_b \theta} r_{t_b z}}{r_b} \right) \right] \right\}$$

where

$$A = \lambda_4^{\bar{b}} \left( 1 - \frac{u^2}{a^2} \right) + \dot{s}_z r_{t_b}$$

$$\bar{g} = (g_z, g_z, g_z, g_z)^T$$

$$\bar{g} = (\bar{C}_b d_{\theta_b} + \bar{C}_f d_{\theta_f}) + A^{-1} D$$

The subscripts b and f represent the backward and forward difference, respectively.

(2) Shock Wave Boundary ( $\xi = 1$ )

On the shock wave surface, the Rankine-Hugoniot relation is used:

$$v_{,1} = \frac{\gamma+1}{2} p + \frac{\gamma-1}{2}$$

$$\rho = v_{,1} / (1 + v_{,1} - p)$$

$$r_{,1} = \frac{1}{u_{\infty}^2 - v_{\infty}^2} \{ u_{\infty} (v_{\infty} - w_{\infty} r_{,0} / r_0) + v_{\infty} \times$$

$$\quad \times \sqrt{(v_{\infty} - w_{\infty} r_{,0} / r_0)^2 + (u_{\infty}^2 - v_{\infty}^2) (1 + r_{,0}^2 / r_0^2)} \}$$

$$v = v_{\infty} + v_{,1} \left( 1 - \frac{1}{\rho} \right) / \sqrt{1 + r_{,1}^2 + r_{,0}^2 / r_0^2}$$

$$u = u_{\infty} (v - v_{\infty}) r_{,1}$$

$$w = w_{\infty} - (v - v_{\infty}) r_{,0} / r_0$$

$v_{n\infty}$  is the normal velocity in front of the wave.  $u_{\infty}$ ,  $v_{\infty}$  and  $w_{\infty}$  are the incoming flow velocity components.

$$u_{\infty} = \sqrt{\gamma} M_{\infty} \cos \alpha \cos \beta$$

$$v_{\infty} = -\sqrt{\gamma} M_{\infty} \sqrt{1 - \cos^2 \alpha \cos^2 \beta} \cdot \cos(\varphi - \sigma)$$

$$w_{\infty} = -\sqrt{\gamma} M_{\infty} \sqrt{1 - \cos^2 \alpha \cos^2 \beta} \cdot \sin(\varphi - \sigma)$$

$$\sigma = \text{tg}^{-1}(\text{tg} \beta / \sin \alpha)$$

$\alpha$  and  $\beta$  are the attach angle and slip angle, respectively. /45

As for pressure behind the shock wave  $p$ , the pressure characteristic compatibility relation is established by using equation (3). In this case, we should take the positive characteristic value  $\lambda_3^{\overline{B}}$ , and  $d_{\xi f}$  is changed to  $d_{\xi b}$ .

#### IV. Difference Scheme

The MacCormack second order explicit scheme is used in this work<sup>[1]</sup>. In order to adapt to the special feature of the split

coefficient method and to ensure the second order accuracy, a two point and a three point formula are used.

$$\frac{\Delta_i p}{\Delta \Phi} = \frac{p_{i+1} - p_i}{\Delta \Phi}$$

$$\frac{\nabla_i p}{\Delta \Phi} = \frac{p_i - p_{i-1}}{\Delta \Phi}$$

$$\frac{\delta_i p}{\Delta \Phi} = \frac{-2p_i + 3p_{i+1} - p_{i+2}}{\Delta \Phi}$$

$$\frac{\delta_i p}{\Delta \Phi} = \frac{2p_i - 3p_{i-1} + p_{i-2}}{\Delta \Phi}$$

If  $\Delta f$  and  $\delta_b$  are used in predicting step, then  $\nabla_b$  and  $\delta_f$  should be used in the correcting step.

#### V. Stability Condition

The step  $\Delta z$  must be limited by the stability condition. For a MacCormack explicit difference equation, stability is a necessary condition. With respect to any point in the area where solution is sought, the development region of the differential equation must be totally included in the dependent area of the difference equation, i.e.

$$\frac{\Delta \xi}{\Delta z} \geq \max_{\substack{1 \leq i \leq 7 \\ 1 \leq t \leq 4}} \{(\sigma_1)_{i,t}, (\sigma_2)_{i,t}, (\sigma_3)_{i,t}\}$$

where

$$\begin{aligned} \sigma_1 &= \frac{1}{u^2 - a^2} \left\{ |u(u\xi_s + v\xi_s + w\xi_s/r) - a^2\xi_s| + \right. \\ &\quad \left. + a\sqrt{(v\xi_s + w\xi_s/r)^2 + (u^2 - a^2)(\xi_s^2 + \xi_s^2/r^2)} \right\} \\ \sigma_2 &= \frac{1}{r(u^2 - a^2)} \frac{\Delta \xi}{\Delta \Phi} \left\{ |uw| + a\sqrt{u^2 + w^2 - a^2} \right\} \\ \sigma_3 &= \frac{1}{w^2 - a^2} \left\{ \left| u \left[ u\xi_s + v\xi_s + \frac{w}{r} \left( \xi_s + \frac{\Delta \xi}{\Delta \Phi} \right) \right] - a^2 \xi_s \right| + \right. \\ &\quad \left. + a\sqrt{\left[ v\xi_s + \frac{w}{r} \left( \xi_s + \frac{\Delta \xi}{\Delta \Phi} \right) \right]^2 + (u^2 - a^2) \left[ \xi_s^2 + \left( \xi_s + \frac{\Delta \xi}{\Delta \Phi} \right)^2 / r^2 \right]} \right\} \end{aligned}$$

Therefore

/46

$$\Delta z = \frac{\mu \Delta \xi}{\max_{\substack{1 \leq i \leq n \\ 1 \leq j \leq n}} \{(\sigma_i)_{j,j}, (\sigma_j)_{i,i}, (\sigma_j)_{i,i}\}}$$

## VI. Calculated Results and Analysis

In this paper, the equation to calculate the supersonic flow of a non-symmetric ( $r_{b\varphi} \neq 0$ ) re-entry warhead with  $\alpha$  and  $\beta$  is given. In order to explain the special feature of this method we calculated the flow fields and aerodynamic forces of a  $9^\circ$  spherical cone at  $M = 5, 7, 9$  and  $\alpha = 0^\circ, 3^\circ, 6^\circ, 9^\circ, 10^\circ$ . The results are compared to those obtained with the conventional difference method<sup>[2]</sup> (see Tables 1 and 2).

Table 1. Comparison of Pressure Coefficients  $C_p$  at  $M = 5$ ,  
 $\alpha = 0^\circ$

z(axial position) difference(27x13) difference(11x7) SCM(11x7)

30	0.0575	0.0548	0.0586
36	0.0588	0.0563	0.0598

Table 2. Comparison of Pressure Center ( $C_m/C_N$ ) at  $M = 5$ ,  
 $\alpha = 3^\circ$   
z(axial position) difference(27x13) difference(11x7) SCM(11x7)

30	0.7165	0.7200	0.7131
36	0.7114	0.7145	0.7086

From the above tables we know that the SCM method can still maintain a high accuracy with few meshes. Due to the fact that the split coefficient method has good physical significance, it is more appropriate than the conventional difference method when the transverse flow gradient is large.

#### References

- [1] Daywiff, J., AIAA 81-0115.
- [2] Zhang Lumin and Guo Zhiquan, Numerical and Approximate Calculation of Inviscid, Steady Supersonic Flow of a Non-symmetric Body with a Side Slip Angle, Journal of Aerodynamics, 4(1983).

## THE SPLIT-COEFFICIENT MATRIX METHOD FOR SUPERSONIC THREE DIMENSIONAL FLOW

Zhang Lumin    Shan Xiaonan

(China Aerodynamic Research and Development Centre)

### Abstract

The Split Coefficient Matrix (SCM) finite difference method for solving inviscid steady supersonic flow over non-symmetrical body is presented. This method is based on the mathematical theory of characteristics. In the SCM approach, these coefficients are split according to the sign of the characteristic slopes. The split coefficients are multiplied by appropriate one-sided. Forward differences are associated with negative characteristic slopes, While backward differences are associated with positive slope values.

The numerical example of the blunt sphere-cones have been worked in this paper and compared with ref. 2 to demonstrate good accuracy of SCM in rare mesh.

Investigation on Some Characteristics of the FLIC Method and Its /48  
Application to Calculation of Pitot Pressure of Dusty-gas Shock

Tube Flow

Du Xixin

(China Aerodynamic Research and Development Center)

Abstract

In this paper, a trial method is used to explore some of the features of the FLIC method. The original mass flow calculation method is modified. This modified FLIC method is used to calculate the Pitot pressure of a dusty-gas flow. The result reveals the variation of pitot pressure with loading ratio and time. The stationary part of the Pitot pressure agrees with the analytical solution of the effective flow in the equilibrium region.

I. Introduction

The FLIC method<sup>[1]</sup> have many attractive features. (1) As compared to the point mass lattice method, it does not require many point masses. For a given problem, this will significantly reduce memory storage and computer time. Furthermore, the fluctuation which is characteristic to the point mass lattice method can be avoided. (2) It can be successfully applied to the calculation of two-dimensional flow problems<sup>[1]</sup>. However, just as other difference methods, an artificial viscosity term must be introduced to the FLIC method to improve the stability of the calculation. Just as reference [2] pointed out that the

artificial viscosity term will blur the shock wave and contact surface. For a dusty-gas flow, details of the flow characteristics caused by the presence of dusty particles will be smeared. The flow pattern is distorted. Even, the reality may be destroyed. To this end, an attempt is made in this work to minimize the appearance of discontinuous surfaces in FLIC calculations.

As we know very well that dusty-gas shock tube flow problems have very important practical significance. Until now, this problem has already been widely studied<sup>[3-7]</sup>. Therefore, some basic phenomena in a dusty-gas shock tube flow, such as the effect of particles on the structure of the shock wave and contact surface, the presence of a non-equilibrium region behind the shock wave, and the formation of an effective flow in the equilibrium region to follow, are thoroughly understood. However, studies on the characteristics and variation of the effective flow in the equilibrium region and two-dimensional dusty-gas flow problem are still inadequate. Therefore, there is a need to further investigate these problems.

---

This paper was received on January 11, 1984. Revised manuscript was received on June 14.

## II. The FLIC Method

/49

### 1. Brief Introduction

A detailed introduction of the FLIC method can be formed in reference [1]. Here, we are only going to explain its major characteristics. In order to find the solution, a volume

including the fluid is divided into several lattices, as shown in Figure 1. The center coordinate of a typical lattice is  $i, j$ , which is determined by the position  $(i-1/2)\delta x$  and  $(j-1/2)\delta y$ . A finite difference approximation method for the equation of motion of the fluid is used to bring the quantity in each lattice forward with time. Each computation cycle consists of two steps. First, the median values of velocity and specific internal energy are calculated by considering the accelerating effect of the pressure gradient alone. This means that there is no mass flow across the boundary of the lattice. The second step includes the calculation of the migration effect. It is assumed that the mass flow across the lattice boundary is directly proportional to the density of flow out of the lattice. This is the so-called "flow out of lattice" difference method. The advantage of this method is that the calculation is very stable in the low velocity region. Furthermore, the possibility that a lattice is empty is eliminated. Therefore, the final values of density, velocity and specific internal energy can be obtained from the conservation of mass, momentum and energy. As time progresses, these calculations are repeated for every time increment.

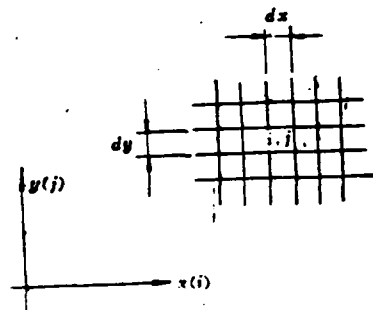


Figure 1. Schematic Diagram of the Calculation Lattice

## 2. Exploration of Some Features

Two different schemes are used to calculate an ideal shock tube flow. Figure 2 shows the result obtained using the original method in reference [1], where the coefficient for the artificial viscosity term  $B = 0$ . In the original method, the equation to calculate the mass flow across the lattice boundary is as follows: if  $\tilde{u}_{i+\frac{1}{2}, j}^n \geq 0$

$$\Delta M_{i+\frac{1}{2}, j}^n = S_{i+\frac{1}{2}, j}^n \rho_{i+\frac{1}{2}, j}^n \tilde{u}_{i+\frac{1}{2}, j}^n \Delta t \quad (1)$$

If  $\tilde{u}_{i+\frac{1}{2}, j}^n < 0$ , then

$$\Delta M_{i+\frac{1}{2}, j}^n = S_{i+\frac{1}{2}, j}^n \rho_{i+\frac{1}{2}, j}^n \tilde{u}_{i+\frac{1}{2}, j}^n \Delta t \quad (2)$$

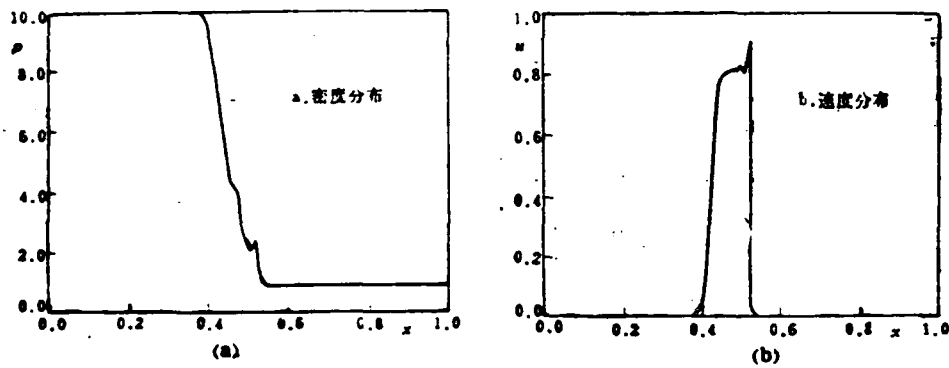


Figure 2. Solution to an Ideal Shock Tube Wave ( $p_4/p_1=10$ ,  $B=0$ )

- a. density distribution
- b. velocity distribution

where  $\Delta M$  is the total mass flow across the right lattice boundary /50 within a time increment  $\delta t$ ,  $S_{i+\frac{1}{2}}^x$  is the area of the right lattice boundary,  $p_{i,j}^n$  or  $p_{i+1,j}^n$  is the so-called density of the flow into our out of the lattice,  $\tilde{u}$  is the x-component of the median velocity, and the superscript  $n$  represents the cycle number of the calculation.  $\tilde{u}_{i+\frac{1}{2},j}^n = (1/2) (\tilde{u}_{i,j}^n + \tilde{u}_{i+1,j}^n)$ . From Figure 2 we can see that when  $B = 0$  there are obvious overshoots and fluctuations for parameters such as velocity and density behind the shock wave. Furthermore, the contact surface is blurred. In the FLIC method, the calculation of the mass flow is extremely important. In order to overcome these difficulties, the original method to calculate the mass flow is modified. Figure 3 shows the result of the modified mass flow calculation

method. The mass flow calculation equation is:

If  $\tilde{u}_{i+\frac{1}{2};j}^n > 0$

$$\Delta M_{i+\frac{1}{2};j}^n = S_{i+\frac{1}{2};j}^n \rho_{i+1,j}^n \tilde{u}_{i+\frac{1}{2};j}^n \delta t \quad (3)$$

If  $\tilde{u}_{i+\frac{1}{2};j}^n < 0$ , then

$$\Delta M_{i+\frac{1}{2};j}^n = S_{i+\frac{1}{2};j}^n \rho_{i,j}^n \tilde{u}_{i+\frac{1}{2};j}^n \delta t \quad (4)$$

From Figure 3 one can see that the shock wave front and the contact surface are very clear. Furthermore, there is no overshoot and oscillation behind the shock wave front. However, with increasing calculation time, it becomes unstable, as shown in Figure 4.

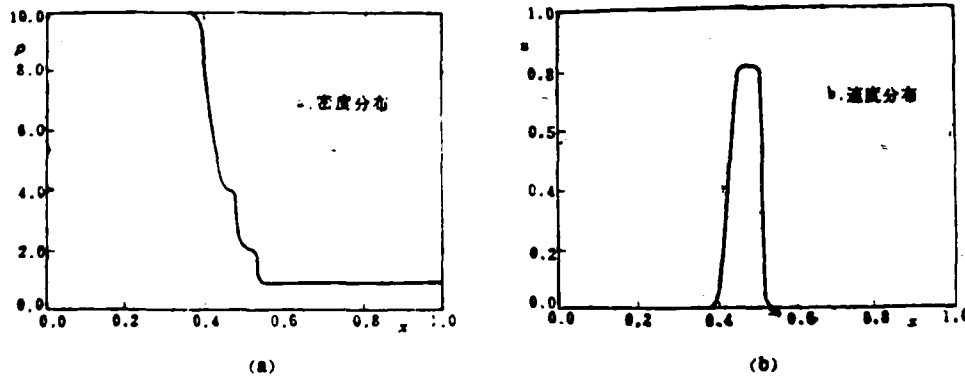


Figure 3. Solution to an Ideal Shock Tube Wave ( $p_4/p_1 = 10$ ,  $B = 0$ ).

- a. density distribution
- b. velocity distribution

### 3. Overcoming the Difficulties

In order to overcome this difficulty, these two methods are used alternatively to stabilize the calculation. In addition, the overshoot and oscillation become very small. The

discontinuous front, however, remains very clear, as shown in Figure 5.

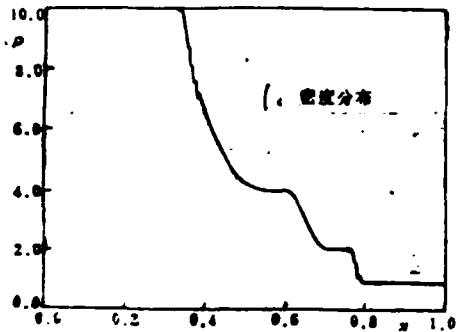


Figure 4. Solution to an Ideal Shock Tube ( $p_4/p_1 = 10$ ,  $B = 0$ )

1. density distribution

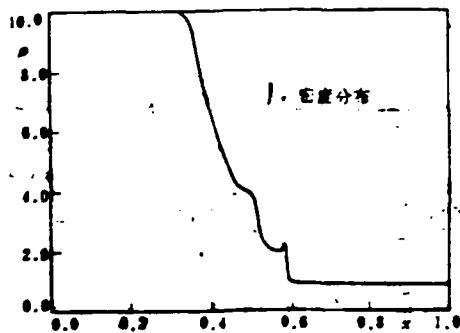


Figure 5. Solution to an Ideal Shock Tube ( $p_4/p_1 = 10$ ,  $B = 0$ )

1. density distribution

### III. Calculation of Pitot Pressure of Unsteady Dusty-gas Shock /51 Tube Flow

Pitot pressure is a very important aerodynamic parameter. Methods to calculate and measure it have very important practical and theoretical significance. For dusty-gas flows, the study on Pitot pressure is not enough. To this end, the aforementioned modified FLIC method is used to calculate the pitot pressure of an unsteady dusty-gas flow.

#### 1. Basic Equations

Let us assume that a dusty-gas mixture flow through a tube. In order to determine the equation of motion for this mixture, it is necessary to make some assumptions. The gas is a total gas. With the exception of interaction with solid particles, its viscosity and thermal conductivity can be neglected. The particles are uniform spheres which are incompressible. There is no variation of mass. Their number must be large enough so that they can be treated continuously. However, there must be so few that that their total volume can be neglected. Other detailed assumptions can be found in reference [6].

Let  $p$ ,  $\rho$ ,  $T$ ,  $u_g$  and  $v_g$  correspond to the pressure, density, temperature and x and y-components of the velocity of the gas, respectively. Let  $\sigma$ ,  $\Theta$ ,  $u_p$  and  $v_p$  correspond to the mass concentration, temperature, and x and y components of the velocity of the particle, respectively. Under the above assumptions, the equations of mass, momentum and energy conservation of the gas and the dust are:

(8)

Continuity equations:

$$\frac{\partial \rho}{\partial t} + \frac{\partial}{\partial x} (\rho u_x) + \frac{\partial}{\partial y} (\rho v_x) = 0 \quad (5)$$

$$\frac{\partial \sigma}{\partial t} + \frac{\partial}{\partial x} (\sigma u_x) + \frac{\partial}{\partial y} (\sigma v_x) = 0 \quad (6)$$

Momentum equations:

$$\rho \frac{Du_x}{Dt} = -\frac{\partial p}{\partial x} - \frac{\sigma}{m} D_x \quad (7)$$

$$\rho \frac{Dv_x}{Dt} = -\frac{\partial p}{\partial y} - \frac{\sigma}{m} D_y \quad (8)$$

$$\sigma \frac{Du_x}{Dt} = \frac{\sigma}{m} D_x \quad (9)$$

$$\sigma \frac{Dv_x}{Dt} = \frac{\sigma}{m} D_y \quad (10)$$

Energy equations:

$$\rho \frac{DI_g}{Dt} = -p \left( \frac{\partial u_x}{\partial x} + \frac{\partial v_x}{\partial y} \right) - \frac{\sigma}{m} [(U_g - U_p) D + Q] \quad (11)$$

$$\sigma \frac{DI_p}{Dt} = \frac{\sigma}{m} Q \quad (12)$$

where  $U_g = (u_g^2 + v_g^2)^{\frac{1}{2}}$ ,  $I_g = C_v T$ ,  $I_p = C_m \Theta$ ,  $m$  is the mass of a single particle, and  $D_x$  and  $D_y$  represent the  $x$  and  $y$  components of the drag  $D$  on the sphere by the flow.  $Q$  represents the heat exchange between the particle and the gas. The equation of state of the gas can be expressed as:

$$p = (\gamma - 1) I_g \rho \quad (13)$$

From these equations, the mutual interacting factors between the particle and the gas are the drag  $D$  and the heat exchange

rate  $Q$ . In order to obtain a set of closed equations, the dependence of  $D$  and  $Q$  on the flow parameters must be given. In this work, the following drag equation is used:

$$D = \frac{\pi}{8} d^2 \rho (U_s - U_p) |U_s - U_p| C_D \quad (14)$$

where

$$C_D = 0.48 + 28 Re^{-1.05} \quad (15)$$

The heat exchange formula is:

$$Q = \pi d \mu C_p Pr^{-1/3} (T - \Theta) Nu \quad (16)$$

where

$$Nu = 2.0 + 0.6 Pr^{1/3} Re^{1/2} \quad (17)$$

where  $C_p$  is the isobaric specific heat of the gas,  $\mu$  is the viscosity coefficient of the gas, and  $Re$  is the Reynolds number calculated based on the diameter  $d$  of the particle and the relative velocity of the particle:

$$Re = \rho_s |U_s - U_p| d / \mu \quad (18)$$

$Pr$  is the Prandtl number

$$Pr = \mu C_p / K \quad (19)$$

where  $K$  is the thermal conductivity of the gas.

Because the surrounding environment of the particle may experience very fast temperature changes, the temperature dependence of the viscosity coefficient  $\mu$  and thermal conductivity  $K$  must be considered. The viscosity coefficient of air can be expressed as:

$$\mu = \mu_0 \left( \frac{T}{T_0} \right)^{0.7} \quad (20)$$

where  $\mu_r$  is the viscosity coefficient at the reference temperature  $T_r$ . Because the temperature dependence of  $K$  is similar to that of  $\mu$  and  $C_p$  is a constant, the Prandtl constant is still a constant  $Pr = 0.75$ . In this calculation, the particle is a small glass ball. The density of the material is  $2.5\text{g/cm}^3$  and the diameter is 10 micron.

## 2. Effect Flow and Its Pitot Pressure in the Equilibrium Region

From references [6] and [7] we know that the particles in the flow reach the limiting velocity and temperature of the gas after a relaxation region behind the shock wave, i.e., the dust-gas mixture reaches an equilibrium. The mixture, in equilibrium, may be considered as a new total gas<sup>[6]</sup> - an effective gas. The effective parameters such as specific heat and soundspeed of this effective gas had been derived and explained in reference [6]. In order to facilitate the following description, we are introducing two important parameters here: (1) frozen Mach number  $M_f$  which is defined as the ratio of the flow to the local gas sonic speed and (2) equilibrium Mach number  $M_e$  which is defined the ratio of the flow to the local effective sonic speed of the mixture.

For this type of effective flow in equilibrium, the Pitot pressure can be expressed as: When  $M_e \leq 1$

$$p_i / \rho u^2 = \frac{1}{\gamma_i M_i^2} \left( 1 + \frac{\gamma_i - 1}{2} M_i^2 \right)^{\gamma_i / (\gamma_i - 1)} \quad (21)$$

$$p'_i/\rho u^2 = \frac{1}{\gamma_i M_i^2} \frac{\left(\frac{\gamma_e+1}{2} M_i^2\right)^{\gamma_e/(\gamma_e-1)}}{\left(\frac{2\gamma_e}{\gamma_e+1} M_i^2 - \frac{\gamma_e-1}{\gamma_e+1}\right)^{1/(\gamma_e-1)}} \quad (22)$$

#### IV. Results and Discussion

The modified FLIC method is used to solve the partial differential equations (5) - (12) for a dusty-gas shock tube flow. Furthermore, the variation of Pitot pressure with time is calculated at various loading ratios.

##### 1. Dust-gas Shock Tube Flow

Figure 6 shows the velocity distribution (using  $\sqrt{p_\infty/\rho_\infty}$  to make it dimensionless) and density distribution (using  $p_\infty$  to make it dimensionless) of a dusty-gas shock tube flow. The distance  $x$  is made dimensionless by using  $l = (4/3) (p_p/p_\infty)d$ .  $p_d$  is the density of the material. The high pressure section of the shock tube is filled with pure air and low pressure section is filled with the dust-gas mixture. The diaphragm pressure ratio  $p_4/p_1 = 10$ . From Figure 6 we can see that the presence of particles makes the shock wave decay. It is followed by a non-equilibrium region where the particles exchange momentum and energy with the gas. When the velocity and temperature of the particle reach the corresponding values of the gas, the flow is in equilibrium. From the density distribution we can see that the decaying contact surface has a fixed area. The calculation grasped the major features of the dusty-gas shock tube flow. In this sense, the modified FLIC method is reliable.

## 2. Pitot Pressure

Figure 7 shows the variation of Pitot pressure with time. The loading ratio  $a = 1.0$ ,  $M_s = 3.6$  and  $d_p = 10$  micron. One can see that a pressure jump is created when the shock wave sweeps across the pressure probe. After an unsteady process, Pitot pressure maintains at a constant level. The flow between the shock wave front and the end of the probe is a non-equilibrium flow. Therefore, the Pitot pressure measured is the non-equilibrium Pitot pressure of the dusty-gas flow under supersonic conditions.

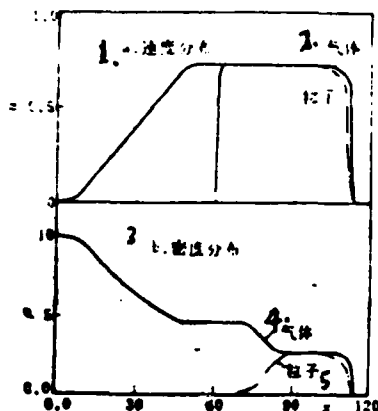


Figure 6. Velocity and Density Distribution of a Dusty-gas Shock Tube

1. velocity distribution
2. gas
3. density distribution
4. gas
5. particle

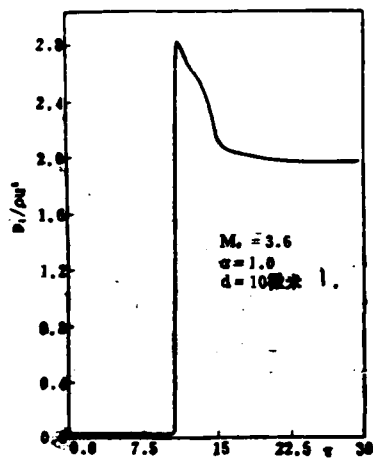


Figure 7. Variation of Pitot Pressure with Time of a Dusty-gas Flow

1.  $d = 10$  micron

Figures 8 and 9 show the variation of Pitot pressure with time at  $M_s = 1.6$  and  $\alpha = 0.4$  and  $1.0$ . We can see an interesting /54 phenomenon, which is that there are many small fluctuations superpositioned onto the unsteady part of the Pitot pressure. As the cause was investigated, it was discovered that when the equilibrium Mach number in the equilibrium region  $M_e < 1$ , this phenomenon exists. When  $M_e > 1$ , these small fluctuations disappear.

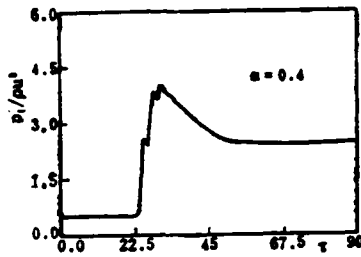


Figure 8. Variation of Pitot Pressure with Time in a Dusty-gas Flow

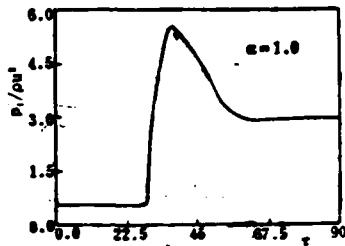


Figure 9. Variation of Pitot Pressure with Time in a Dusty-gas Flow

Figures 10 and 11 represent the variation of the steady value of Pitot pressure with  $\alpha$  at  $M_s = 1.6$  and  $3.6$ , respectively. One can see that (1) the analytical solution (equation (22)) of the effective flow in the equilibrium region is very close to the constant Pitot pressure in non-equilibrium. However, there is a region in Figure 11 where the analytical equation (equation (21)) is very different from the numerical value. This region corresponds to  $\alpha < 0.6$ , i.e.,  $M_e < 1$ . (2) The steady value of Pitot pressure increases with increasing  $\alpha$ .

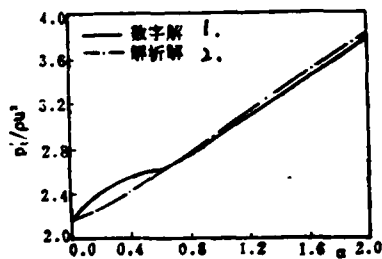


Figure 10. Variation of Pitot Pressure with  $\alpha$ ,  $M_s = 1.6$

1. numerical solution
2. analytical solution

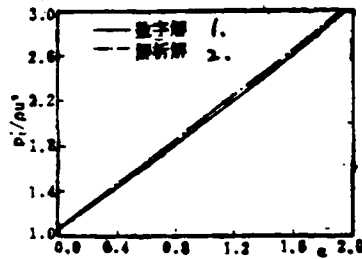


Figure 11. Variation of Pitot Pressure with  $\alpha$ ,  $M_s=3.6$

1. numerical solution
2. analytical solution

#### V. Conclusions

Through the above discussion, we can reach the following conclusions. (1) Details of the effect of the presence of the particles in a dusty-gas shock tube on the flow can be calculated by using the modified FLIC method. This indicates that the modified method is reliable. (2) The pressure of numerous particles in the flow increases the Pitot pressure. The Pitot pressure when  $M_s=1.6$  and  $\alpha=2$  is 1.8 times that of  $\alpha=0$ . When  $M_s=3.6$ , it increases by 3.1 times. From this we can see that the effect of particles on Pitot pressure also increases with increasing Mach number  $M_s$ . (3) When the incoming flow is steady, Pitot pressure reaches a steady value after a relaxation period. When  $M_e > 1$ , the steady Pitot pressure value can be calculated approximately by using the analytical solution (equation (22)) of

the effective flow in equilibrium.

#### References

- [1] Gentry, R.A., Martin, R.E., and Daly, B.J., J. of Computational Physics 1, 87-118 (1966).
- [2] Zhou Yuling and Li Deyuan, Progress in Mathematics, 10, 1 (1981) 46-56.
- [3] Carrier, G.F., J. of Fluid Mechanics, Vol. 4, 1958, /55  
P. 376-382.
- [4] Marble, F.E., Combustion and Propulsion AGARD Colloq. 5th Pergamon Press, 1963, P. 175-213.
- [5] Marcoin, F., Rudman, S., and CAbia, V., AIAA 80-1448 R, of AIAA J. Vol. 19, No. 10, 1980, P. 1294-1301.
- [6] Rudinger, G., The Physics of Fluid, Vol. 7, 1964, P.658-663.
- [7] Miura, H., and Glass, I.I., UTIAS Report No. 250, CN ISSN 0082-5255.
- [8] Marble, F.E., Dynamics of Dusty Gases, Annual Review of Fluid Mechanics, Vol. 2, 1970, pp. 397-446.

The trial calculation is used to explore some of the features of FLIC. The original approach to the mass flow calculation of FLIC is modified through the calculation. The modified FLIC method is used to compute the dusty-gas shock tube flow and its pitot pressure. The results obtained here show clearly both the decay of a frozen shock wave and a contact surface and other details of the flow. The results also show the variation of the pitot pressure with loading ratio and time. The stationary part of the pitot pressure is in good agreement with the analytical value of the effective flow in the equilibrium region of a dusty-gas shock tube flow.

An Experimental Investigation of Flap Turbulent Heat Transfer  
and Pressure Characteristics in Hypersonic Flow

/56

Gao Ruifeng (China Aerodynamic Research and Development Center)

Abstract

This paper introduces the experimental results of the heat transfer and pressure characteristics of a flap installed on a blunt cone model obtained in a shock tunnel. Effects of flap deflection angle, attack angle, Mach number and unit Reynolds number on heat flow and pressure characteristics are discussed. The results indicate that flap deflection angle and Mach number are determining factors affecting the flap heat transfer, pressure characteristics and control effectiveness. The paper also gives the correlation between the peak heat flow and heat pressure,  $\dot{q}_{\max}/\dot{q}_c = (p_{\max}/p_c)^{0.7}$ , as well as an empirical formula to calculate peak heating.

I. Introduction

The three-dimensional flow and its separation characteristics near one flap on a conical body are interesting problems for us. When the flap deflects, it usually results in the interference between shock wave and the boundary layer which frequently leads to the formation of a separation flow. Interference separation can change the apparent pressure distribution and heat distribution on the aircraft as well as on

AD-A162 993

ACTA AERODYNAMICA SINICA (SELECTED ARTICLES)(U) FOREIGN  
TECHNOLOGY DIV WRIGHT-PATTERSON AFB OH F ZHUANG ET AL  
05 DEC 85 FTD-ID(RS)T-0639-85

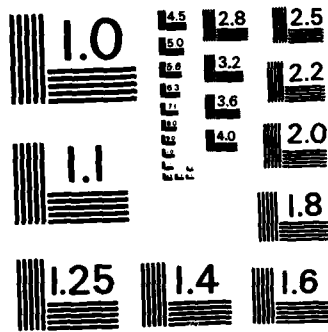
2/2

UNCLASSIFIED

F/G 20/4

NL

END



MICROCOPY RESOLUTION TEST CHART  
NATIONAL BUREAU OF STANDARDS-1963-A

the flap. Consequently, it may affect the stability and control effectiveness of the aircraft, as well as may cause serious local heating of the surface. Therefore, it is necessary to investigate this type of complicated attached and separated flows.

The re-entry model of a hypersonic vehicle is shown in photograph 1. Experimental studies on similar models were reported in references [1] and [2]. Berman et al<sup>[1]</sup> used sharp and little blunt cone models to measure the heat transfer, pressure and drag increase on large deflection angles (45°, 60° and 75°) interference sweeps at  $M_\infty \approx 11$  and  $Re_\infty = 2 \times 10^6$  (based on the length of the model). Kim and Parkinson used Calspan's shock tunnel to measure the heat transfer, pressure and frictional drag of the flap behind a slender cone at  $M_\infty = 7.8 \sim 13.3$  and  $Re_\infty = 3.3 \times 10^6 \sim 70 \times 10^6$ /foot. However, the flap deflection angles were small, 10°-30°. The purpose of this experimental study is to adopt this model (see Photograph 1) to increase the flap deflection angle to measure the heat flow and pressure on the flap and the cone surface in order to determine the effect of factors such as flap deflection angle, Mach number, Reynolds number and attack angle.



Photograph 1

## II. Experimental Conditions

This experiment was conducted in a shock tunnel. The experimental gas is nitrogen. The Mach numbers of the flow are 7.15 and 10.97.

This paper was received on May 16, 1984

The corresponding Reynolds numbers are  $4.34 \times 10^{-7} \text{ m}^{-1}$  and  $4.14 \times 10^7 / 57 \text{ m}^{-1}$ , respectively. Experimental observation of a great deal of boundary layer status data indicates that the flap is totally in turbulence.

The half conical angle of the model is  $10^\circ$ . The bluntness ratio is 0.061. The wing deflection angle  $\delta_f$  is  $22^\circ \sim 51^\circ$ . The angle of attack  $\alpha$  is  $-6^\circ \sim 10^\circ$ . The angle between the flat surface behind the conical model and the axis of cone is  $5.5^\circ$ . The two flap chord lengths are 80 and 36mm, respectively. The spans are 94mm and 37.5mm. The heat flow rate and pressure were measured with a thin film platinum thermister and a piezoelectric pressure transducer, respectively.

## III. Results and Discussion

All experimental results are expressed in terms of the heat flow rate ratio ( $\dot{q}/\dot{q}_c$ ) and pressure ratio ( $p/p_c$ ) where the reference  $\dot{q}_c$  and  $p_c$  are the surface heat flow rate and pressure in front of the shaved flat surface on the rear of the cone where there is no interference.

The flow rate near the flap of the aircraft is three-dimensional. When the flap is deflected and the interference

increases, the strong pressure gradient causes the separation of the attached boundary layer, the shock wave and the interference between boundary layer and the shock wave. Therefore, the flow field is even more complicated (see photographs 2, 3 and 4). The pressure distribution varies violently on and near the flap surface and the heating rate increases significantly. Many characteristics of this spatial flow are related to various influencing factors (such as flap deflection angle, span, chord length, flap profile, tip profile, crevice, Mach number, attack angle and Reynolds number). Effects of various factors on the thermal environment are described and discussed in the following.

Heat Transfer and Pressure Characteristics on Flap Surface. At  $M_\infty = 7.15$  and  $10.97$  and  $Re_\infty = 4.24 \times 10^{-7} m^{-1}$ , the flap heat transfer rate and pressure distribution at various deflection angles are shown in Figure 1. Apparently, the heat transfer and pressure exhibit both a boundary layer and a separation flow pattern, in agreement with the general that the flow is attached or separated when the interference is weak or strong. As compared to the results obtained with a flap on a plate, the peak positions of heat transfer and pressure are lagging behind for the flap on a cone. They vary between 50% chord length to 80% chord length. When the deflection angle is around  $36^\circ$ , the heat flow distribution in the mid chord is slightly distorted. This may be due to the interference of the expansion wave at the shaved flat surface. The following correlation formula is satisfied by the peak heat flow and peak pressure in reference to the rear cone values:

$$\frac{\dot{q}_{max}}{\dot{q}_c} = \left(\frac{p_{max}}{p_c}\right)^{0.7}$$

where  $n = 0.7$ . The correlation power index found by Berman et al is  $n = 0.8$  0.86, and  $n = 0.8$  by Kim<sup>[2]</sup>. The difference may be due to the difference in the local geometrical profile of the model. Therefore, we believe that the correlation index is determined by the local flow field characteristics.

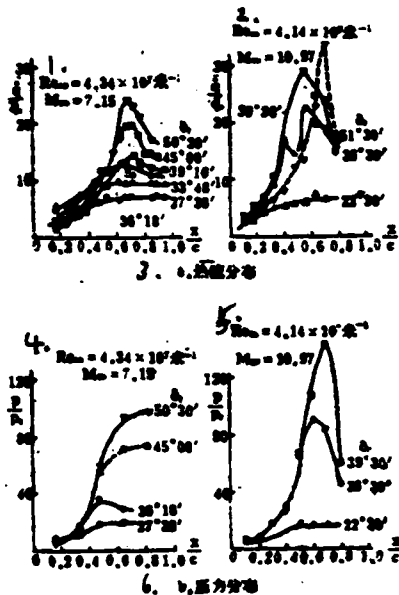


Figure 1. Heat Flow Distribution and Pressure Distribution at the Center of the Flap Wing

1.  $Re_{\infty} = 4.34 \times 10^7 m^{-1}$
2.  $Re_{\infty} = 4.14 \times 10^7 m^{-1}$
3. heat flow distribution
4.  $Re_{\infty} = 4.34 \times 10^7 m^{-1}$
5.  $Re_{\infty} = 4.14 \times 10^7 m^{-1}$
6. pressure distribution

From an engineering angle, on the basis of the analysis given in reference [2] and by using the experimental results in this work, the following empirical formula to calculate the peak

heat transfer is obtained

$$\frac{\dot{q}_{max}}{\dot{q}_s} = 9.136 - 18.39 \delta_f - (23.195 - 56.08 \delta_f) \frac{M_\infty}{Re_\infty^{0.1}}$$

where  $\delta_f$  is in radians and  $Re_\infty$  is the unit Reynolds number ( $m^{-1}$ ). /58  
 The applicable range is:  $28^\circ < \delta_f < 45^\circ$ ,  $\theta_c = 8.5^\circ \sim 11^\circ$ ;  $M_\infty = 7 \sim 11$ ; and small bluntness. The error in most cases is less than +10%. The formula shows that the peak heat flow is proportional to the flap deflection angle and Mach number, and inversely proportional to  $Re_\infty^{0.1}$ .

Characteristics of Heat Flow in Separation Region. The deflection of the flap causes the thermal environment near the flap to vary significantly. Observation of the shadow (see photographs 2, 3 and 4) and measurement of the heat flow indicate that the separation shock wave shifts forward with increasing deflection angle. The region influenced by separation is expanding (see Figure 2).

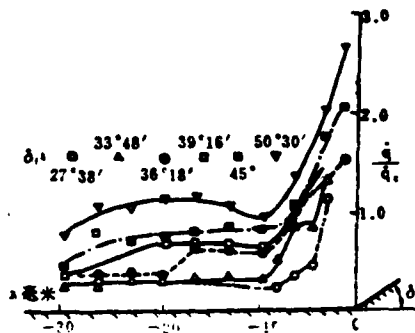
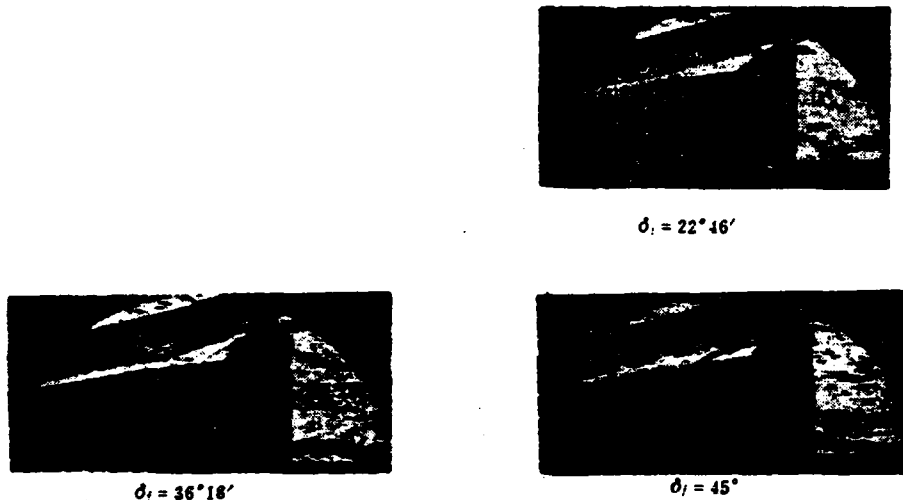


Figure 2. Heat Flow Distribution in Separation Region

( $M_\infty = 7.15$ ,  $Re_\infty = 4.34 \times 10^7$  *M-1*)



(photographs)

Effect of Attack Angle: Under a specific separation condition ( $\delta_f = 39^\circ 16'$ ), the attack angle of the model was changed to  $-4^\circ, 0^\circ, 4$  and  $10^\circ$  to measure the heat flow and pressure on the flap. The results are shown in Figure 3. It was found that the heat flow varies slightly (within a small angle of attack range) ( $-4^\circ \leq \alpha \leq 4^\circ$ ). Hence, the heat transfer ratio at zero attack angle can be roughly used to represent the heat transfer ratio in the range of small attack angles. However, when the attack angle is over  $10^\circ$ , the heat flow on the flap is decreased significantly.

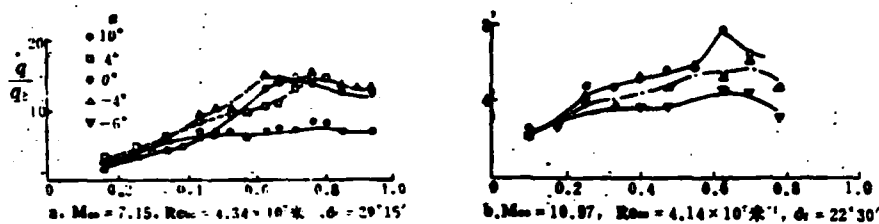


Figure 3. Effect of Attack Angle on Flap Heat Flow Distribution

Under the condition of attached flow ( $\delta_f = 22.5^\circ$ ), the heat transfer ratio and pressure ratio on the flap decrease as the attack angle decreases from  $0^\circ$  to  $-4^\circ$  and  $-6^\circ$ , i.e., the flap is the leeward surface. The flap heat and pressure increase must be slower than the corresponding values on the rear cone surface.

Effect of Reynolds Number. In this work, the Mach number was kept unchanged, i.e.,  $M_\infty = 10.84$ . When the unit Reynolds number  $Re_w = 2.82 \times 10^7 m^{-1}$  and  $4.14 \times 10^7 m^{-1}$ , the measured flap heat transfer ratio and pressure ratio basically do not vary. /59  
Therefore, we believe that the dependence of characteristics controlling the flap heat transfer ratio and pressure ratio on unit Reynolds number is weak in the experimental conditions studied (see Figure 4).

Effect of Mach Number. When the flap deflection angle is  $36.5^\circ$  and the Reynolds number is approximately  $4.24 \times 10^7 m^{-1}$ , at

$M_\infty = 10.97$  and  $7.15$ , experimental results show that the heat transfer ratio and pressure ratio on the flap are strongly dependent on the Mach number. With increasing Mach number, the heat transfer and pressure ratio will increase (see Figure 5).

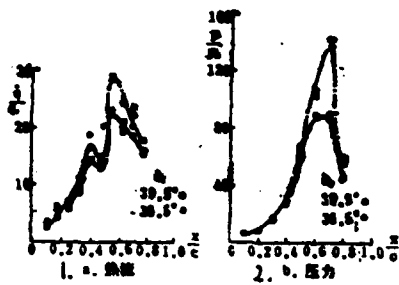


Figure 4. Effect of Unit Reynolds Number on Flap Heat Flow and Pressure

$$\left( M_\infty \approx 10.84, Re_\infty = \begin{cases} 4.14 \times 10^7 m^{-1} (\text{hollow}) \\ 2.82 \times 10^7 m^{-1} (\text{solid}) \end{cases} \right)$$

1. heat flow
2. pressure

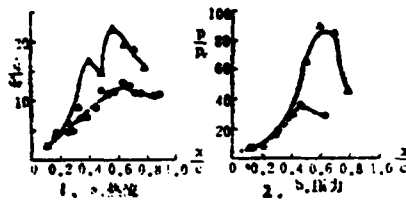


Figure 5. Effect of Mach Number on Flap Heat and Pressure

$$\left( \delta_f = 36.5^\circ, Re_\infty = 4.24 \times 10^7 m^{-1}, M_\infty \begin{cases} 10.97 (\text{triangle}) \\ 7.15 (\text{circle}) \end{cases} \right)$$

1. heat flow
2. pressure

#### IV. Conclusions

Under the experimental flow condition, we reach the following conclusions in studying the turbulent thermal environment on a flap in a blunt cone model:

1. The heat flow and pressure are distributed in a boundary layer or separation flow pattern on the flap. The peak heat transfer and peak pressure (in reference to the value on the rear body) satisfy the following correlation:

$$\frac{\dot{q}_{max}}{\dot{q}_c} = \left( \frac{p_{max}}{p_c} \right)^2$$

2. The variation of flap re-attached flow with attack angle is similar to that of rear cone heat flow with attack angle (in the small attack angle region).

3. The re-attached heat flow and pressure characteristics of the flap are strongly dependent on the Mach number. Their dependence on the unit Reynolds number is weak.

#### References

- [1] Berman, R., Hecht, A., Metzger, J. and Nestler, D., Journal of Spacecraft and Rockets, 14, 3(1977), 163-169.
- [2] Kim, B.S.C. and Parkinson, T.W., AIAA Paper 71-598(1971).

## AN EXPERIMENTAL INVESTIGATION OF FLAP TURBULENT HEAT TRANSFER AND PRESSURE CHARACTERISTICS IN HYPERSONIC FLOW

Gao Ruifeng

(China Aerodynamic Research and Development Center)

#### Abstract

This paper presents experimental results of flap heat transfer and pressure characteristics on a blunt cone in shock tunnel. Effects of flap deflection angle, angle of attack, Mach number and unit Reynolds number are discussed.

Results have shown that flap deflection angle and Mach number are decisive factors, which considerably affect the flap heating, pressure characteristics and control effectiveness. This paper gives a correlation of peak heating and peak pressure.  $\frac{\dot{q}_{max}}{\dot{q}_r} = \left( \frac{p_{max}}{p_r} \right)^{1.7}$ , also gives an empirical formula for estimating peak heating.

LDA Measurements for Leading Edge Vortex Core Velocity of a  
Strake-wing

/61

Lu Zhiyong (Beijing Institute of Aeronautics and Astronautics)  
and Cheng Yuangzhong (Institute No. 304 of Aviation Ministry)

Abstract

The axial velocity distribution of a vortex core on a strake-wing was measured by a two-dimensional laser Doppler anemometer (LDA) in a water funnel. Furthermore, the spatial position of the strake-wing vortex and the variation of the vortex breakdown point with the angle of attack are given.

It is demonstrated in this paper that the axial velocity distribution at various attach angles can be expressed by one curve by choosing an appropriate non-dimensional parameter. But, this is not true at downstream of the vortex breakdown point because of the violent change in velocity.

Introduction

Over a long period of time, the aerodynamic characteristics and the flow phenomena of slender delta wings and strake-wings have been widely studied<sup>[1,2,3]</sup>. It was found that the aerodynamic characteristics of these wings at large angles of attack are determined by the leading edge vortex (see Figure 1). As we all know very well that the leading edge vortex originates from the separation of the shear layer at the leading edge of the

wing. Most of the vortex moment is concentrated in the vortex core. The flow field of a vortex core has been studied extensively. However, most of the studies limited to the measurement of heat and direction<sup>[4,5,6]</sup>. Different from those methods mentioned before, LDA shows its unique advantage that it will not interfere with the flow field<sup>[7]</sup>. In addition, its measuring signal is transmitted at the speed of light. In conjunction with a processing system including a computer, it is capable to perform real time measurement. This is very useful to the study of a vortex core flow field and the measurement of turbulent parameters in the vortex core. The accurate measurement of the flow field can further deepen the study on the leading edge vortex, which will facilitate the creation of more appropriate mathematical models.

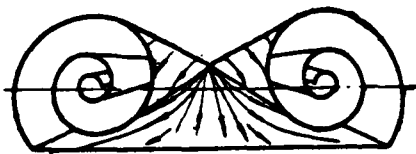


Figure 1. Leading Edge Vortex of a Delta Wing

#### Experimental Apparatus and Model

##### Water Tunnel

The measurement of the flow field of the vortex core of a strake-wing was performed in the water tunnel at Beijing Institute of Aeronautics and Astronautics. The experimental

section of the water tunnel is  $0.4 \times 0.4 \text{m}^2$  in square cross-section. It is 6m long. The Reynolds number based on the average chord length of the model as the reference is  $Re=12000$ .

This paper was received on June 10, 1984

### Hydrogen Bubble Generator

The principle is shown in Figure 2. When the aluminum model is placed between the platinum wire and the carbon rod, the model itself becomes an electrode. Hydrogen bubbles are generated at its leading edge. When the model is at a certain angle of attack, the hydrogen bubbles display the core of the leading edge vortex. When we perform the LDA measurement, hydrogen bubbles are used as the tracing particles. The size of the hydrogen bubble is usually below 4 microns.

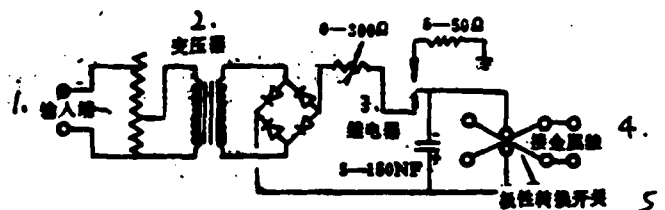


Figure 2. Hydrogen Bubble Generator

1. input end
2. transformer
3. relay
4. to metal wire
5. polarity switch

The DISA two-dimensional Laser Doppler Anemometer (LDA)

The LDA system is shown in Figure 3. In the experiment, the optical system of the LDA is shown in Figure 4.

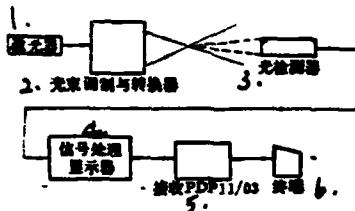


Figure 3. Block Diagram of the LDA System

1. laser
2. beam modulator and converter
3. light detector
4. signal processing display
5. receiving PDP11/03
6. terminal

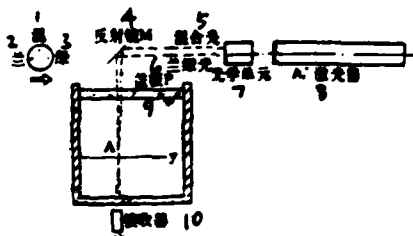


Figure 4. Optical Arrangement of the LDA System

1. mixed
2. blue
3. green
4. mirror M
5. polychromatic light
6. blue and green light
7. optical element
8. laser
9. cover plate P
10. receiver

### Model

The profile and size of the strake-wing is shown in Figure 5. The sweepback angle of the leading edge of the strake is  $X=76^\circ$ . The sweepback angle of the primary wing is  $X=30^\circ$ .

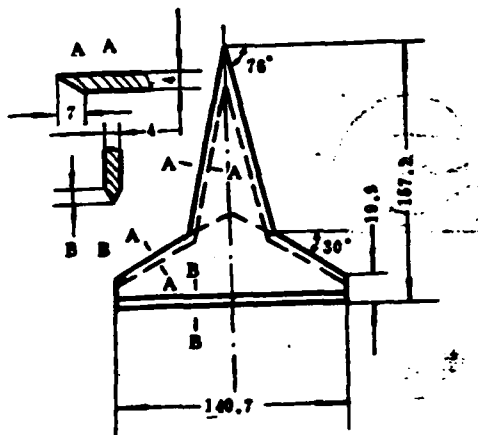


Figure 5. Profile of the Strake-wing

### Results and Discussions

#### 1. Position of Vortex Core and Breakdown of Vortex Core

Figure 6 shows the positions of the vortex core at various angles of attack, which were obtained through the use of hydrogen

bubbles and laser measurements. Figure 7 shows a comparison of the breakdown point of the vortex core for a strake-wing to that of a delta wing. In the current experiment, the breakdown point has already reached the trailing edge when the attack angle  $\alpha=18^\circ$ . This is slightly lower than the result obtained from wind tunnel measurement. It should be pointed out that the position of the breakdown point does not remain unchanged after it is moved onto the primary wing. On the contrary, the breakdown points of the two primary vortices are located on either side. Each of them is moving back and forth around a specific average position. The phase of this movement differs by  $180^\circ$ .

## 2. Axial Velocity Distribution of the Vortex

According to reference [8], the space occupied by the leading edge vortex can be divided into three regions, as shown in Figure 8. The parameters  $D$  and  $\sqrt{\nu t}$  are the major characteristics of these three regions.  $D$  represents the distance between the spiral vortex sheets,  $\sqrt{\nu t}$  is the viscous diffusion distance and  $\nu$  is the dynamic viscosity coefficient.  $t$  is the characteristic time which can be expressed as  $x/U_\infty$ , where  $x$  is the coordinate in the direction of the primary flow and  $U_\infty$  is the incoming flow velocity. The viscous region is  $D \ll \sqrt{\nu t}$ . In this region, the vortex core (also called the subcore) is also spinning as a solid. There is only axial velocity and no rotational velocity on the axis of the vortex. /63

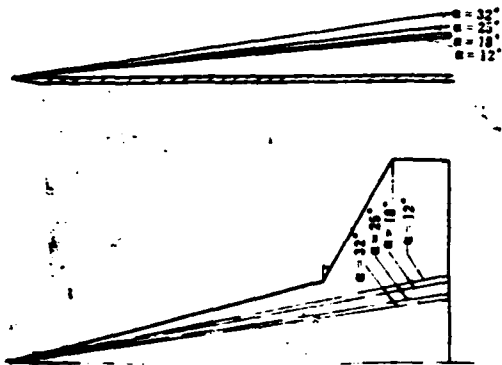


Figure 6. Position of Vortex for a Strake-wing

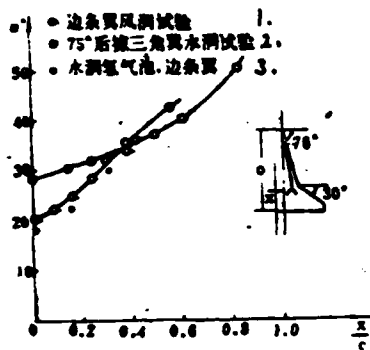


Figure 7. Comparison of Breakdown Position of Strake Vortex

1. Strake-wing Tunnel Experiment
2. 75° Sweepback Delta Wing Water Tunnel Experiment
3. Hydrogen Bubble in Water Tunnel, Strake-wing

Figure 9 shows the axial velocity distribution of the vortex core at 4 different angles of attack. When  $\alpha=12^\circ$ , based on hydrogen bubble observation, the breakdown point is far away from the trailing edge. The axial velocity begins to increase from

the apex. This is because that vortex moment is continuously added to the vortex core along the leading edge from the top. Their trajectory can be considered as a series of spiral lines. An axial velocity component pointed downstream is created with respect to the vortex center. Near the trailing edge, because of the inverse pressure gradient, the axial velocity of the vortex core drops. When  $\alpha=18^\circ$ , the breakdown point of the vortex core has already reached the trailing edge. In this case, the axial velocity of the vortex center drops abruptly behind the breakdown point. The deceleration gradient is very large. It is not the same as the deceleration gradient near the trailing edge at  $\alpha=12^\circ$ . At  $\alpha=25^\circ$ , the breakdown point has already moved forward to the wing surface, approximately at 81% of the root chord. At  $\alpha=35^\circ$ , the vortex breakdown point has moved to 52% of the root chord. Because the vortex intensity increases and the induction effect of the vortex intensifies, the negative pressure on the wing (relative to the static pressure of the incoming flow) increases, and the maximum axial velocity also increases. The axial velocity can be 2.4 times the incoming flow velocity. It should be pointed out that this value is lower than that for a corresponding delta wing. This is because the primary wing of the strake-wing cannot further reinforce the vortex.

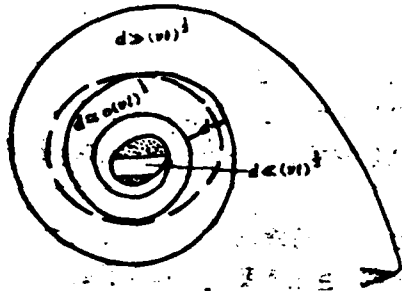


Figure 8. Structure of the Vortex

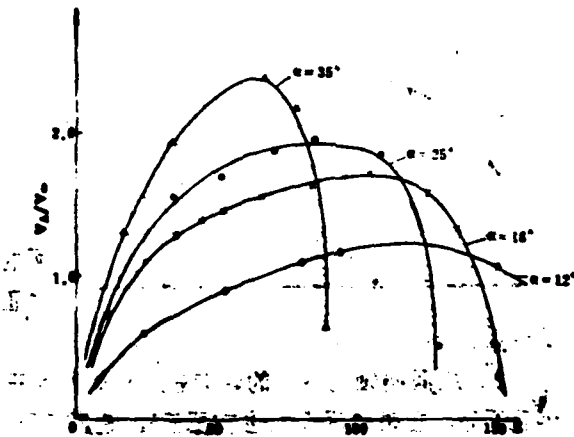


Figure 9. Axial Velocity Distribution Along the Center of the Vortex

### 3. Similarity Curve of Axial Velocity Distribution at the Vortex Center /64

Upstream from the vortex breakdown point, the curves of axial velocity vs. attack angle  $\alpha$  have some similarities. At a

fixed angle of attack, the maximum axial velocity  $U_c$  is used as the reference velocity to render velocity non-dimensional. The distance between the maximum velocity point on the vortex axis and the apex of the wing,  $S_m$ , is used as the family of curves shown in Figure 9 can be expressed as the curve in Figure 10. However, it is not possible to express it downstream from the vortex breakdown point by one curve. Whether this property has a more generalized significance remains to be further verified.

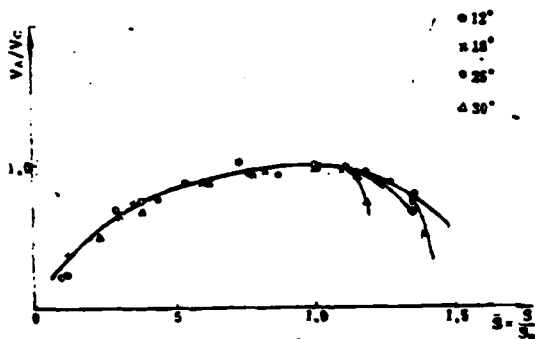


Figure 10. The Similarity Curve

#### 4. Velocity Variation at the Vortex Breakdown Point

The breakdown phenomenon itself is also on unsteady process. As described before, the position of the breakdown point varies with time. The velocity near the breakdown point also varies randomly. Table 1 shows the mean velocity distribution in a very short period of time at the breakdown point. It also shows the corresponding mean square root velocity values. Therefore, we should measure dynamic parameters in order to understand the breakdown phenomenon well and to know the dynamic characteristics

of the flow field after the breakdown.

For delta and strake-wings with a sharp leading edge, the major parameters affecting the breakdown characteristics are the angle of attack  $\alpha$  and the sweepback angle  $\chi$ . The effect of Reynolds number is secondary<sup>[9]</sup>. The direct cause for vortex breakdown is the effect of viscosity and inverse gradient in the vortex core. This is a commonly accepted viewpoint.

Table 1 Velocity and Its Mean Square Root

采样时间序号*	0.1秒内平均 速度 $U_A/U_\infty$	0.1秒内均方根 值 $U_A'/U_\infty$
1	1.79	15%
2	.68	19%
3	.125	63%
4	-.66	63%
5	.28	27.7%

\* 在每一个时间序号下时间为0.1秒采样次数为100次。

1. sampling time sequence\*
2. average velocity within 0.1 sec,  $U_A/U_\infty$
3. root mean square within 0.1 sec,  $U_A'/U_\infty$
4. \* The time in each time sequence number is 0.1 sec. There are 100 samplings

### Conclusions

1. With increasing attack angle, the angle between position of the vortex axis and the wing surface increases and the angle between the plane of symmetry of the wing and the vortex axis decreases. This is an important factor for the presence of the non-linear (upward) torque on a single wing.

2. The axial velocity on any point on the vortex axis begins from the apex and reaches its maximum at a point in front

of the trailing edge. Then, it begins to decrease. At the wing surface where breakdown takes place, the decrease of velocity is caused by an inverse pressure gradient, leading to the breakdown of the vortex.

3. Appropriate non-dimensional parameters are used to express the velocity distribution at any point along the vortex axis of a strake-wing and can be expressed as one curve. Beyond the /65 breakdown point, this general curve does not exist.

In the research process, some comrades from the 506 teaching and research offices and the 304 Institutes assisted in the work.

#### References

- [1] Eearnshaw, P.B. "An Experimental Invesitgation of the Structure of a Leading Edge Vortex" R & M No. 3261, 1961.
- [2] Hummel, D., "On the Vortex Formation over a Slender Wing at Large Angles of Incidence" AGARD-CP-247, October, 1978.
- [3] M-J Liu etc. "Flow Patterns and Aerodynamic Characteristics of Wing-Strake Configuation" Journal of Aircraft, May, 1980.
- [4] Lin Liangshen, Leading Edge Separation Vortex and Its Breakdown of a Delta Wing, Journal of Japan Aeronautic Society, 1972.
- [5] Sforza, P.M., and Smorto, M.J., "Streamwise Development of the Flow over a Delta Wing" AIAA Paper 80-0200.
- [6] Brennenstunl, U., and Hummel, "Vortex formation over Delta Wing" ICAS-82-6.6.3.
- [7] The Two-dimension Laser Doppler Anemometer System and Its Applications, Printed by the 304 Instutute of the Aerospace

Ministry.

- [8] Maskell, E.C., "Some Recent Developments in the Study of Edge Vortices.
- [9] Erickson, G., "Vortex Flow Correlation" ICAS Paper 82-6.6.1.

## LDA MEASUREMENTS FOR LEADING EDGE VORTEX CORE OF A STRAKE-WING

Lü Zhiyong

*(Beijing Institute of Aeronautics and Astronautics)*

Cheng Yuanzhong

*(Institute No. 304 of Aviation Ministry)*

### Abstract

The axial velocity distribution along leading edge vortex core of a strake-wing were measured by means of 2-Dimensional L. D. A and hydrogen bubble technique in the water tunnel, The trajectories of the vortex core and the vortex breakdown point which vary with angles of attack are presented. It has been shown that axial velocity distribution at different angles of attack can be fitted with a nondimensional curve. But this is not true at downstream of vortex breakdown point because of dramatic change of the velocity.

for Low Speed Multi-component Airfoils

Wang Jie (Northwestern Polytechnical University)

I. Introduction

In order to improve the takeoff and landing characteristics of an aircraft, it is necessary to conduct low speed multi-component wind tunnel experiments in the design and selection of various devices to enhance lift.

The height to width ratio of a conventional two-dimensional experimental section is relatively large and the geometric aspect ratio of the model is small. The boundary layer on the wall in the experimental section will affect the experimental result. The narrower the model is, the more serious the effect becomes. The turbulent boundary layer of the tunnel wall expands toward the laminar flow region at the leading edge of the model in a wedge area, which moves the turning point on the middle cross-section of the model forward. When a pressure gradient exists in a two-dimensional airfoil experiment, the flow at the wall becomes extremely complicated. The total intensity is equivalent to the scatter of the vortex circulation of the airfoil on the tunnel wall in all directions. Induced velocity and induced attack angle are created on all cross-sections in the airfoil. Consequently, the two-dimensional nature of the flow is affected.

The most important effect is the premature separation at the model-tunnel wall junction. Far before separation takes place on

the middle cross-section of the model, the boundary layer near the model-tunnel wall junction is separated under a relatively small inverse pressure gradient. Furthermore, it propagates approximately along a  $45^\circ$  angle toward the middle of the model. For models with an aspect ratio less than 2, premature flow separation at the tunnel wall has already affected the pressure measurement at the middle cross-section<sup>[3],[2]</sup>.

## II. Experimental Apparatus, Blowing System, Model and Experimental Technique

The experiment was performed in a direct flow, closed, low speed, two-dimensional wind tunnel. The cross-section in the experimental section is rectangular. It is 2m high and 0.2m wide. The boundary layer thickness on the side wall of the experimental section was measured to be 30mm<sup>[3]</sup>. The experimental wind speed is  $V=45\text{m/sec}$  and the Reynolds number  $Re=1.2 \times 10^6$ .

The blowing system has 6 blowing slots which are installed symmetrically on both sides of the turning wheel (See Figure 1). The front slot is located on the upper surface of the leading edge of the airfoil. It is 150mm long. The middle slot is located at 65% chord length from the leading edge. It is perpendicular to the wing chord and symmetric. The total length is 330mm. The rear slot is located at the upper surface of the flap. It is 80mm long.

Each blowing slot is 2mm wide. Compressed air is blowing out of a pressure stabilizer along the tunnel wall surface. It

was measured that more than 90% of the flow blowing out of the slot along the blowing direction is homogeneous. Furthermore, the flow blowing from the slots to eliminate the wall boundary layer does not have a significant effect on the tunnel flow field itself<sup>[3]</sup>.

This paper was received on December 27, 1983 and revised manuscript was received on April 16, 1984.

The experimental models are single and double slotted flap airfoils. There are 54 pressure measuring holes on the model. The chord length of the basic airfoil is 400mm.

The blowing amount is controlled by a blowing coefficient  $\lambda$ , which is expressed as:

$$\lambda = q_j / q_\infty \quad (1)$$

$$q = \rho_0 \cdot v^2 \quad (2)$$

$$\lambda = (\rho_0 \cdot v_j^2 - p_\infty) / q_\infty \quad (3)$$

where  $q_j$ --dynamic pressure at the outlet of the blowing slot,  $q_\infty$ --dynamic pressure in the experimental section; and  $p_\infty$ --static pressure in the experimental section. There is a pressure measuring hole on the side of the pressure stabilizing box. The pressure sensed through the hole is considered to be the total pressure of the blowing jet  $p_{0j}$ . This pressure is connected to a pressure gauge. The pressure gauge reading is used to accurately control the blowing quantity.

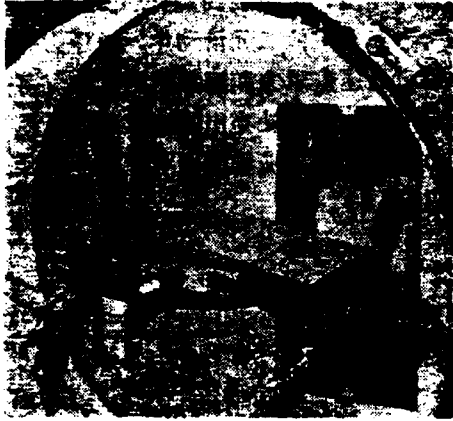


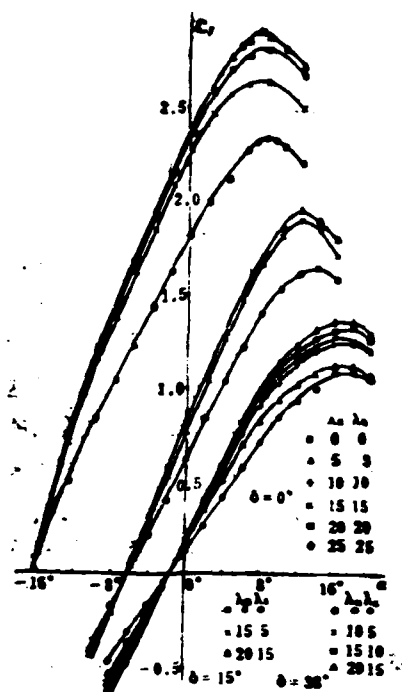
Figure 1. Blowing Slot Installed on the Upper Surface of the Model

According to the measured pressure distribution on the surface of the airfoil, we can calculate the pressure coefficient  $C_p$ . Then, through numerical integration and tunnel wall interference correction, it is possible to obtain the lift, drag and torque coefficient of the whole airfoil. The airfoil drag is obtained by measuring the total pressure loss in the wake.

### III. Experimental Results and Discussion

From the part of experimental curve already obtained (See Figure 2) we can see that the slope of the lift curve  $C_y^a$  and the maximum lift coefficient  $C_{y_{max}}$  are relatively low when not blowing. When the wall boundary layer was blown away by blowing

an amount of air corresponding to  $\lambda_n$  and  $\lambda_s$  equal to 10,  $C_y^a$  and  $C_{y\max}$  are apparently larger. This blowing quantity already made the flow separation appear in the middle cross-section of the model, instead of at the junction of the model and the tunnel wall. Blowing through the front slot is more effective in preventing separation of the tunnel wall boundary layer. When the blowing coefficient exceeds 15,  $C_y^a$  essentially remains unchanged as the blowing quantity increases. In other words, once the blowing exceeds the required quantity to avoid the premature separation at the model-tunnel wall junction, the effect of blowing is no longer obvious. Based on the experimental results obtained with multi-component airfoils with three relative thicknesses at 16.5%-18% in this work, the appropriate blowing coefficient should be controlled between 15-20. Blowing away the tunnel wall boundary layer restores  $C_y^a$  and  $C_{y\max}$ . They are increased by 15%-30% and 0.3-0.4, respectively, as compared to those obtained without blowing.



1. 双槽襟翼型 襟翼偏角  $\phi = 0^\circ, 15^\circ, 20^\circ$

Figure 2. Effect of Blowing on the  $C_y$ - $\alpha$  Curve

$\lambda_n$  - front slot blowing coefficient

$\lambda_s$  - middle slot blowing coefficient

1. double-slotted flap airfoil, flap deflection angle  $\phi = 0^\circ, 15^\circ, 20^\circ$

Because the width of the experimental section is very narrow, when the blowing coefficient is too large, an overblowing effect will appear in the experiment, which will directly affect the pressure measurement at the middle cross-section of the model. This is reflected on the  $C_y^a$  curve. The slope of the lift

curve remains unchanged. The curve is shifted upward and the zero lift attack angle increases. Therefore, the control of the blowing quantity in a small wind tunnel will affect the reliability of the experimental result.

When comparing the pressure distribution with that without /68 blowing, its slope remains unchanged. The surface area beneath the airfoil is essentially unchanged, while the upper surface area is increased (premature separation at the tunnel wall affecting a larger region).

In an actual two-dimensional flow, the pressure differential drag obtained from the pressure distribution should be less than the airfoil drag measured in the wake. The latter is the sum of pressure differential drag and friction drag. However, the airfoil drag when there is no blowing is smaller than the pressure differential drag (See Figure 3). As described before, the vortex from the tunnel wall changes the attach angle at every cross-section. The induced drag is already included in the pressure measured at the cross-section in the middle (See Figure 3).

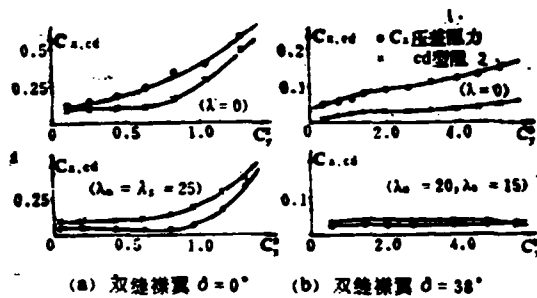


Figure 3. Effect of Blowing on Pressure Differential Drag and Airfoil Drag

- (a) double-slotted flap  $\delta = 0^\circ$
- (b) double-slotted flap,  $\delta = 38^\circ$
- 1. differential drag
- 2.  $C_d$  airfoil drag

#### IV. Conclusion and Prospect

1. Using a tunnel wall boundary layer control technique, it is possible to establish an approximate two-dimensional flow state until stalling. Reliable  $C_y^a$  value can be obtained.

2. The location of the blowing slot is not the key to preventing the large area flow separation beyond the slot. (In this experiment, the position of the front slot was changed, however, we could not see any obvious effect on the experimental result). Nevertheless, blowing slots perpendicular to the local

flow are optimal.

3. Blowing from the slot is most effective on suppressing the effect of the tunnel wall boundary layer. Only the front and middle slots are needed for satisfactory experimental results. In the double-slotted flap, the blowing quantity from the front slot should be higher than that from the middle slot.

The experimental research of using a blowing control technique for the boundary layer is still preliminary. These preliminary conclusions are obtained based on the experimental study of airfoils with large relative thickness. For airfoils with a smaller relative thickness such as modern airfoils including the supercritical airfoils, what combination of blowing quantities can be used to obtain reliable two-dimensional experimental data and whether a reliable  $C_{y\max}$  value can be obtained by blowing and the appropriate correction of the Re number still remain to be studied and explored.

This work received the guidance and assistance from comrades Xia Yushun, Xi Zhongxiang and Bao Guhua. Comrades in the laboratory also actively coordinated the experimental work. The author wishes to express his gratitude to them.

#### References

- [1] Van den Berg, B., AGARD LS No. 43 (1970).
- [2] De Vos, D.M., NLR RR 70050U (1973).
- [3] Xia Yushun, Experimental Report on the Measurement of F-3 Wind Tunnel Boundary Layer Control Flow Field, Technical

Information of Northwestern Polytechnical University, SHJ 8040 (1980).

- [4] Xi Zhongxiang, Research on the Control of Boundary Layer /69 in the F-3 Low Speed Two-dimensional wind tunnel, Northwestern Polytechnical University Technical Information, SHJ 8101, (1981).

## AN EXPERIMENT RESEARCH OF BOUNDARY LAYER CONTROL TECHNIQUE FOR MULTI-COMPONENT AIRFOILS

Wang Jie

(Northwestern Polytechnical University)

### Abstract

The present paper describes some research results of boundary layer control on the wall of a two dimensional low speed wind tunnel with blowing system. In the experimental research the airfoil models with single and double slotted trailing edge flap were adopted. The boundary layer control is a very effective method to prevent the premature flow separation in the junction corner between the tunnel wall and the airfoil model and to get rid of three dimensional effect for single or multi-component airfoil research.

In the paper, some of contrast research results are given by figures and the selection of blowing quantity and the disposition of the blowing slots are described.

Zhang Hanxin, Yu Zechu and Lu Linsheng

(All of China Aerodynamic Research and Development Center)

## 1. Introduction

In the past decade, a great deal of progress was made in solving the N-S equation of a separation flow by numerical methods. Explicit finite difference methods have been developed to a mature stage. However, because of the limitation of stability conditions, it takes longer to calculate a stable solution. In order to overcome this difficulty, implicit methods, such as the implicit factoring method and implicit alternating direction method, were developed. However, these methods require solving three diagonal matrices. As compared to explicit methods, the program for an implicit method is more complex and the computation time needed for every step is longer. In order to avoid the difficulty in the iteration of the three diagonal matrices, MacCormack<sup>[1]</sup> introduced a new implicit method and its iteration process involves the chasing of two diagonal matrices. On the basis of reference [1], an even simpler implicit method is introduced in this paper. Its iteration process only involves scalar chasing. Examples given in this work show that this method is capable of giving results in agreement with those obtained by explicit methods. Its efficiency is comparable to that of reference [1], but it is simple and easy.

## 2. Difference Scheme

### 1. Model Equation

Let us study the following equation:

$$\frac{\partial u}{\partial t} + \frac{\partial F_1}{\partial x} + \frac{\partial F_2}{\partial x} = 0 \quad (2.1)$$

where

$$F_1 = \alpha u \quad (\alpha \neq 0) \quad (2.2)$$

$$F_2 = -v \frac{\partial u}{\partial x} \quad (2.3)$$

$\alpha$  and  $v$  are constants. Let us use the following second order accuracy implicit difference scheme:

$$\begin{aligned} u_i^{\bar{n}+1} &= u_i^n - \frac{\Delta t}{\Delta x} [(1-\beta)(F_{1,i}^n - F_{1,i-1}^n) + \beta(F_{1,i}^{\bar{n}+1} - F_{1,i-1}^{\bar{n}+1})] - \frac{\Delta t}{\Delta x} (F_{2,i}^n - F_{2,i-1}^n) \\ u_{i+1}^{\bar{n}+1} &= u_{i+1}^{\bar{n}+1} - \frac{\Delta t}{\Delta x} [(1+\beta)(F_{1,i+1}^{\bar{n}+1} - F_{1,i}^{\bar{n}+1}) - \beta(F_{1,i+1}^{\bar{n}+1} - F_{1,i}^{\bar{n}+1})] - \\ &\quad - \frac{\Delta t}{\Delta x} (F_{2,i+1}^{\bar{n}+1} - F_{2,i}^{\bar{n}+1}) \\ u_i^{\bar{n}+1} &= \frac{1}{2} (u_i^n + u_{i+1}^{\bar{n}+1}) \end{aligned} \quad (2.4)$$

This paper was received on May 14, 1984. The content of this paper was introduced in the Fluid Mechanics Computation Class at Qinghua University in June 1983.

where  $\beta$  is constant determined by  $\alpha$  and  $v$ . If the first step is /71 to pick a backward difference, then choose  $\beta$  so that  $\beta(\partial F/\partial u) = \beta\alpha > 0$ . If the first step is to pick a forward difference, then choose  $\beta$  so that  $\beta(\partial F/\partial u) = \beta\alpha < 0$ . Let

$$\begin{cases} \delta u_i^{\bar{n}+1} = u_i^{\bar{n}+1} - u_i^n \\ \delta u_{i+1}^{\bar{n}+1} = u_{i+1}^{\bar{n}+1} - u_{i+1}^{\bar{n}+1} \\ F = F_1 + F_2 \end{cases} \quad (2.5)$$

Using Taylor expansion, equation (2.4) can be written as:

$$\begin{cases} \left(1 + d \frac{\Delta t}{\Delta x}\right) \delta u_i^{n+1} = -\frac{\Delta t}{\Delta x} (F_i^n - F_{i-1}^n) + d \cdot \frac{\Delta t}{\Delta x} \delta u_i^{n+1} \\ \left(1 + d \frac{\Delta t}{\Delta x}\right) \delta u_i^{n+1} = -\frac{\Delta t}{\Delta x} (F_{i+1}^n - F_i^n) + d \cdot \frac{\Delta t}{\Delta x} \delta u_i^{n+1} \\ u_i^{n+1} = u_i^n + \frac{1}{2} (\delta u_i^{n+1} + \delta u_i^{n+1}) \end{cases} \quad (2.6)$$

Here,  $d = \beta \alpha > 0$ . If a stability analysis is performed on equation (2.6), it is found that in order to satisfy the stability condition  $d$  should be:

$$d = \max \left\{ \left[ \frac{k}{2} \left( a + \frac{2v}{\Delta x} \right) - \frac{\Delta x}{2 \Delta t} \right], 0 \right\} \quad (2.7)$$

where  $k$  is an insurance index which is larger than 1. One can see that the difference formula (2.6) thus derived is MacCormack's implicit formula. When  $d=0$ , it is MacCormack's explicit formula.

## 2. One-dimensional Unsteady N-S Equation

This equation is 
$$\frac{\partial U}{\partial t} + \frac{\partial F_1}{\partial x} + \frac{\partial F_2}{\partial x} = 0 \quad (2.8)$$

Here,  $U$  is an  $n$  dimensional vector,  $F_1 = F_1(u)$  is a function of a  $n$ -dimensional vector which is not dependent on viscosity, and  $F_2$  is a function of an  $n$ -dimensional vector which is dependent on viscosity. Obviously, equation (2.8) can be written as:

$$\frac{\partial U}{\partial t} + A \frac{\partial U}{\partial x} + \frac{\partial F_2}{\partial x} = 0 \quad (2.9)$$

where  $A = (\partial F_1 / \partial U)$ . Let us assume that it is possible to express  $A$  as  $A = S \Lambda S^{-1}$ . Here,  $\Lambda = \text{diag}(\lambda_{\Lambda}^1)$  and  $\lambda_{\Lambda}^1$  is the eigenvalue of  $A$ .  $S^{-1}$  is the left eigen vector matrix of  $A$  and  $S$  is its inverse matrix. In order to solve equation (2.9), in analogy to the model

$$\begin{cases} U_i^{n+1} = U_i^n - \Delta t \left\{ [SA^- S^{-1}]_i \cdot \left(\frac{\partial U}{\partial x}\right)_{i,0}^n + [SA_+ S^{-1}]_i \cdot \left(\frac{\partial U}{\partial x}\right)_{i,1}^{n+1} \right\} - \Delta t \left(\frac{\partial F_1}{\partial x}\right)_{i,0}^n \\ U_i^{n+1} = U_i^{n+1} - \Delta t \left\{ [SA^+ S^{-1}]_{i+1}^{n+1} \cdot \left(\frac{\partial U}{\partial x}\right)_{i+1}^{n+1} - [SA_+ S^{-1}]_{i+1}^{n+1} \cdot \left(\frac{\partial U}{\partial x}\right)_{i+1}^{n+1} \right\} - \\ \quad - \Delta t \left(\frac{\partial F_1}{\partial x}\right)_{i+1}^{n+1} \\ U_i^{n+1} = \frac{1}{2} (U_i^n + U_i^{n+1}) \end{cases} \quad (2.10)$$

where

172

$$\begin{aligned} A^- &= \text{diag} [(1-\beta)\lambda'_d], \quad A^+ = \text{diag} [(1+\beta)\lambda'_d] \\ A_+ &= \text{diag} (\beta, \lambda'_d), \quad \beta, \lambda'_d > 0 \end{aligned} \quad (A)$$

$\beta$  is a constant to be determined.  $(\partial U/\partial x)_{j,b}$ , and  $(\partial U/\partial x)_{j,f}$  represent the first order backward and forward difference quotient at point  $j$ , respectively. Let  $F = F_1 + F_2$ . By rearranging the above formula it becomes

$$\begin{cases} U_i^{n+1} = U_i^n - \Delta t \left(\frac{\partial F}{\partial x}\right)_{i,0}^n - \Delta t [SA_+ S^{-1}]_i \cdot \left[ \left(\frac{\partial U}{\partial x}\right)_{i,1}^{n+1} - \left(\frac{\partial U}{\partial x}\right)_{i,0}^n \right] \\ U_i^{n+1} = U_i^{n+1} - \Delta t \left(\frac{\partial F}{\partial x}\right)_{i+1}^{n+1} + \Delta t [SA_+ S^{-1}]_{i+1}^{n+1} \left[ \left(\frac{\partial U}{\partial x}\right)_{i+1}^{n+1} - \left(\frac{\partial U}{\partial x}\right)_{i+1}^{n+1} \right] \\ U_i^{n+1} = U_i^n + \frac{1}{2} [(U_i^{n+1} - U_i^{n+1}) + (U_i^{n+1} - U_i^n)] \end{cases} \quad (2.11)$$

because

$$\begin{cases} \left(\frac{\partial U}{\partial x}\right)_{i,0}^{n+1} - \left(\frac{\partial U}{\partial x}\right)_{i,0}^n = \frac{1}{\Delta x} (\delta U_{i+1}^{n+1} - \delta U_{i+1}^n) \\ \left(\frac{\partial U}{\partial x}\right)_{i+1}^{n+1} - \left(\frac{\partial U}{\partial x}\right)_{i+1}^{n+1} = \frac{1}{\Delta x} (\delta U_{i+1}^{n+1} - \delta U_{i+1}^{n+1}) \end{cases} \quad (2.12)$$

Let  $d_1 = \beta_1 \lambda_A^1 > 0$ , then  $\Lambda_\beta = \text{diag} (d_1)$ . Let

$$D = S \Lambda_\beta S^{-1} \quad (2.13)$$

then to a second order accuracy, equation (2.11) can be written as the following:

$$\begin{cases} \left( I + D_i^* \frac{\Delta t}{\Delta x} \right) \delta U_i^{*+1} = -\frac{\Delta t}{\Delta x} (F_i^* - F_{i-1}^*) + D_{i-1}^* \frac{\Delta t}{\Delta x} \delta U_{i-1}^{*+1} \\ \left( I + D_{i+1}^{*+1} \frac{\Delta t}{\Delta x} \right) \delta U_{i+1}^{*+1} = -\frac{\Delta t}{\Delta x} (F_{i+1}^{*+1} - F_i^{*+1}) + D_i^{*+1} \frac{\Delta t}{\Delta x} \delta U_i^{*+1} \\ U_i^{*+1} = U_i^* + \frac{1}{2} (\delta U_i^{*+1} + \delta U_i^{*+1}) \end{cases} \quad (2.14)$$

where  $I$  is a unit matrix.

In the following let us investigate the problem regarding the selection of  $d_1$ . The  $d_1$  which satisfies the stability condition is:

$$d_l \geq \max \left\{ \left[ \frac{1}{2} \left( |\lambda_l^i| + \frac{2\nu}{\Delta x} \right) - \frac{\Delta x}{2\Delta t} \right], 0 \right\} \quad (2.15)$$

$(l=1, 2, \dots, n)$

Therefore, we may choose

$$d_l = \max \left\{ \left[ \frac{k}{2} \left( |\lambda_l^i| + \frac{2\nu}{\Delta x} \right) - \frac{\Delta x}{2\Delta t} \right], 0 \right\} \quad (2.16)$$

This is MacCormack's method. However, just as we pointed out in the introduction, this choice requires operation involving two diagonal matrices. In order to further simplify the computation,  $d_1$ , may be chosen as:

$$d_1 = d_2 = \dots = d_n = \max_l \cdot \max \left\{ \left[ \frac{k}{2} \left( |\lambda_l^i| + \frac{2\nu}{\Delta x} \right) - \frac{\Delta x}{2\Delta t} \right], 0 \right\} = d \quad (2.17)$$

Here,  $d$  is not varying with  $l$ . It satisfies the largest among  $n$  parameters in the stability condition. Substituting equation (2.17) into (2.13) we get

$$D = dI$$

By substituting this equation into (2.14) we get:

$$\begin{cases} \left(1 + d_i^* \frac{\Delta t}{\Delta x}\right) \delta U_i^{n+1} = -\frac{\Delta t}{\Delta x} (F_i^n - F_{i-1}^n) + d_{i-1}^* \frac{\Delta t}{\Delta x} \delta U_{i-1}^n \\ \left(1 + d_{i+1}^* \frac{\Delta t}{\Delta x}\right) \delta U_{i+1}^{n+1} = -\frac{\Delta t}{\Delta x} (F_{i+1}^n - F_i^n) + d_{i+1}^* \frac{\Delta t}{\Delta x} \delta U_{i+1}^n \\ U_i^{n+1} = U_i^n + \frac{1}{2} (\delta U_i^{n+1} + \delta U_i^n) \end{cases} \quad (2.18)$$

This is a simple implicit calculation scheme consisting of an scalar equations. Furthermore, each scalar equation is independent. They can be solved by the scalar chasing method. In addition, it is also possible to change equation (2.14) into a characteristic form. In that case, each equation will have its own one-to-one corresponding  $d_1$  ( $1 = 1, 2, \dots, n$ ). By using these local  $d_1$ 's, we also can obtain an implicit formula with n scalar equations. Obviously, that method is also very simple.

### 3. Example

The sample implicit method described above was used to calculate the laminar separation of a supersonic flow around a two-dimensional compressible corner. The incoming flow conditions are:  $M_\infty = 3.0$ ,  $Re_\infty = 1.68 \times 10^4$ ,  $\alpha = 10^\circ$ . The wall is adiabatic. The initial N-S equation, coordinate transformation and lattice formation are identical to those used in reference [2]. In the calculation rigorous implicit condition was used for the body surface boundary. Figures 1 and 2 show the distribution surface pressure and that of frictional drag, respectively. Furthermore, the results are also compared with those obtained with the explicit method in reference [2] and those with implicit formula in reference [1]. Results show that the time for each step is less than that of MacCormack's method. But,

the overall efficiency is comparable. Similar to the situation in reference [1], after the computation is done to a certain stage, the time step must be continuously reduced to improve accuracy.

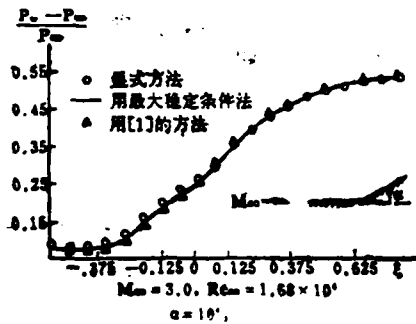


Figure 1. Distribution of Wall Surface Pressure

- o explicit method
- maximum stability condition method
- ▲ method used in reference [1]

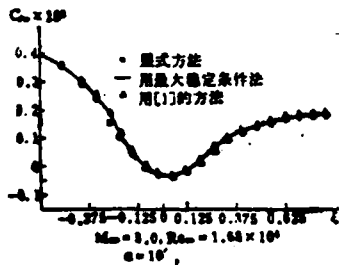


Figure 2. Distribution of Wall Surface Frictional Drag

- o explicit method
- maximum stability condition method
- ▲ method used in reference [1]

Comrade Jie Xinxing also participated in a portion of this work.

#### References

- [1] MacCormack, R.W., A Numerical Method for Solving the Equations of Compressible Viscous Flow, AIAA Paper 81-110.
- [2] Zheng Hanxin et al, Numeical Method for Separation of Supersonic and Hypersonic Viscous Gas Flows, Journal of Mechanics, 4 (1981).

### **A SIMPLER IMPLICIT METHOD SOLVING N-S EQUATION**

Zhang Hanxin, Ya Zechu, Lu Linsheng  
(The China Aerodynamics Research and Development Centre)

#### **Abstract**

A simpler implicit method based on the reference [1] is presented. The process of iteration is only of scalar operation. The calculation shows that the results are in agreement with those given by the explicit method, and that the method is as efficient as MacCormack's, but present method is simpler.

## Indented Blunt Body

Gao Shuchun and Gu Gangmin

(China Aerodynamic Research and Development Center)

During re-entry, a vehicle experiences mostly turbulent flow in the process. Due to high temperature chemical attack and particle cloud erosion, the head is indented. Thus, the calculation of separation flow over an indented body is very significant. Due to flow separation and some complicated flow field interference effects, the structure of the flow field becomes very complex. In recent years, although this type of research has been initiated abroad<sup>[1-3]</sup>, yet there is very little progress. In particular, calculated results of turbulent flows are far apart from experimental data. This is primarily related to factors such as the selection of the turbulence model, the determination of the position of the turning point, and the roughness of the surface. In particular, the mechanism of the turbulence is still not very clear. Consequently, there is some blindness in the determination of models and the establishment of numerical methods. Many people doubt the validity of using the hybrid theory to study the separated turbulent flow. Despite these reasons, people are still using the simplest turbulent flow model to simulate a flow field with separation present<sup>[1,2]</sup>. We believe that this is the simplest treatment before many complicated phenomena are understood. Moreover, it is able to solve

some practical problems.

In this work, the simplified NS equation was used as the starting point to calculate hypersonic flow field over a severely indented axi-symmetric blunt body by using a time dependent implicit spatial factor decomposition method<sup>[1]</sup> and by adopting the Cebeci-Smith double layer vortex viscosity approximation<sup>[2,4]</sup>. The results are more or less in agreement with the calculated and experimental results obtained abroad.

The example used in this work is  $Re_\infty = 6 \times 10^6$ ,  $M_\infty = 9.0$ ,  $T_\infty = 200^\circ R$ ,  $T_w/T_\infty = 3.44$ , and the shape of the object is the same as that in reference [2].

Figure 1 is the pressure distribution in the wall surface, which is close to those described in references [1,2].

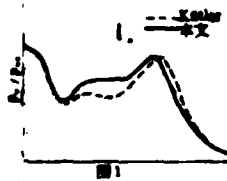


Figure 1

1. this work

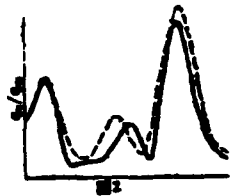


Figure 2

Figure 2 is the heat flow distribution on the wall surface which is close to the result reported in reference [1]. It is also close to the experimental value on a small wall. However, it is quite different from the result reported in reference [2]. There are many reasons for this discrepancy. For instance, in the initial equation the spacing between meshes, the numerical method, and the specific algebraic model can lead to such differences. We believe that these factors are not essential. Why is there such a large discrepancy in the heat flow when the results of wall pressure are basically the same? This is because the heat flow is not a directly calculated quantity. Instead it is a quantity derived from the calculated result. Its magnitude is determined by the temperature gradient and thermal conductivity near the wall surface:

---

This paper was received on June 10, 1984.

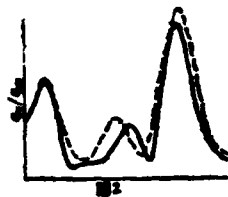


Figure 2

Figure 2 is the heat flow distribution on the wall surface which is close to the result reported in reference [1]. It is also close to the experimental value on a small wall. However, it is quite different from the result reported in reference [2]. There are many reasons for this discrepancy. For instance, in the initial equation the spacing between meshes, the numerical method, and the specific algebraic model can lead to such differences. We believe that these factors are not essential. Why is there such a large discrepancy in the heat flow when the results of wall pressure are basically the same? This is because the heat flow is not a directly calculated quantity. Instead it is a quantity derived from the calculated result. Its magnitude is determined by the temperature gradient and thermal conductivity near the wall surface:

---

This paper was received on June 10, 1984.

Figure 3 compares the frictional drag distribution in a laminar flow to that in a turbulent flow. The frictional drag in the turbulent flow was calculated using a formula similar to equation (3).

Figure 4 compares the shock wave position in a laminar flow to that in a turbulent flow, which agrees with the conclusion in reference [2].

Figures 5-7 show the iso-M, iso-density and isobaric contours of the turbulent flow, respectively. The structure of the flow field is described in detail.

From Figure 5 we can see that the shock wave becomes steeper after the separated flow is re-attached. Hence, there is a second subsonic region.

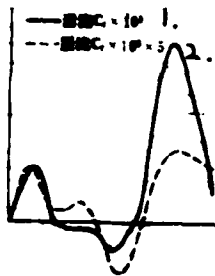


Figure 3

1. turbulent flow
2. laminar flow

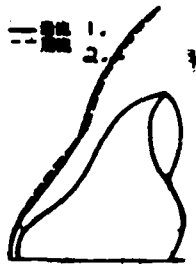


Figure 4 Comparison of Laminar and Turbulent Shock Wave

- 1. turbulent flow
- 2. laminar flow



Figure 5 Iso-Mach Number Lines for Turbulent Flow

Figure 8 shows the flow pattern in the separated region. There is a "Secondary Separation Bubble", which is in agreement with the conclusion in reference [5]. This effect was not found in calculating a turbulent flow.

After approximately 3000 iterations, the flow field of the turbulent flow could basically be created. We were inspired by the work in reference [2] to observe this effect. Our conclusion also agrees with theirs. The authors of that paper believed that it was caused by the interference of the separation bubble and the subsonic band of the blunt body. They also pointed out that a similar effect could be found in calculating a laminar flow. However, we did not observe this oscillating phenomenon in our laminar flow calculation.



Figure 6 Iso-density Contours of Turbulent Flow

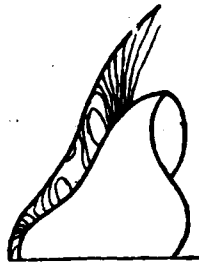


Figure 7 Isobaric Lines of Turbulent Flow

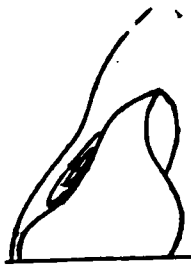


Figure 8 Velocity Trend in Separated Laminar Flow

With a time-dependent technique to solve a separated flow field, because the variation rate of a physical quantity with time oscillates periodically, the flow field does not converge consistently. However, in a certain sense of averaging, the flow field is convergent. Therefore, we should establish specific criteria for an average convergence. Of course, such criteria may vary. The NS equation for a laminar flow is quasi-linear

and the turbulent flow equation, even in the simplest algebraic model, is non-linear. There are difficulties in the solution finding process which are not encountered in the laminar flow calculation. Therefore, we cannot copy a laminar flow model in the calculation of a turbulent flow.

#### References

- [1] Kutler, P., et al, AIAA 78-213.
- [2] Rakich, J.V., et al, AIAA 78-260.
- [3] Kutler, P., et al, AIAA 80-0063.
- [4] Anderson, E.C., and James N. Moss, NASA TN D-7865.
- [5] Hsich, T., AD A 111794, 1982.

## NUMERICAL CALCULATION OF SEPARATION FLOW OVER SEVERELY INDENTED BLUNT BODY

Gao Shuchun, Gu Gangmin  
(China Aerodynamic Research & Development Centre)

#### Abstract

A time dependent space factored implicit numerical procedure solving simplified Navier-Stokes equations is used to calculate axi-symmetric hypersonic viscous flow over a severely indented blunt body. A simple algebraic turbulent model is adopted. The results are compared with another numerical solution in ref 1. A good agreement is found for the wall pressure and heating distribution, although there are some discrepancy in detail for flow structure. A secondary separation bubble is seen clearly in laminar numerical results and high frequency oscillation phenomena are found to be the same as that in the turbulent calculation of ref 2.

Dong Changquan

(Beijing Institute of Information and Control)

### 1. Introduction

In solving the Navier-Stokes equation with an explicit technique, its stability is often limited by the time steps. When it is applied to a high Reynolds number viscous flow, we have to pay a high price even in a two-dimensional case. One of the major problems in any implicit technique is the treatment of the non-linear convection and pressure terms. Earlier computation shows that an alternating direction implicit scheme in conjunction with the quasi-linearization of non-linear terms could be used to calculate the separated base flow field. This type of scheme is obviously able to accelerate the stabilization process, as compared to explicit method, in order to save computer time.

The scheme used in the work is based on the SCM technique developed by Steger and Warming for solving Euler equations and MacCormack's 1980 algorithm. (The advantages of these schemes is to avoid solving three diagonal or three diagonal block equations and to directly create an iteration scheme to simplify the mathematics in each iteration.) A matrix similarity transformation is used to solve the N-S equation by the SCM technique. The viscosity terms are treated by Cay#beB's treatment<sup>[6]</sup> for diffusion terms as well as by a technique similar to that used

by Allen-Cheng-Bpau\*oBcKaЯ. This algorithm can eventually derive an upper or lower triangular matrix. The direct iteration method can save the amount of computation in each iteration as compared to a tridiagonal chasing method.

Finally, it should be pointed out that in order to meet the stability requirement it is very important to add an appropriate dissipation factor in the process. In addition, the boundary condition must be approached in a way consistent with that in the SCM technique. The algorithm has an accuracy to the second order.

## 2. Basic Equations

The following is the non-dimensional Navier-Stokes equation:

$$\frac{\partial \bar{U}}{\partial t} + \frac{\partial \bar{F}}{\partial x} + \frac{\partial \bar{G}}{\partial y} = \frac{\partial \bar{F}_v}{\partial x} + \frac{\partial \bar{G}_v}{\partial y} = \frac{\partial(\bar{V}_1 + \bar{V}_2)}{\partial x} + \frac{\partial(\bar{W}_1 + \bar{W}_2)}{\partial y} \quad (1)$$

The reason to decompose the viscosity terms  $\bar{F}_v$  and  $\bar{G}_v$  into  $\bar{V}_1 + \bar{V}_2$  and  $\bar{W}_1 + \bar{W}_2$  is to facilitate the treatment of mixed derivatives. It also facilitates the use of Cay\*beB's or Allen-Cheng-Bpau\*oBcKaЯ's viscosity treatment. A detailed expression is shown in reference [4]. The region of computation and the boundary condition are defined using the same method as that used in reference [4].

## 3. Computation Technique

Almost at the same time as MacCormack introduced his algorithm in 1980, Steger-Warming<sup>[3]</sup> presented the SCM method

---

This paper was received on June 14, 1984

for solving Euler equations. Furthermore, based on whether the /80 eigen value of the Jacobi matrix A or B is positive or negative, the derivatives are approximated by off-center differences. The coefficient matrix of the derived linear algebraic equation is an upper or a lower triangular matrix to facilitate direct computation. Consequently, the tridiagonal chasing method commonly required in the Beam-Warming factoring method can be avoided to reduce the load of computation in the stabilization process. We employed this technique to solve the Navier-Stokes equation with the objective of making the computation more economical.

According to the second order three layer format introduced by Beam-Warming [3]:

$$\Delta \bar{U}^* = \frac{\theta \Delta t}{1+\xi} \frac{\partial}{\partial t} (\Delta \bar{U}^*) + \frac{\Delta t}{1+\xi} \frac{\partial \bar{U}^*}{\partial t} + \frac{\xi}{1+\xi} \Delta \bar{U}^{*+1} \quad (2)$$

From equation (1) we get

$$\begin{aligned} \Delta \bar{U}^* + \frac{\theta \Delta t}{1+\xi} \left( \frac{\partial}{\partial x} A + \frac{\partial}{\partial y} B \right) \Delta \bar{U}^* &= - \frac{\Delta t}{1+\xi} \left( \frac{\partial \bar{F}}{\partial x} + \frac{\partial \bar{G}}{\partial y} \right)^* + R \bar{H} S \\ R \bar{H} S &= \frac{\theta \Delta t}{1+\xi} \left\{ \frac{\partial}{\partial x} (P - R_x) + \frac{\partial}{\partial x^2} R \right\} \Delta \bar{U}^* + \frac{\theta \Delta t}{1+\xi} \left\{ \frac{\partial}{\partial y} (Q - S_y) + \frac{\partial}{\partial y^2} S \right\} \Delta \bar{U}^* \\ &+ \frac{\theta \Delta t}{1+\xi} \left[ \frac{\partial \Delta \bar{V}_1}{\partial x} + \frac{\partial \Delta \bar{W}_1}{\partial y} \right]^{*+1} + \frac{\Delta t}{1+\xi} \left( \frac{\partial \bar{F}}{\partial x} + \frac{\partial \bar{G}}{\partial y} \right)^* + \frac{\xi}{1+\xi} \Delta \bar{U}^{*+1} \end{aligned}$$

where

$$A = \frac{\partial \bar{F}}{\partial \bar{U}}, \quad B = \frac{\partial \bar{G}}{\partial \bar{U}}, \quad P = \frac{\partial \bar{V}_1}{\partial \bar{U}}, \quad R = \frac{\partial \bar{V}_1}{\partial \bar{U}}, \quad Q = \frac{\partial \bar{W}_1}{\partial \bar{U}}, \quad S = \frac{\partial \bar{W}_1}{\partial \bar{U}}$$

Because  $\bar{F}$  and  $\bar{G}$  are homogeneous functions of  $\bar{U}$ , it is possible to introduce the following similarity transformation:

$$\begin{aligned} A &= Q A_+ Q^{-1} = Q (A_+ + A_-) Q^{-1} = A^+ + A^- \\ B &= Q A_+ Q^{-1} = Q (A_+ + A_-) Q^{-1} = B^+ + B^- \end{aligned}$$

Therefore:

$$\left\{ I + \frac{\theta \Delta t}{1 + \xi} \left( \frac{\partial}{\partial x} A^* + \frac{\partial}{\partial x} A^- + \frac{\partial}{\partial y} B^* + \frac{\partial}{\partial y} B^- \right) \right\} \Delta \bar{U}^*$$

$$= - \frac{\Delta t}{1 + \xi} \left( \frac{\partial \bar{F}^*}{\partial x} + \frac{\partial \bar{F}^-}{\partial x} + \frac{\partial \bar{G}^*}{\partial y} + \frac{\partial \bar{G}^-}{\partial y} \right) + R \hat{H} S$$

$$\bar{F}^* = A^* \bar{U} \quad \bar{F}^- = A^- \bar{U} \quad \bar{G}^* = B^* \bar{U} \quad \bar{G}^- = B^- \bar{U}$$

where

$$\bar{F}(\lambda_1, \lambda_2, \lambda_3) = \frac{\rho}{2\gamma} \begin{vmatrix} 2(\gamma-1)\lambda_1 + \lambda_2 + \lambda_3 \\ 2(\gamma-1)\lambda_1 u + \lambda_2(u+c) + \lambda_3(u-c) \\ 2(\gamma-1)\lambda_1 v + \lambda_2 v + \lambda_3 v \\ (\gamma-1)\lambda_1(u^2+v^2) + \frac{\lambda_2}{2}[(u+c)^2+v^2] + \\ + \frac{\lambda_3}{2}[(u-c)^2+v^2] + W_I \end{vmatrix}$$

$$W_I = \frac{(3-\gamma)(\lambda_2 + \lambda_3)c^2}{2(\gamma-1)}$$

$$\bar{G}(\hat{\lambda}_1, \hat{\lambda}_2, \hat{\lambda}_3) = \frac{\rho}{2\gamma} \begin{vmatrix} 2(\gamma-1)\hat{\lambda}_1 + \hat{\lambda}_2 + \hat{\lambda}_3 \\ 2(\gamma-1)\hat{\lambda}_1 u + \hat{\lambda}_2 u + \hat{\lambda}_3 u \\ 2(\gamma-1)\hat{\lambda}_1 v + \hat{\lambda}_2(v+c) + \hat{\lambda}_3(v-c) \\ (\gamma-1)\hat{\lambda}_1(u^2+v^2) + \frac{\hat{\lambda}_2}{2}[u^2+(v+c)^2] + \\ + \frac{\hat{\lambda}_3}{2}[u^2+(v-c)^2] + W_{II} \end{vmatrix}$$

$$W_{II} = \frac{(3-\gamma)(\hat{\lambda}_2 + \hat{\lambda}_3)c^2}{2(\gamma-1)}$$

$$\bar{F}^{\pm} = \bar{F}(\lambda_1^{\pm}, \lambda_2^{\pm}, \lambda_3^{\pm})$$

$$\bar{G}^{\pm} = \bar{G}(\hat{\lambda}_1^{\pm}, \hat{\lambda}_2^{\pm}, \hat{\lambda}_3^{\pm})$$

The splitting of the eigen value is not unique. There are other ways to divide it into positive and negative parts. In order to overcome the critical state of  $\lambda^+$  and  $\lambda^-$ , appropriate small quantities  $\varepsilon_1$  and  $\varepsilon_2$  are introduced. Hence

$$F^+ = F(\lambda_i^+ + e_1, \lambda_i^+ + e_1, \lambda_i^+ + e_1), \quad F^- = F(\lambda_i^- - e_1, \lambda_i^- - e_1, \lambda_i^- - e_1)$$

$$G^+ = G(\hat{\lambda}_i^+ + e_1, \hat{\lambda}_i^+ + e_1, \hat{\lambda}_i^+ + e_1), \quad G^- = G(\hat{\lambda}_i^- - e_1, \hat{\lambda}_i^- - e_1, \hat{\lambda}_i^- - e_1)$$

In the following, we will discuss the modification of the left hand side terms by RHS. Let us approach second order terms by Cayenne's method [6]:

$$\frac{\partial^2 R^{n+1}}{\partial x^2} = \frac{1}{\Delta x^2} (R_{i+1}^{n+1} - R_i^{n+1}) - \frac{1}{\Delta x^2} (R_{i+1}^{n+1} - R_{i-1}^{n+1})$$

$$\frac{\partial^2 R^{n+1}}{\partial x^2} = \frac{1}{\Delta x^2} (R_{i+1}^{n+1} - R_i^{n+1}) - \frac{1}{\Delta x^2} (R_{i+1}^{n+1} - R_{i-1}^{n+1})$$

The computation format after the modification is:

$$\left\{ \begin{aligned} & \left[ I + \frac{\theta \Delta t}{(1+\xi) \Delta x} \nabla_x (A^+ + A^*) \right] \left[ I + \frac{\theta \Delta t}{(1+\xi) \Delta y} \Delta_y (B^-) \right] \Delta \bar{U}^* \\ & = -\frac{\Delta t}{1+\xi} (\delta_x^f \bar{F}^+ + \delta_y^f \bar{G}^+ + \delta_x^b \bar{F}^- + \delta_y^b \bar{G}^-) + RHS \\ & \left[ I + \frac{\theta \Delta t}{(1+\xi) \Delta y} \nabla_y (B^+ + B^*) \right] \left[ I + \frac{\theta \Delta t}{(1+\xi) \Delta x} \Delta_x (A^*) \right] \Delta \bar{U}^{**} = \Delta \bar{U}^* \\ & \bar{U}^{**} = \bar{U}^* + \Delta \bar{U}^{**} \end{aligned} \right.$$

$\delta_x^b, \delta_x^f, \delta_y^f$  and  $\delta_y^b$  are second order single side difference operators.

$$\left[ I + \frac{\theta \Delta t}{(1+\xi) \Delta x} \Delta_x (A^- + \hat{A}^*) \right] \left[ I + \frac{\theta \Delta t}{(1+\xi) \Delta y} \Delta_y (B^-) \right] \Delta \bar{U}^{**}$$

$$= \frac{\Delta t}{1+\xi} (\delta_x^f \bar{F}^+ + \delta_y^f \bar{G}^+ + \delta_x^b \bar{F}^- + \delta_y^b \bar{G}^-) + RHS^*$$

$$\left[ I + \frac{\theta \Delta t}{(1+\xi) \Delta y} \Delta_y (B^- + \hat{B}^*) \right] \left[ I + \frac{\theta \Delta t}{(1+\xi) \Delta x} \Delta_x (A^*) \right] \Delta \bar{U}^{***} = \Delta \bar{U}^{**}$$

$$\bar{U}^{***} = \frac{1}{2} (\bar{U}^* + \bar{U}^{**} + \Delta \bar{U}^{***})$$

It should be pointed out that a filtering technique consistent with the algorithm is required for regions with intense interruption and high gradient such as shock waves. In order to satisfy the stability requirement, it is very important to include some fourth order dissipation factors in the process such as

$$\frac{\omega_x}{8} \frac{\Delta x'}{(1+\xi)} \frac{\partial' \bar{U}}{\partial x'} + \frac{\omega_y}{8} \frac{\Delta y'}{(1+\xi)} \frac{\partial' \bar{U}}{\partial y'}$$

$\omega_x$  and  $\omega_y$  are the dissipation coefficients. The entire scheme is accurate to the second order. Just as Beam-Warming-Yee<sup>[2]</sup> pointed out, the appropriate approximation of the implicit boundary condition is very important in an implicit scheme. It is able to create an unconditionally stable algorithm consistent with the format of the internal points. (Obviously, the boundary must exist for  $(\Delta t/\Delta x)$  and  $(\Delta t/\Delta y)$  when  $\Delta t$ ,  $\Delta x$  and  $\Delta y \rightarrow 0$ .) Due to page limitation, this cannot be discussed here.

#### 4. Computational Results

In this work, an attempt was made to derive a direct, non-iterative implicit scheme to overcome the deficiency of the traditional upwind format. The resolution of the flow field was improved because the off-center approximation was based on the sign of the eigen value of the coefficient matrices A and B.

We calculated the results in several cases corresponding to  $M_\infty=3,4$  and  $Re_\infty=4000, 1.5 \times 10^4$  on a Univac 1100 computer. Compared to the method used in reference [4], each iteration could save about a half of the computer time. However, it requires more iterations to converge. The entire calculation saves approximately 20% computer time as compared to the process used in reference [4]. The results obtained with both methods are basically consistent. The velocity distribution, density distribution and temperature distribution on the  $x=1.5$  cross-section are shown below, in comparison to the results reported

in reference [4].

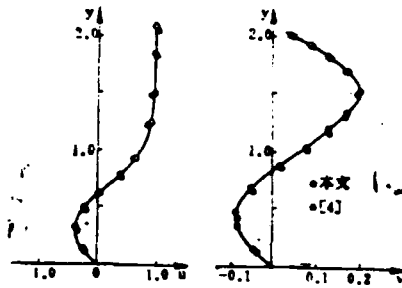


Figure 1 Distribution of Velocities  $u$  and  $v$  on the  $x=1.5$  Cross-section

1. this work

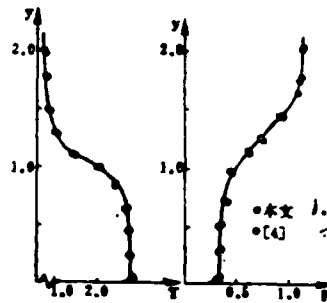


Figure 2 Density Distribution  $p$  and Temperature Distribution  $T$  on the  $x=1.5$  Cross-section

1. this work

## References

- [1] Steger, J.L. & Warming, R.F., J. of Comp. Phys. 40, 2(1980).
- [2] Beam, R.M., Warming, R.F. & Yee, H.C., NASA CP 2201.
- [3] Beam, R.M. & Warming, R.F., AIAA 77-645.
- [4] Dong Changquan, Journal of Aerodynamics, 4(1982).
- [5] MacCormack, R.W., AIAA 81-110.
- [6] Richtmeyer, R.D. & Morton, K.W., (1967) Interscience Publisher, J. Wiley and Sons "Difference Methods for Initial Value Problems" New York.

## AN IMPLICIT TECHNIQUE FOR COMPUTATION OF BASE FLOWFIELD

Dong Changquan  
(Beijing Institute of Information & Control)

### Abstract

A new noniterative implicit scheme for computation of the base flowfields are presented. The new implicit scheme for solution of Navier-Stokes eqs. based on the SCM technique is developed by Steger & Warming (1) for solution of Euler eqs. and some properties of the algorithm analogous to the MacCormack algorithm (5).

Unlike usual implicit schemes, the present algorithm does not require the solution of a block tridiagonal systems, because it leads to block bidiagonal systems. Numerical results indicate rather improvement in accuracy for circulation-region than (4). Furthermore the computer time required to obtain a converged solution has been reduced.

Liu Songling

(Northwestern Polytechnical University)

## I.

It has always been an important problem in fluid dynamics to predict a separated flow. Although the N-S equation can describe a separated flow, however, it requires a great deal of computer time to solve this equation using available techniques. Usually a method to solve the boundary layer equation fails due to the presence of singular points near the separation point. In recent years, inverse methods to solve the boundary layer equation, i.e., to determine the boundary velocity  $u_e$  outside the boundary layer and other parameters with given boundary layer displacement thickness  $\delta^*$  or friction coefficient  $c_f$ , have been developed. Since both displacement thickness and friction coefficient are unknown, it is necessary to first estimate these parameters in using the inverse method. The calculated  $u_e$  value is then compared to that of an inviscous flow to modify  $\delta^*$  or  $c_f$  for recalculation until the velocity distribution obtained agrees with that of inviscous flow.

If a permeation equation is used as an auxiliary equation, then the incompressible flow equation formed by this auxiliary equation and the momentum integral equation is

$$\frac{d\theta}{dx} = \frac{c_f}{2} - (H+2) \frac{\theta}{u_e} \frac{du_e}{dx} \quad (1)$$

$$\theta \frac{dH}{dx} = \frac{dH}{dH_1} \left\{ c_E - H_1 \left[ \frac{c_f}{2} - (H-1) \frac{\theta}{u_e} \frac{du_e}{dx} \right] \right\} \quad (2)$$

$\theta$  is the boundary layer momentum thickness and  $H$  is the shape factor.  $H_1 = (\delta - \delta^*) / \theta$ ,  $\delta$  is the boundary layer thickness, and  $c_E$  is the permeation coefficient. When a forward mode is used,  $(1/u_e)$   $(du_e/dx)$  is known,  $c_f$  and  $c_E$  can be calculated empirically, and  $dH/dH_1$  can be determined from  $H_1 = H_1(H)$  which has already been established. Equations (1) and (2) can be written as:

$$\begin{bmatrix} 1 & 0 \\ H_1 & \theta \frac{dH_1}{dH} \end{bmatrix} \frac{d}{dx} \begin{bmatrix} \theta \\ H \end{bmatrix} = \begin{bmatrix} \frac{c_f}{2} - (H+2) \frac{\theta}{u_e} \frac{du_e}{dx} \\ c_E - H_1 \frac{\theta}{u_e} \frac{du_e}{dx} \end{bmatrix} \quad (3)$$

As  $H$  increases,  $H_1$  decreases and  $dH_1/dH$  approaches zero. There is a singular point in equation (3). If  $\delta^*$  and  $u_c$  are specified as the knowns, then equation (3) becomes:

$$\begin{bmatrix} \frac{\theta}{H} & -\frac{\theta}{u_e} (H+2) \\ \theta \left( \frac{H_1}{H} - \frac{dH_1}{dH} \right) & -\frac{\theta}{u_e} H_1 \end{bmatrix} \frac{d}{dx} \begin{bmatrix} H \\ u_e \end{bmatrix} = \begin{bmatrix} \frac{1}{H} \frac{d\delta^*}{dx} - \frac{c_f}{2} \\ \frac{H_1}{H} \frac{d\delta^*}{dx} - c_E \end{bmatrix} \quad (4)$$

Because  $dH_1/dH \leq 0$ , the determinant of the coefficients on the left side is always not equal to zero to avoid any singular point.

The Lag-Entrainment method developed by Green et al<sup>[1]</sup> is widely used in the computation in aerodynamics. This material

This paper was received on January 28, 1984 and revised manuscript arrived on April 4.

/85

was used in reference [8] to calculate the unseparated turbulent boundary layer on the surface of a compressor blade with satisfactory results. In reference [2], the shape factor relation  $H_1 = H_1(H)$  was modified to be used in an inverse mode calculation in an example of separation caused by a shock wave.

In this work, this method is used to calculate the separated compressible flow in the trailing edge by using the measured displacement thickness to determine the flow velocity  $u_e$ , momentum thickness  $\theta$  and friction coefficient  $c_f$  on the boundary layer.

From the momentum integral equation and permeation equation we can derive that

$$\frac{\theta}{u_e} \frac{du_e}{dx} = \frac{1}{F_1} \left( \frac{d\delta^*}{dx} - F_1 \right) \quad (5)$$

$$F_1 = \frac{Hc_f}{2} + (1 + 0.2rM_e^2) \left( c_f - \frac{H_1c_f}{2} \right) \frac{d\bar{H}}{dH_1}$$

$$F_1 = -H(H+2-M_e^2) + (1 + 0.2rM_e^2) (H+1)H_1 \frac{d\bar{H}}{dH_1}$$

In addition,  $H = \delta^*/\theta$  and  $\bar{H} = (H+1)/(1+0.2rM_e^2) - 1$ , where  $r$  is the restoration coefficient. The relation between  $H_1$  and  $\bar{H}$  is the one recommended in reference [2]. Equation (5) and reference [1] give a closed set of three differential equations. After the initial values are specified,  $u_e$ ,  $\bar{H}$ ,  $\theta$  and  $c_f$  can be solved.

It is demonstrated in practice that, when the initial point is in an area with a larger shape factor, the value of  $c_f$  obtained using the method recommended in reference [1] may be

too large, leading to small  $u_e$  and  $H$  along the process (Example 2). After changing to the method used in reference [3] to determine the initial value of  $c_E$  and using the same differential equation as the one in reference [1] to calculate  $c_E$  along the process, the result is improved significantly.

## II.

The method described above was used in the following examples:

(1) Boundary Layer on the Upper Surface of a Supercritical Airfoil.

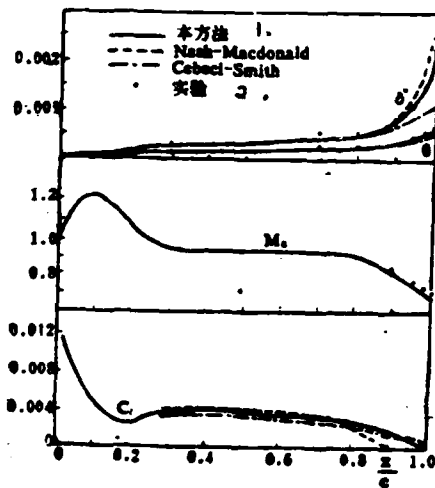


Figure 1

1. this work
2. experimental

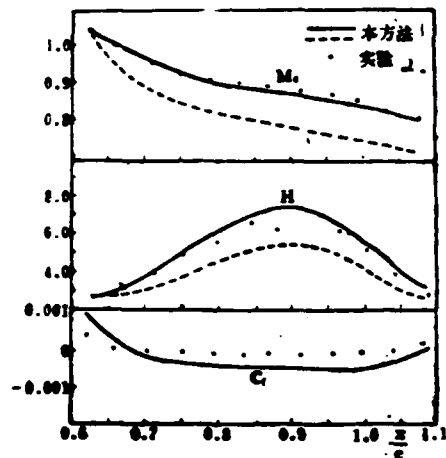


Figure 2

1. this work
2. experimental

Figure 1 shows the measured velocity distribution and boundary layer on an airfoil as reported in reference [4]. The incident flow M number is 0.75 and Re number is  $2 \times 10^6$ . It is separated near the trailing edge. The figure shows calculated results obtained by using forward schemes introduced by Cebeci-Smith and Nash-MacDonald. In the range  $x/c < 0.85$ , a forward mode /86 was used. There is a shock wave at  $x/c = 0.2$  to make the boundary layer thickness grow. But, it is not separated. At  $x/c = 0.85$ , it was switched to an inverse mode. The displacement thickness, momentum thickness and friction coefficient are in agreement with the experimental data. The calculated result at

the trailing edge is much better than those obtained with both forward modes. The calculated M number at the external boundary of the trailing edge boundary layer is less than 4% different from the experimental value.

(2) Boundary Layer on the Upper Surface of a Circular Arc Airfoil in Reference [5]

The thickness of the airfoil is 10%, the chord length is 12 inches, the Re number is  $3.6 \times 10^6$ , and the incident M number is 0.7339. There is a shock wave at 0.62 chord length. The M number in front of the shock wave is 1.32, causing a turbulent boundary layer separation. At approximately 1.05 chord length, the boundary layer is readhered. Figure 2 shows the calculated results, as well as the experimental results given in reference [5]. The calculated M number and shape factor are in good agreement with the experimental data. The calculated friction coefficient is slightly low in the separated region. This method can be used to predict the separation and re-adhesion of the boundary layer. The dotted line in the figure indicates the result obtained using the initial value of  $c_E$  as calculated by the method adopted in reference [1]. After changing to the method used in reference [3] to calculate the initial value of  $c_E$ , the solid line in the figure is obtained.

(3) Boundary Layer on the Upper Surface of a Transonic Compressor Blade

The experimental data obtained on the upper surface boundary layer of the  $V_1$  transonic compressor turbine blade is reported in

reference [6]. The upstream M number is 0.85, chord length is 0.08 M and Re number is  $5 \times 10^6$ . The calculated results are shown in Figure 3. As compared to the experimental data, the maximum deviation of  $M_e$  is less than 5%. The momentum thickness is on the low side. After  $(x/c) > 0.75$ ,  $c_f$  is negative. Thus, we believe that the turbulent boundary layer is already separated in this region.

#### (4) Boundary Layer Reported in Reference [7]

The experimental specimen is a circular arc with a thickness of 18%. The incident M number is 0.7 and the Re number is  $4 \times 10^7$ . Figure 4 shows the results obtained by using the method described in this paper, together with the solution of the N-S equation given in reference [7]. The M number at the trailing edge calculated in this method is 8% lower than the experimental value. The momentum thickness is slightly larger than that calculated based on the N-S equation. Both methods agree with the experimental data to the same extent. The measured separation point is located at  $x = -0.02M$ . The calculated separation point using either method is located downstream from the measured point. Based on this example, we find that the inverse mode technique is not very different from solving the N-S equation.

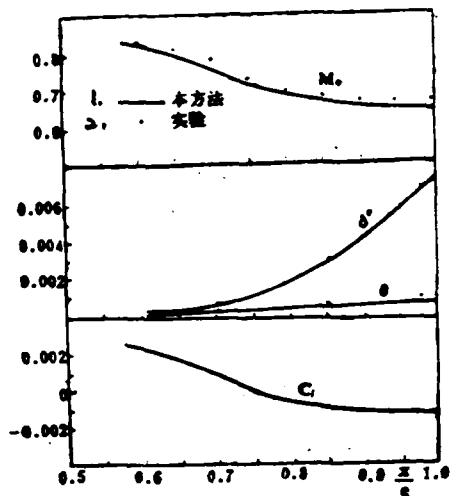


Figure 3

1. this work
2. experimental

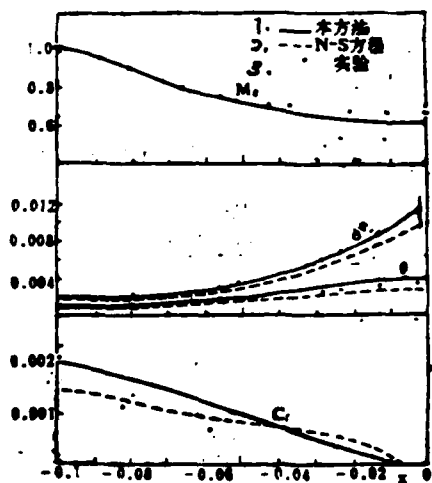


Figure 4

1. this method
2. N-S Equation
3. experimental

From the above computation we arrive at the following conclusions:

(1) It is possible to avoid the singular point near the separation point when using an inverse method to solve the boundary layer equation. It can be used to calculate a separated boundary layer on the trailing edge when the intensity is not too high. The method described can be used to calculate turbulent separated boundary layers with satisfactory results.

(2) Examples show that the result of the inverse method near the separation point is not too different from that obtained by solving the N-S equation.

#### References

- [1] Green, J.E., et al., ARC RM 3791 (1973).
- [2] East, L.F., et al., RAE TR 77046 (1977).
- [3] Head, M.R., ARC RM 3152(1958).
- [4] Spaid, F.W., Jour. Aircraft, 17, 8 (1980), 567-575.
- [5] Alber, I.E., et al., AIAA Jour., 11, 5 (1973), 620-627.
- [6] Calvert, W.J., et al., The Aeronautical Quarterly, 31, 3 (1980), 173-196.
- [7] Viswanath, P.R., et al., AIAA Paper 82-0413.
- [8] Liu Songling et al, Journal of Engineering Thermal Physics, 3, 3 (1982), 226-228.

## **THE COMPUTATIONS OF COMPRESSIBLE TURBULENT SEPARATED BOUNDARY LAYERS**

Liu Songling

*(The North-western Polytechnical University)*

### **Abstract**

The lag-entrainment method is used in an inverse mode to predict two dimensional compressible turbulent separated boundary layers in the trailing edge region. There are reasonable agreements of the predicted values with those several measured from separated turbulent boundary layers. An example shows that the differences between the results obtained by present method and the N-S equation solutions are not significant.

Qin Ning

(Nanjing Aeronautical Institute)

The inverse boundary layer method is a numerical method for solving boundary layer flows. In this method, the displacement thickness  $\delta^*$  or the wall shear stress  $\tau_w$  is the prescribed variable and the velocity distribution  $u_e$  or the pressure distribution of the boundary edge flow is calculated with the boundary layer solution. This can avoid the singularity at the separation point in the finite-difference calculation and provide a meaningful method in solving separated flows. This method requires far less calculations and storage space compared to the direct solution of the N-S equation. In practice, it is a good method of approximation for solving bubble separation in the boundary layer.

We have based on the inverse boundary layer method for separated flows given by Cebeci et al to propose an inverse calculation method for the incompressible boundary flows<sup>[2]</sup>. In this method the displacement thickness  $\delta^*$  is prescribed and the profile of the boundary layer edge velocity is calculated with the boundary layer solution. Falkner-Skan coordinates are used both in direct and inverse calculation regions in order to avoid the matching difficulty between the two regions as that occurred in reference [2] which have used Falkner-Skan coordinates for the direct calculation region and the physical coordinates for the

inverse calculation. Inadequate treatment of the solution at the transition point may cause jump or divergence of the solution. With the transformation coordinates, the variation of the solution at each point is smaller than that with the physical coordinates and the convergency is faster when the values of previous solution are used as the initial values for the next calculation in Newton iteration. Additionally, the use of only one transformation coordinate allows the use of one general calculation process from the starting point  $x=0$  of the direct calculation region to the inverse calculation region containing separations.

#### I. Basic Equations and Transformation

The two-dimensional steady state boundary layer equations for incompressible laminar flows are as follows:

(1a)

$$\frac{\partial u}{\partial x} + \frac{\partial v}{\partial y} = 0$$

(1b)

$$u \frac{\partial u}{\partial x} + v \frac{\partial u}{\partial y} = u_e \frac{du_e}{dx} + \nu \frac{\partial^2 u}{\partial y^2}$$

$$y=0, \quad v=v=0; \quad y=y_s, \quad u=u_e \quad (2)$$

In direct calculation,  $u_e$  is given.

In inverse calculation,  $u_e$  is unknown and  $\delta^*$  is given and the additional boundary condition is obtained from the definition:

$$\delta^* = \int_0^{\infty} \left(1 - \frac{u}{u_e}\right) dy \quad (3)$$

Using Falkner-Skan transformation for the above equations and boundary conditions,

Manuscript received on June 14, 1984

189

$$x = x, \quad \eta = \sqrt{\frac{u_e}{\nu x}} y \quad (4)$$

and it gives

$$f''' + \frac{m+1}{2} f f'' + m[1-f'^2] = x \left( f' \frac{\partial f'}{\partial x} - f'' \frac{\partial f}{\partial x} \right) \quad (5)$$

$$\eta=0, \quad f=f'=0, \quad \eta=\eta_e, \quad f'=1 \quad (6)$$

In direct calculation,  $u_e$  is given.

In inverse calculation,  $u_e$  is unknown, and the boundary conditions are

$$\eta = \eta_e, \quad f = \eta_e - \sqrt{\frac{u_e}{\nu x}} \delta^* \quad (7)$$

where  $f$  is the dimensionless stream function,  $\varphi = (u_e \nu x)^{1/2} f(x, \eta)$ ,  $f' = u/u_e$ ,  $m = x/u_e \, du_e/dx$ , the superscript "\*" is  $\partial/\partial \eta$ .

## II. Numerical Method

### 1. The Finite-Difference Scheme

The Keller box scheme is employed. It has the second order accuracy with unconditional stability. Multiplying equation (5) by  $u_e$ , let  $f=F$  and  $\bar{u}_e=W$ , the differential equation (5) is reduced to the first order differential equations

$$F' = U \quad (8a)$$

$$U' = V \quad (8b)$$

$$WV' + \frac{1}{2} (X \frac{dW}{dX} + W) FV + X \frac{dW}{dX} (1-U^2) = XW \left( \frac{1}{2} \frac{\partial U^2}{\partial X} - V \frac{\partial F}{\partial X} \right) \quad (8c)$$

$$\eta = 0, \quad F=U=0; \quad \eta = \eta_e, \quad U=1 \quad (9)$$

In the inverse method,

$$\eta = \eta_0, \quad F = \eta_0 - \sqrt{\frac{W}{X}} \bar{\delta}^* \quad (10)$$

where

$$\bar{u}_0 = \frac{u_0}{u_\infty}, \quad X = \frac{x}{L}, \quad \bar{\delta}^* = \delta^* \sqrt{Re_{x=L}} / L$$

With  $X=X_0$ , set up an equation at the point  $(X_0, \eta_{j-1/2})$ ;

with  $X=X_j$  ( $i>0$ ), set up an equations at point  $(X_j, \eta_{j-1/2})$  of the two previous equations, and set up an equation at point  $(X_{j-1/2}, \eta_{j-1/2})$  of the third formula. The partial derivatives are approximated

using first order central-difference operators. The following finite-difference equations are obtained.

$$h_{j-1/2}^{-1} (F_j - F_{j-1}) - \frac{1}{2} (U_j - U_{j-1}) = 0 \quad (11a)$$

$$h_{j-1/2}^{-1} (U_j - U_{j-1}) - \frac{1}{2} (V_j - V_{j-1}) = 0 \quad (11b)$$

$$\begin{aligned} (WV^2)_{j-1/2}^{-1} + \frac{1}{2} \left\{ X^{i-1/2} \left( \frac{dW}{dX} \right)_{j-1/2}^{-1} + W^{i-1/2} \right\} (FV)_{j-1/2}^{-1} + \\ + X^{i-1/2} \left( \frac{dW}{dX} \right)_{j-1/2}^{-1} (1-U^2)_{j-1/2}^{-1} - X^{i-1/2} W^{i-1/2} \left[ \frac{1}{2} \frac{\partial U^2}{\partial X} - V \frac{\partial F}{\partial X} \right]_{j-1/2}^{-1} \end{aligned} \quad (11c)$$

$j=2, 3, \dots, J$

and the boundary conditions are

190

$$F_1 = U_1 = 0, \quad U_J = 1, \quad F_J + \frac{(\bar{\delta}^*)^2}{X^{1/2}} (W^2)^{1/2} = \eta_0 \quad (12)$$

The solutions of  $3J+1$  unknowns  $(F_j^i, U_j^i, V_j^i, W^i)$  can be obtained from the group of nonlinear algebraic equations formed from the above equations and the boundary conditions.

## 2. Linearization of the Equations and Obtaining the Solutions

Using Newton's iteration method let

$$F_j^i = F_j^i + \delta F_j^i, \quad U_j^i = U_j^i + \delta U_j^i, \quad V_j^i = V_j^i + \delta V_j^i, \quad W^i = W^i + \delta W^i$$

and substituting them in equations (11) and (12), the following linearized equations are obtained with the omission of  $\delta^2$  and other small quantities.

$$h_{i-1}^{-1} (\delta F_i - \delta F_{i-1}) - \frac{1}{2} (\delta U_i + \delta U_{i-1}) = (r_i)_i, \quad (13a)$$

$$h_{i-1}^{-1} (\delta U_i - \delta U_{i-1}) - \frac{1}{2} (\delta V_i + \delta V_{i-1}) = (r_i)_{i-1} \quad (13b)$$

$$\begin{aligned} (S_i)_i \delta F_{i-1} + (S_i)_i \delta F_i + (S_i)_i \delta U_{i-1} + (S_i)_i \delta U_i + (S_i)_i \delta V_{i-1} \\ + (S_i)_i \delta V_i + (S_i)_i \delta W = (r_i)_i, \\ j=2, 3, \dots, J \end{aligned} \quad (13c)$$

$$\begin{aligned} \delta F_1 = (r_1)_1 = 0, \quad \delta U_1 = (r_1)_1 = 0, \quad \delta U_J = (r_J)_J = 0 \\ \delta F_i + \frac{\bar{\delta}^*}{2(XW)^{1/2}} \delta W = (r_i)_i \end{aligned} \quad (14)$$

The coefficients form a 4x4 diagonal matrix and the solution of the above linear equations can be obtained directly using the general forward method.

The converged solution of a fixed point Newton iteration can be used as the initial value to obtain the solution for the next point.

### 3. Treatment of the Backflow Region

The inverse method can avoid the singularity at the separation point. However, exponential divergency may still occur if the backflow region is not treated. A theoretical analysis has been carried out in reference [6] based on the suitability of the initial conditions of the parabolic equations. We have used the approximation method given at Reyhner and Flugge-Lotz to treat this problem<sup>[3]</sup>. That is

at  $u < 0$ ,  $f'^2 = 0$ ,  $f' \partial f' / \partial x = 0$

#### 4. The Grids of Calculation and the Growth of the Boundary Layer

With transformation coordinates, the thickness of the boundary layer of the attached laminar flow is basically constant. Unevenly distributed grids are employed along the normal direction. The grids are denser near the wall. Uneven grids are also used along the longitudinal direction. The grids employed in the direct method of calculation for the attached boundary layer flow are rather sparse, while those employed in the inverse method of calculation for the region of separation flow are denser. Since the thickness of the boundary layer increases due to separation, the grids along the normal direction in the separation region should be increased.

### III. Example

1. For testing the accuracy of the numerical method, we have calculated the laminar separation flow with  $Re_{\infty, L} = 10^5$ , and two types of  $\delta^*$  distribution<sup>[4]</sup>.

The calculation started from  $X=1.0$  and the Blasius solution was obtained. Inverse calculation was carried out starting from the second point with given distribution of  $\delta^*$ ,  $\Delta X=0.02$ . There were 45 points along the  $X$  direction and 41 points along the  $X$  direction, which increased to 61 points after the separation point.

The results of the numerical calculation are shown in /91 Figures 1 and 2 and compared with the results given by Carter<sup>[4]</sup> using global iteration calculations.

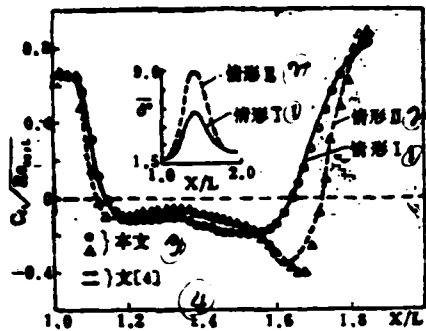


Figure 1.

1. condition I
2. condition II
3. our results
4. reference [4]

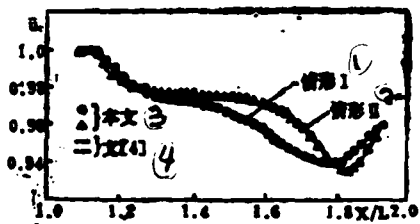


Figure 2.

1. condition I
2. condition II
3. our results
4. reference [4]

2. Calculation Based on Horton's Ntim Experimental Data Given in Reference [5]. Direct method of calculation was carried out for the region from  $x=0$  to  $x=x_{INV}$  using given experimental values  $u_e$ . Inverse calculation was carried out for the region starting from  $x=x_{INV}$  using experimental values of  $\delta^*$ . With  $u_\infty = 9.36\text{M/sec}$ , the calculated results are compared with the experimental values in Figures 3 and 4.

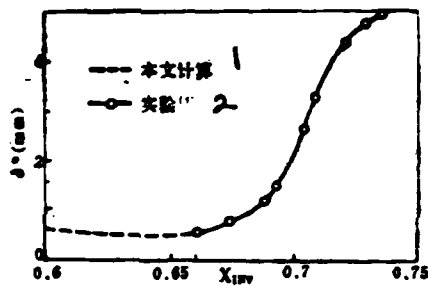


Figure 3.

1. our calculation
2. experimental result [5]

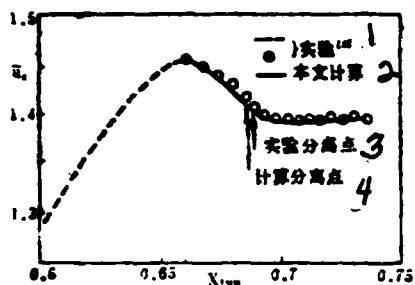


Figure 4.

1. experimental result [5]
2. our calculation
3. separation point in experiment
4. separation point in calculation

The calculation was carried out using FACOM 230 computer. The CPU time is about 50 sec per calculation.

#### IV. Discussion

By comparison of the results of calculation, we have concluded as follows:

1. The calculation results using the forward approximation method of Reyhner and Flugge-Lotz are consistent with the results obtained by global iteration calculations. However, the former method used less calculations and storage space and is an effective method for calculating the separation of bubbles.

2. Using Falkner-Skan coordinates in both direct and inverse calculation regions can provide smooth transition

between the two regions and allows the use of the same numerical procedure for calculation. No jump of the solution will occur at the transition point.

The author wishes to express his appreciation to Prof. Cao Qi-peng for the assistance and consultation in calculation and the preparation of the manuscript.

#### References

/92

- [1] Catherall, D., Mangler, K.W., J. of Fluid Mech. 26,1(1968).
- [2] Bradshaw, P., Cebeci, T., Whitelaw, J.H., Engineering Calculation Methods for Turbulent Boundary Flows (1982).
- [3] Reyhner, T.A., Flugge-Lotz I., Inter. J. of Nonlin. Mech. 3 (1968),
- [4] Carter, J.E., NASA TR-R-447 (1975).
- [5] Horton, H.P., Aero. Quar., 32, 3(1981).
- [6] Qin Ning, Nanjing Aeronautical Institute Research Report No. 1833, (1983).

#### Abstract

This paper presents an numerical method for solving 2-D, steady, incompressible laminar boundary layer flows with separation and reattachment. In the method, the displacement thickness is prescribed and the boundary layer edge velocity is calculated with the boundary layer solution so that the singularity at separation point is avoided. In the reverse flow region, FLARE approximation is used. The finite-difference scheme used here is 2nd order accuracy and unconditionally stable implicit Box method. Falkner-Skan coordinates are used both in direct and inverse calculation regions in order to avoid the matching difficulty between the two regions. The results are compared with global iteration calculations and experimental data.

Li Jingbai    Qi Mengbo

(Nanjing Aeronautical Institute)

### Abstract

The wall lift interference parameters on ground effects for octagonal closed wind tunnels have been derived using image vortex systems. The fillet vortex system can be added to rectangular tunnel vortex system. The vortex lattice method can be used to determine fillet vortex strength. It has been found that the wall lift interference corrections on ground effect have related to not only the wall upwash and streamline curvature effects but also the normal gradient of the upwash velocity at the horizontal tail.

### 1. Introduction

The interference of wall lift in ground effect testing has been investigated in various wind tunnels since over fifty years ago. The image vortex systems of the wing model in the rectangular wind tunnel are two groups of infinite periodic vortex series. The equation for the wall lift interference parameters can be easily derived theoretically. Batchelor has designed an image vortex system for application in octagonal wind tunnels<sup>[1]</sup>.

He has based on the rectangular image vortex system with the addition of continuous distribution of vortices along the rectangular peripheries to determine the vortex strength using

the method with predetermined pattern and to calculate the interference parameter of the wall upwash with the wing positioned at the center and away from the center of the wind tunnel<sup>[2]</sup>.

Fan Jiechuan has applied Batchelor's method to calculate the interference parameter of wall upwash in an octagonal wind tunnel<sup>[3]</sup>. He has also extended this method in calculation of the ground effects and obtained several equations and charts which are suitable for engineering applications. Garner has indicated in reference [4] that the accuracy of the calculation of the upwash interference parameter using Batchelor's method is considerably poor when the wingspan of the wing model is larger than 2/3 of the width of the wind tunnel. Therefore, we have used the vortex lattice method to determine the fillet vortex strength. The wall upwash interference parameters for octagonal closed wind tunnels calculated by this method<sup>[5]</sup> are quite consistent with the accurate solutions obtained by the fixed angle transformation method<sup>[6]</sup>. This method has also other advantages such as it is simple in calculation and better in speed of calculation.

## 2. The Wall Lift Interference Parameter at the Wing

A testing section of octagonal tunnel having width of  $b$ , height of  $h$ , and fillet length of  $t$  is considered. The wing is assumed to be located at the center of the tunnel and a single horseshoe vortex having strength,  $\Gamma$ , and vortex span,  $l$ , is

representing the wing. With coordinate system  $oxyz$  and having the  $x$ -axis along the direction of incoming flow, assume that the attached vortices are on the plan of  $x=0$  and the free vortices are extended infinitely to the downstream and parallel to the  $x$ -axis. In the octagonal test, every fillet is divided into  $q$  elements and a fillet vortex having strength  $K_j$  is placed on every  $1/4$  point  $(z_j, y_j)$ . The  $3/4$  point  $(z_{Ni}, y_{Ni})$  is the control point. With the presence of wall and ground, the image vortex systems, in respect to the wall and the ground of the tunnel, of the horseshoe vortex of the wing and the fillet vortices are shown in Figure 1.

The calculation of the wall lift interference parameter for the octagonal wind tunnel can be carried out based on the calculation for the rectangular tunnel having the same width to height ratio

Manuscript received on December 25, 1982, revised manuscript received on April 15, 1984.

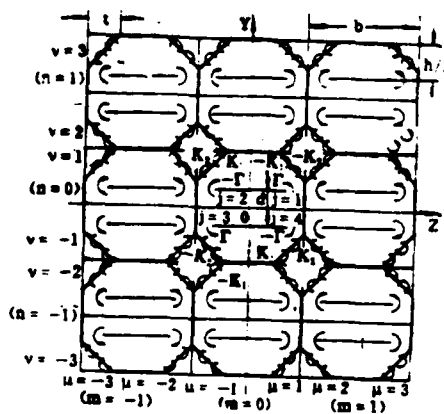


Figure 1. The Image Vortex Systems of the Ground Effect Test

with the additional contribution of the fillet vortices. With the ground effect, the image vortex systems can be regarded as four groups of vertical vortex series having base points at  $(z_j + mb, y_j)$  and interspace of  $(h+2d)$ , where  $(z_j, y_j)$   $j = 1, 2, 3, 4$  are the coordinates of the four free vortices locating immediately next to the origin of the coordinates, and  $m=0, +1, +2, \dots, d$  are the heights of the wing from the ground. Using the induced velocity equation for the vertical vortex series having equal space and same direction of rotation, the equations for calculating the average wall upwash interference parameter,  $\bar{\delta}_R$ , at the wing and the normal derivative,  $\delta_{yOR}$ , of the upwash interference parameter at the center of the wing in the rectangular wind tunnel can be derived (see reference [5] for detail).

For calculating the additional effect of the fillet vortex, the image vortex systems of the wing can be regarded as four equal spaced horizontal vortex series locating at the base points,  $[z_j, y_j+n(h+2d)]$  with interspace  $b$ , where  $n=0, +1, +2, \dots$ . The normal velocity  $C_i$  at any control point on the fillet of the vortex system can be calculated using the induced velocity equation for the horizontal vortex series having equal space and the same direction of rotation. Similarly, the fillet vortex systems can also be regarded as  $4q$  groups of horizontal vortex series based at  $[z_j, y_j+n(h+2d)]$  having interspace  $b$ , equal vortex strength and the same rotation direction.  $(z_j, y_j)$   $j = 1, 2, \dots, q$  are the coordinates of the vortices on the four fillets locating immediately next to the origin of the

coordinates. The induced normal velocity  $F_{i,j}$  at the control point of the vortex series having unit strength can be obtained using the induced velocity equation for the horizontal vortex series. With the condition that the normal velocities on the fillets are zero,

$$\sum_{j=1}^q F_{i,j} K_j = C_i, \quad (i=1,2,\dots,q) \quad (1)$$

The fillet vortex strength  $K_j$  can be obtained by solving the above group of linear algebraic equations. The upwash velocities of the horizontal clockwise vortex series, having base points at  $[z_j, y_j+n(h+2d)]$  and interspace  $b$ , produced near the wing are:

$$\Delta V_{y,i} = -\frac{K_i}{4b} \sum_{j=1}^q \frac{\sin \frac{2\pi}{b} (z-z_i)}{\operatorname{ch} \frac{2\pi}{b} [y-y_i - \pi(h+2d)] - \cos \frac{2\pi}{b} (z-z_j)} dz \quad (2)$$

Using the above equation to obtain the upwash velocity of the wall lift interference can simplify the original two-fold summation formula down to single summation. This will give high speed and accuracy in calculation. Since the above series converges very fast, satisfactory accuracy can be obtained with  $n=\pm 3$ .

The average value of  $\Delta V_{y,j}$  can be obtained by integration of equation (2) along the span direction on the wing surface ( $y=d$ ). The additional average upwash interference parameter produced on the wing by all fillet image vortex systems is:

$$\bar{\delta}_i = \frac{bh}{2\Gamma l} \sum_{j=1}^q \Delta \bar{V}_{y,i} = \frac{bh}{2\Gamma l} \sum_{j=1}^q \frac{1}{l} \int_{-l/2}^{l/2} \Delta V_{y,i} dz \quad (3)$$

Obtaining the derivation of equation (2) with respect to  $y$ , the normal derivative of the additional induced upwash velocity of the fillet systems at the center of the wing ( $y=d, z=0$ ) is

$$\delta_{i.o} = \frac{bh^2}{2\Gamma l} \sum_{i=1}^4 \frac{\partial(\Delta V_{vi})}{\partial y} \quad (4)$$

The parametric area of  $\bar{\delta}_f$  and  $\delta_{yof}$  is  $bh$  and the reference length of the latter is  $h$ . The normal derivatives of the average wall upwash interference parameter of the octagonal wind tunnel and the upwash velocity at the center of the wing are

$$\bar{\delta} = (\bar{\delta}_R + \bar{\delta}_I) \frac{C}{bh} \quad (5)$$

$$\delta_{i.o} = (\delta_{i.o.R} + \delta_{i.o.I}) \frac{C}{bh} \quad (6)$$

respectively, where  $C$  is the cross area of the test section of the octagonal tunnel. The detailed equations of  $\bar{\delta}$  and  $\delta_{yof}$  and the derivation can be obtained in reference [5].

Figure 2 shows the dependence of the wall interference parameter  $\bar{\delta}$  on the span-to-width ratio  $l/b$  and the relative height above ground,  $d/h$ , obtained from the NH-2 low velocity octagonal wind tunnel of the Nanjing Aeronautical Institute (the dimensions of the octagonal test section are  $b=3M, h=2.5M, t=0.4M$ ). It indicates that the wall lift interference parameter  $\bar{\delta}$  decreases rapidly with increasing the height of the model above ground. The value of  $\bar{\delta}$  with ground effect is smaller than that without ground effect. The difference can be as high as one order of magnitude.

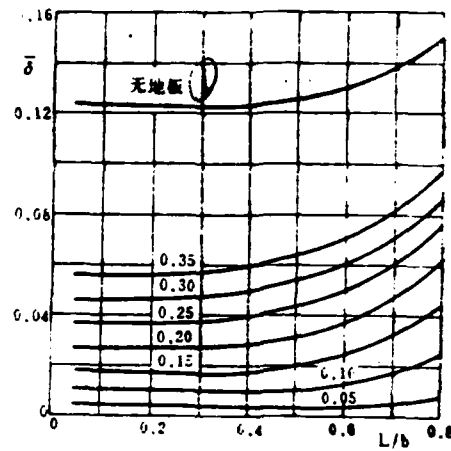


Figure 2. The Average Wall Upwash Interference Parameter of the NH-2 Wind Tunnel

1. without floor

3. The Additional Wall Lift Interference Parameter at the Horizontal Tail

Since the horizontal tail is located downstream of the wing, there is an additional upwash velocity increment at the horizontal tail compared to that at the main wing under the influence of mapping fixed vortex and free vortex systems of the wing. If the projected length of the distance between 1/4 chord point of the mean aerodynamic chord of the horizontal tail and the 1/4 chord point of M.A.C. of the wing on the x-axis is  $L$ , the additional upwash velocity produced by the wing mapping vortex system and the edge mapping vortex systems in the octagonal wind tunnel according to the Biot-Savart formula is

$$\begin{aligned}
V_{z1} = & \frac{\Gamma}{4\pi} \sum_{j=1}^q (-\sigma_{\mu}\sigma_{\nu}) \left[ \frac{1}{x^2 + (\eta_{\nu j} - y)^2} + \frac{1}{(\eta_{\nu j} - y)^2 + (\zeta_{\mu j} - z)^2} \right] \times \\
& \times \frac{x(\zeta_{\mu j} - z)}{\sqrt{x^2 + (\eta_{\nu j} - y)^2 + (\zeta_{\mu j} - z)^2}} - \frac{\Gamma}{4\pi} \sum_{j=1}^q K_j \sum_{\mu, \nu} (\sigma_{\mu}\sigma_{\nu}) \times \\
& \times \left[ \frac{1}{x^2 + (\eta_{\nu j} - y)^2} + \frac{1}{(\eta_{\nu j} - y)^2 + (\zeta_{\mu j} - z)^2} \right] \times \\
& \times \frac{x(\zeta_{\mu j} - z)}{\sqrt{x^2 + (\eta_{\nu j} - y)^2 + (\zeta_{\mu j} - z)^2}}
\end{aligned} \tag{7}$$

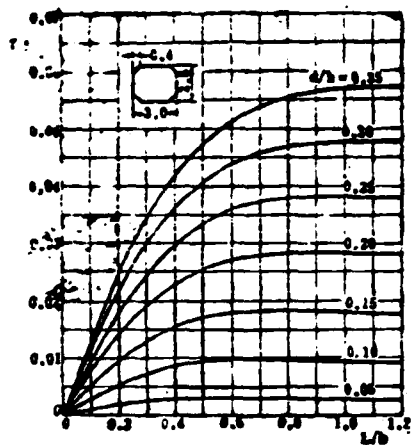
where  $\sigma_{\mu}$ ,  $\sigma_{\nu}$  are +1 or -1 depending on the direction of the vortex  $\sigma_{\mu}\sigma_{\nu}=1$  for counter clockwise vortex and  $\sigma_{\mu}\sigma_{\nu}=-1$  for clockwise vortex in Figure 1,  $(\eta_{\nu j}, \zeta_{\mu j}) = 1, 2 \dots q$  are the coordinates of the wing and the fillet vortices respectively,  $\nu$  and  $\mu$  are integers (Figure 1) and each vortex is represented by a set of  $(\mu, \nu)$ . It should be noticed that the first  $\sum_{\mu, \nu}$  does not include  $(\mu, \nu) = (1, 1), (-1, 1), (1, -1)$  and  $(-1, -1)$ . They are representing the horseshoe vortex and the images with respect to the ground within the wind tunnel. Since Equation (7) converges fast,  $\mu=\nu=9$  is sufficient for calculation. /96

From Equation (7), the additional upwash interference parameter at the horizontal tail can be obtained as [5]

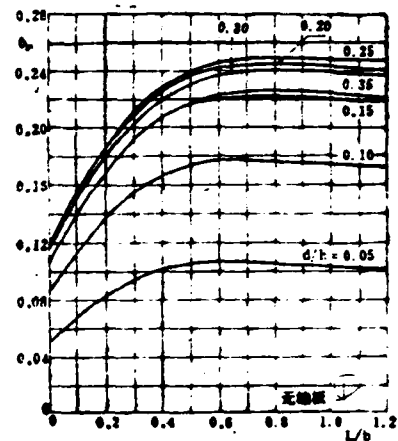
$$\tau \delta_i = \frac{C}{2\Gamma l} V_{z1}(L, d, o), \tag{8}$$

and the normal gradient of the upwash velocity is [5]

$$\delta_{z1} = \delta_{z0} + \frac{Ch}{2\Gamma l} \frac{\partial V_{z1}}{\partial y}(L, d, o) \tag{9}$$



(a) interference parameter



(b) interference parameter

1. no floor

Figure 3. The Wall Interference Parameter at the Horizontal Tail in the NH-2 Wind Tunnel ( $l/b=0.5$ )

Figure 3 shows the dependences of  $\tau\delta_t$  and  $\delta_{yt}$  on the relative height  $d/h$  above ground and the relative distance between the wing and the horizontal tail,  $l/b$ , in the NH-2 wind tunnel with a span-to-width ratio of  $l/b=0.5$ . With the attack angle, there is a horizontal distance between the horizontal tail and the center of the wind tunnel,  $\Delta y_t$ , the induced increment of the attack angle at the horizontal tail is

$$\Delta\alpha_t = \left[ \tau\delta_t + \delta_{yt} \frac{\Delta y_t}{h} \right] \frac{C'_y S}{C} \quad (10)$$

where  $C'_y$  is the uncorrected wall interference parameter,  $S$  is the area of the wing. Since the gradient of the wall upwash velocity is larger at the horizontal tail and the position of the

horizontal tail changes with the attack angle, it should give attention to the fact that the errors of the wall lift interference corrections of the pitching moment and longitudinal static stability in the ground effect testing are larger if the second term in Equation (9) is omitted<sup>[5]</sup>.

#### 4. Conclusions

1. The wall upwash interference parameter with ground effect testing is smaller, to one order of magnitude, than that without ground effect. The image vortex method is a simple and effective method of approximation.

2. The vortex lattice method for calculating the effect of fillet vortices of the octagonal wind tunnel is simpler and more accurate than the Batchelor's predetermined pattern method. /97 /9

3. The effect of the normal gradient of the upwash velocity at the horizontal tail should be considered in correcting the wall lift interference in ground effect testing.

#### References

- [1] Batchelor, G.K., Report ACA-1 (1944).
- [2] Batchelor, G.K., Report ACA-5 (1944).
- [3] Fan Jiechuan, 7210 Report #1, (1978), pp. 55-87.
- [4] Garner, H.C., AGARD ograph 109 (1966).
- [5] Li Jingbai, Qi Mengbo, Nanjing Aeronautical Institute, Technical Report 1243 (1982).
- [6] Gent, B.L., Report ACA-2 (1944).

## WALL LIFT INTERFERENCE CORRECTIONS IN GROUND EFFECT TESTING

Li Jingbai    Qi Mengbo  
(Nanjing Aeronautical Institute)

### Abstract

The wall lift interference parameters on ground effects for octagonal closed wind tunnels has been derived using image vortex systems. The fillet vortex system can be added to rectangular tunnel vortex system. The vortex lattice method can be used to determine fillet vortex strength. It has been found that the wall lift interference corrections on ground effect have related to not only the wall upwash and streamline curvature effects, but also the normal gradient of the upwash velocity at the horizontal tail.

**END**

**FILMED**

---

*20-86*

**DTIC**